WIRELESS SIGNAL ACQUISITION AND PROCESSING TECHNIQUES FOR HORSE LAMENESS DETECTION AND EVALUATION

A Thesis

presented to

the Faculty of the Graduate School

at the University of Missouri-Columbia

In Partial Fulfillment

of the requirements for the Degree

Master of Science in Mechanical Engineering

---

by

BAO ANH NGUYEN

Dr. P. Frank Pai, Thesis Supervisor

DECEMBER 2012

The undersigned, appointed by the dean of the Graduate School, have examined the thesis entitled

"WIRELESS SIGNAL ACQUISITION AND PROCESSING TECHNIQUES FOR HORSE LAMENESS DETECTION AND EVALUATION"

Presented by Bao Anh Nguyen,

a candidate for the degree of Master of Science in Mechanical Engineering

and hereby certify that, in their opinion, it is worthy of acceptance.

_____

Dr. P. Frank Pai

_____

Dr. Kevin G. Keegan

_____

Dr. Yuyi Lin

ACKNOWLEDGEMENT

I am greatly thankful to Dr. P. Frank Pai of the College of Engineering along with Dr. Kevin Keegan and Dr. Marco Lopes of the College of Veterinary Medicine, University of Missouri-Columbia. The three of them had spent a great amount of time advising and helping me finish this thesis.

First, I want to express my deep appreciation to my advisor, Dr. Pai for his acceptance and guidance throughout my graduate study here at Mizzou. He is a dedicated professor who cares about his students' growth and personal lives. For his effort, I have become better not only at doing research, but also at academic writing and presenting. Furthermore, he encourages his students to explore their own ideas in research while still maintaining adequate mentorship. On the other hand, he also creates great personal relationship with his students. He is willing to listen to his students. He gives personal advice. He has his students over his house for Christmas. There are things that define him. I thank him for being such a great advisor.

Second, I want to express my thanks to Dr. Keegan and Dr. Lopes who dedicated a great amount of time and effort for this project. They are great researchers who taught me so much about equine lameness. They are always resourceful, creative and critical. Without their support, this thesis would not have been accomplished. I thank them for their mentorship and tremendous help and support.

Finally, I want to thank Dr. Lin, the third member of my thesis committee. I thank him for all his help. He was a great supervisor. It has been a great experience being a

teaching assistant in his class. I also want to thank the Department of Mechanical and Aerospace Engineering for providing me a teaching assistantship that partially supports my study. The main part of the financial support comes from a National Science Foundation STTR Phase II grant to Equinosis with subcontracting to the University of Missouri, College of Veterinary Medicine.

On the personal life aspect, I would like to thank my wonderful family and friends from all over the world for their help and support. First, I want to express my deep gratitude toward my mother Mrs. Quỳnh Anh, my father Mr. Dũng, and my elder brother Mr. Quang for their unconditional love and support before and during my graduate study. My parents have been staying with me throughout my life to teach, encourage, advise and provide mental support although we live in two time zones different by 12 hours. Also, they have been working extra hard to put me through college and continue to support me financially even after I entered graduate school. They have their good and bad times, but no matter how challenging and critical the issues are, they always stand strong and make sure that I do not have to worry about a thing. They give me a home from half the world away. On the other hand, my brother provides me a home in the United States. He has sacrificed so much for my success and happiness. Often, we do have arguments, sometimes very fierce. But in the end, we always settle everything and stand strong together. It is great to have a brother like him who always look out for his younger brother – me. Without these three people, I am sure I would not be the one standing here today. I also want to thank other relatives as well as friends of my family such as bác Trung and chú Tốp families for their love and support. To my grandfather and my aunt

who passed away a few days ago and two years ago respectively, I am very regret that I did not go home earlier.

Second, I would like to thank the Vietnamese community in Mizzou. From these many great students, I have learned and grown so much. They gave me a sense of belonging, and in turn, I have grown a sense of giving back. Their undwindling hope enhances my hope. Their unconditional love grows my love. They accepted me as a member of the big family, and for them, I become a better person. Therefore, I want to list some of their names here to signify their influence on me. Toward these friends, I have deep gratitude, love and respect. Anh Cường-chị Thi, anh Dũng, Đạt, Giang, Sơn, Nhân, Đạo, Hiếu, Thắng, anh Thông-chị Nguyên, chị Dung, Hiền, Uyên, Linh, anh Thành-chị Dung anh Trí-chị Vy, anh Minh-chị Mai, anh Giang-chị Vân, anh Hạnh-chị Phương, anh Hải-Hiền, anh Hiển-chị Hòa, chị Ngân, Hà, Nga, Trân, Trúc, em Ngọc Anh,Vy, Trang, Khanh, Nhiên, Ngọc Anh, Trí.

Third, I also wish to thank many other professors such as Dr. Fales, Dr. Khanna, Dr. Winholtz, and Dr. Li for their academic as well as personal guidance and help. I want to thank many other friends from Vietnam, Nepal, China, Korea, Iraq, and the United States. All of them have given me great social experience, mental and financial support and advices. My graduate student life would not be complete without them. And hence, I also wish name a few friends who helped me through the most challenging times of my master career: Thảo Nguyên, Hải and Hao.

TABLE OF CONTENTS

ACKNOLEDGEMENTS ii

LIST OF FIGURES vii

LIST OF TABLES xi

ABSTRACT xii

CHAPTER 1: INTRODUCTION 1

1.1. Introduction 1
1.2. Equine Lameness Locator 1
1.3. Motivation and Thesis Organization 8

CHAPTER 2: SIGNAL DECOMPOSITION METHODS AND NUMERICAL RESULTS 12

2.1. Sliding-Window Fitting Method 13
2.2. Hilbert-Huang Transform 15
2.2.1. Empirical Mode Decomposition 16
2.2.2. Polynomial Curve Fitting 20
2.2.3. Improvement on EMD 22
2.2.4. Hilbert Transform 27
2.3. Conjugate Pair Decomposition Method 29
2.4. The New Program 31
2.5. Numerical Analysis and Results 32

CHAPTER 3: NUMERICAL INTEGRATION AND DIFFERENTIATION AND GYRO SIGNAL FABRICATION 39

3.1. Numerical Integration Method 39
3.2. Numerical Differentiation Method 40
3.3. Numerical Integration and Differentiation Results 43
3.4. Fabrication of Right Foot Gyroscope Signal for ELL 48

CHAPTER 4: SENSORS CONDITIONING AND NUMERICAL RESULTS 52

4.1. Theoretical Algorithm 53
4.2. Dual-Accelerometer Test 56
4.2. Accelerometer-Videogrammetry Test 63
4.2.1. Calculation of Rotation Angles 74
4.2.2. Theoretical Correction of Acceleration 79
4.3. Empirical Correction Method 83
4.4. Normal Ranges of Head and Pelvis Rotation Angles 90

CHAPTER 5: SUMMARY AND RECOMMENDATIONS 93

5.1. Summary of Research 93
5.2. Recommendations for Future Works 94

REFERENCES 95

APPENDICES:

A. Means and Standard Deviation of DiffMax and DiffMin of Head Movement of Real Trotting Horses 97
B. Results from Single Accelerometer Tests and Accelerometer-Videogrammetry Tests 117
C. Rotation Angles of Head and Pelvis of Trotting Horses.....128

LIST OF ILLUSTRATIONS

Figures Page

1.1. A complete trot [4] 2

1.2. A horse with a camera-based motion analysis system. 3

1.3. DiffMax and DiffMin in a trot cycle 4

1.4. Four types of lameness 4

1.5. A wireless gyroscope (middle) and to wireless accelerometers [2] 5

1.6. A motion measurement system with three wireless sensors 6

1.7. The flowchart of ELL program 7

1.8. True and integrated vertical position 8

1.9. Vertical position of a horse's head during a trot with complicated moving average 9

2.1. Two cubic spline envelopes 16

2.2. EMD: (a) u and m_{11}, and (b) the remainder c_{11}. 17

2.3. EMD: (a) original signal u, and (b) the first IMF c_1 and the residue r_1 18

2.4. EMD: (a) u and $m_{1\ 20}$, and (b) the first IMF c_1 and the residue r_1 20

2.5. Normal EMD procedure: (a) $u(t)$ and m_{11}, and (b) c_{11} 23

2.6. Improved EMD procedure with 4 added extrema: (a) $u(t)$ and m_{11} and (b) c_{11} 25

2.7. Two extended ends for EMD analysis 27

2.8. Instantaneous frequency and amplitude from HHT analysis 28

2.9. Result from HHT-CPD-end analysis: (a) instantaneous amplitude and (b) instantaneous frequency.....31
2.10. The new ELL program using the HHT-CPD-end method.....32
2.11. Standard deviations of DiffMax from the HHT with EE improvement and the SWF 36
2.12. Standard deviations of DiffMax from the HHT with EE improvement and the SWF 37
2.13. Standard deviations of DiffMax from the HHT with ISBM improvement and the SWF 38
3.1. The trapezoidal rule for numerical integration 40
3.2. Directly measured acceleration and acceleration from single curve fitting.....42
3.3. Directly measured acceleration and acceleration from double curve fitting 43
3.4. Acceleration from double curve fitting and the ideal acceleration 44
3.5. The differentiated-integrated position and the ideal data 45
3.6. The differentiated-integrated numerical position and the camera-measured position from the accelerometer-videogrammetry test 46
3.7. Acceleration from double curve fitting and the ideal acceleration signal of an 8-Hz harmonic.....47
3.8. The position from double integrations and the sampled curve of a 32-Hz harmonic 48
3.9. Finding the local maxima of $a(t)$ 49
3.10. Every other maximum value is multiplied by -1 50
3.11. The created gyroscope signal and the original acceleration signal.....51

4.1. The main rotation directions of a horse's head and pelvis.....53
4.2. Acceleration components of an accelerometer 54
4.3. The dual-accelerometer test apparatus.....57
4.4. Accelerations from both sensors in the dual-accelerometer test: (a) accelerations, and (b) absolute error. 58
4.5. Integrated head and pelvis position signals from the dual-accelerometer test: (a) positions, and (b) absolute error.....59
4.6. Dual-accelerometer test with a ball bearing: (a) head and pelvis acceleration signals, and (b) absolute pointwise error 63
4.7. The accelerometer-videogrammetry test setup 64
4.8. A typical sensor motion during the accelerometer-videogrammetry test 65
4.9. Comparison of the sensor's acceleration and the camera's vertical acceleration..67
4.10. Comparison of the sensor's acceleration and the camera's vertical acceleration: (a) without correction, and (b) with correction on the sensor's acceleration.....69
4.11. Comparison of a sensor's acceleration and a camera's vertical acceleration from the accelerometer-videogrammetry test.....71
4.12. Comparison of a sensor's velocity and a camera's vertical velocity from the accelerometer-videogrammetry test.....72
4.13. The sensor's rotation angle α.....74
4.14. Rotation angle ranges in 84 accelerometer-videogrammetry test trials.....75
4.15. The sensor rotation angle caculated using the displacement data measured by the camera system.....76

4.16. Angular velocities measured by the gyroscope sensor and the camera system: (a) comparison of the two velocities, and (b) difference between the two velocities .78
4.17. Rotation angles measured by the gyroscope sensor and the camera system: (a) comparison of the two angles, and (b) difference between the two angles 79
4.18. Uncorrected and corrected acceleration signals.....80
4.19. The vertical acceleration from the camera data and the corrected vertical sensor acceleration 71
4.20. Linear relationship between the means of DiffMax from the use of two different signals 82
4.21. Linear relationship between the means of DiffMax from the use of two different signals 85
4.22. The original sensor acceleration and the vertical acceleration from the camera ...86
4.23. Vertical velocity signals from the sensor and the camera under the Type 1 lameness.....87
4.24. Numerical integration from velocity to position.....88
4.25. Vertical velocity signals from the sensor and the camera under the Type 3 lameness.....89
4.26. Head rotation angle ranges in real trotting horses 91
4.27. Pelvis rotation angle ranges in real trotting horses 91

Tables Page

2.1. Analysis of ideal head acceleration data 35

2.2. Analysis of ideal pelvis acceleration data 35

4.1. DiffMax and DiffMin from the dual-accelerometer test.....60

4.2. The maximum and minimum rotation angles in dual-accelerometer test.....62

4.3. Effects of different correction methods on DiffMax and DiffMin 84

WIRELESS SIGNAL ACQUISITION AND PROCESSING TECHNIQUES FOR HORSE LAMENESS DETECTION AND EVALUATION

Bao Anh Nguyen

Dr. P. Frank Pai, Thesis Advisor

ABSTRACT

The Equine Lameness Locator ® (ELL) is a newly developed system that provides a robust and objective method to detect and evaluate equine lameness. To achieve objective lameness evaluation, the system analyzes a horse's head and pelvis vertical movement signals during trotting. Two uniaxial accelerometers are placed on the horse's torso, one each on the horse's head and pelvis to record vertical accelerations. Vertical position signals are obtained by numerical double integration of the acceleration signals. However, these integrated position signals contain very large moving averages and require advance methods of signal processing for correction. In this thesis, a combination of the Hilbert Huang transform and a conjugate-pair decomposition method is proposed and tested against the current ELL's signal processing method, a sliding-window curve-fitting method. Numerical simulations and experimental results show that the proposed new method involves more intense computation but does not provide better results for lameness evaluation of horses. Hence, the original sliding-window curve-fitting method is recommended for future use.

Clinical and experimental observations reveal that a horse's head and pelvis also rotate during trotting. These rotations may cause inaccurate measurements of the true vertical accelerations. Hence, this work also numerically and experimentally examines the

influences of rotations on the measured vertical accelerations. Numerical techniques, unique experimental devices and setups, and an algorithm for correcting accelerometer outputs to obtain true vertical accelerations have been developed and experimentally validated.

Chapter 1: INTRODUCTION

1.1. Introduction

Limb lameness is one of the most common medical conditions in horses; it causes annual loss of hundreds of million dollars to horse owners [1]. Unfortunately, detecting mild and multiple limb lameness by observation alone is a great challenge for veterinarians. Research has shown that, even experienced veterinarians may disagree on the presence of lameness and its severity, especially in mild or multiple limb lameness [2]. The Equine Lameness Locator (ELL) developed by Equinosis is a breakthrough in equine practice because it provides an easy to use, objective method for detection and evaluation of lameness in the field. ELL uses a set of body-mounted wireless sensors to measure translational and rotational motions at three different locations on a horse to detect, characterize and evaluate lameness [1-3]. While ELL is an objective method, certain limitations on accuracy and repeatability of measurement and lameness prediction still exist. This research aims to improve the accuracy and efficiency of the hardware setup, signal processing, and computer program of ELL.

1.2. Equine Lameness Locator

The Equine Lameness Locator ® (ELL) is a locomotion-based hardware-software system for detection and evaluation of limb lameness in horses [2]. It is developed by Prof. Kevin Keegan (Department of Veterinary Medicine and Surgery, College of Veterinary Medicine), Prof. P. Frank Pai (Department of Mechanical and Aerospace Engineering, College of Engineering) of the University of Missouri, and Prof. Yoshiharu Yonezawa of

the Hiroshima Institute of Technology, Japan. At the beginning, Dr. Keegan recognized the essential role of an objective method to detect and evaluate mild or multiple lameness in horses. He spent many years studying the relationship between limb lameness and motion of various points on a trotting horse. Trotting is a two-beat diagonal gate in horses, as shown in Figure 1.1. During a trot, each pair of diagonal limbs moves together [4]. Also, a right stance is the moment during which the horse's right front limb touches the ground. A left stance is the moment during which the horse's left front limb touches the ground.

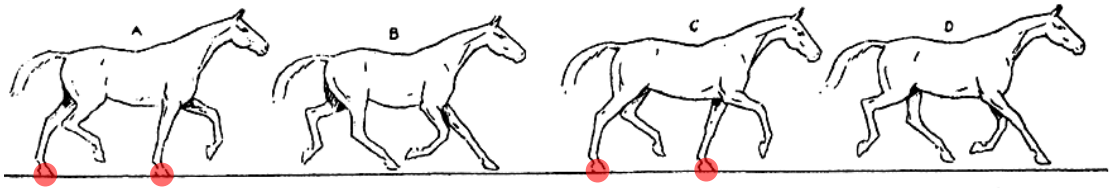

Figure 1.1: A complete trot.

Using a high-speed camera system as shown in Figure 1.2, Dr. Keegan measured the time-varying coordinates of retro-reflective markers on various positions of a horse under study. He investigated the relationship between limb lameness and vertical displacements of head and pelvis during a trot. A horse moves its head and pelvis up and down twice during each complete trot cycle, reaching two maximum and two minimum vertical positions [3]. Results showed that the difference between two adjacent maximum positions and that between two adjacent minimum positions are highly correlated with presence of lameness and its severity. Also the time occurrences of these maximum and minimum positions in accordance with right stance or left stance phase characterize the lameness and narrow the identification of the location of lameness with the limb.

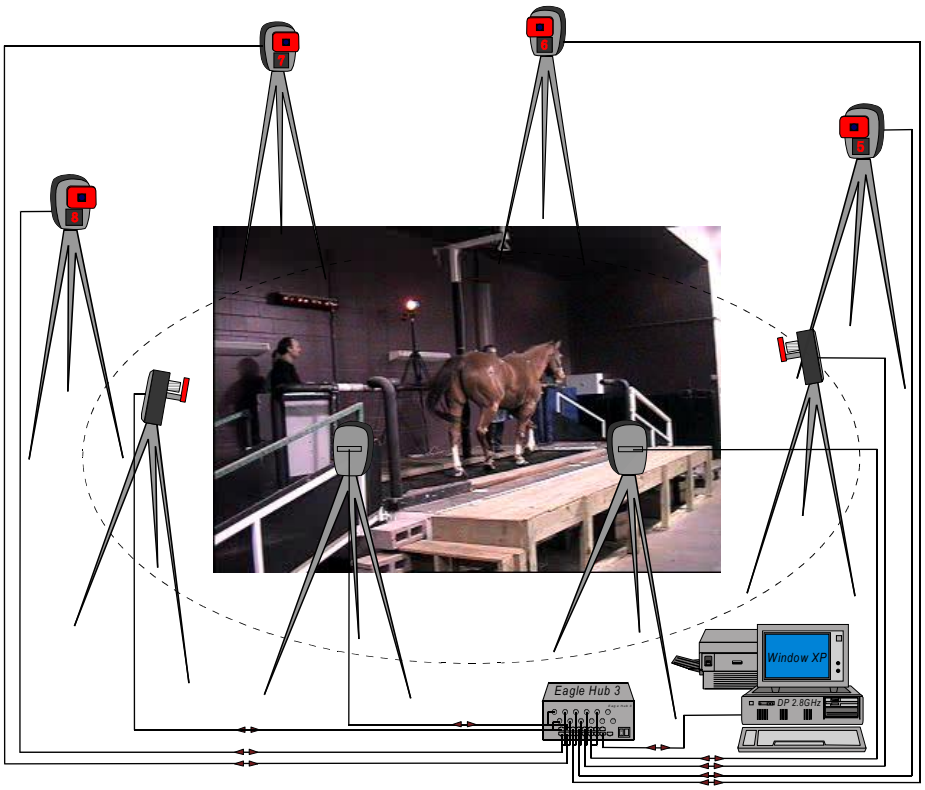

Figure 1.2: A horse with a camera-based motion analysis system.

For convenience, we define DiffMax as the difference between two adjacent maximum positions and DiffMin as the difference between two adjacent minimum positions, as shown in Figure 1.3. A sound horse has its head and pelvis moving up and down in a uniform, sine-wave like pattern [3], and the absolute values of DiffMax and DiffMin from head and pelvis motions should be very close to zero ($<6\,\text{mm}$ for the head and $<3\,\text{mm}$ for the pelvis). On the other hand, a unilaterally lame horse has its head and pelvis moving asymmetrically because the lameness causes a perturbation to the vertical harmonic motions of the head and pelvis [3]. Then, DiffMax and DiffMin deviate from zero [2]. The combination of DiffMax and DiffMin can indicate four different types of lameness.

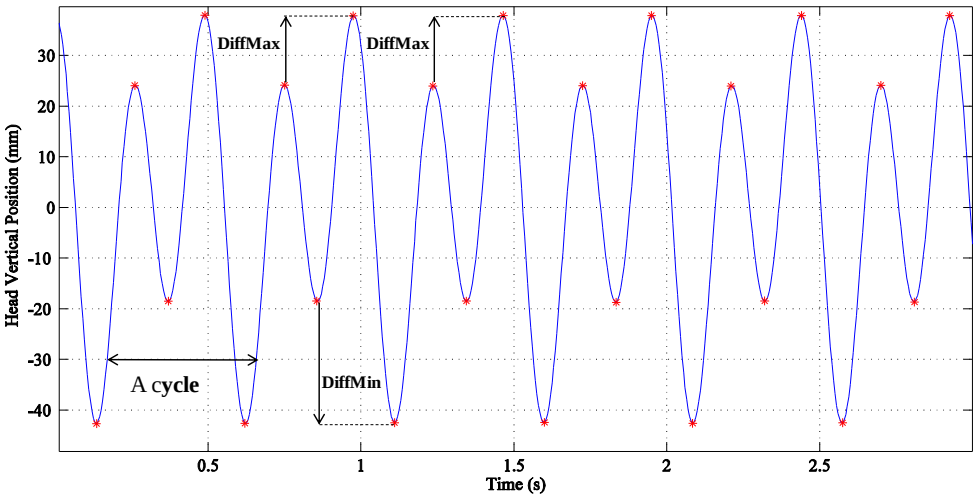

Figure 1.3: DiffMax and DiffMin in a trot cycle.

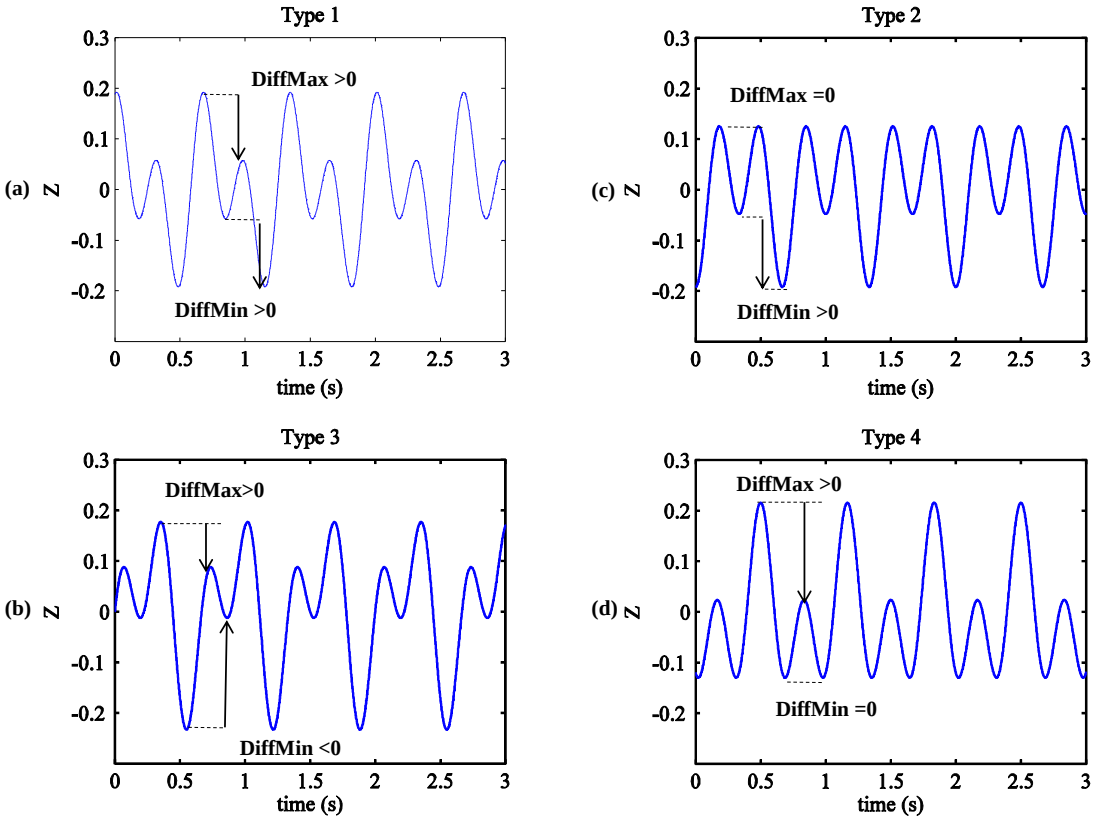

Figure 1.4: Four types of lameness.

Figure 1.4 illustrates vertical motions of an equine head (or pelvis) of four typical types of lameness. For Type 1 lameness, DiffMax and DiffMin have the same sign. Type 2 lameness has DiffMax almost equal to zero while DiffMin can be either positive or negative. For Type 3 lameness, DiffMax and DiffMin have opposite sign. And, Type 4 lameness has DiffMin close to zero while DiffMax is significantly different from zero.

However, there are two major challenges associated with the use of this camera-based motion analysis system. First, such a camera measurement system is very expensive and takes time to set up. Second, training a horse to naturally trot on a treadmill is expensive and time-consuming because it takes a few days for training and hospitalization is needed. Dr. Pai and Dr. Yonezawa helped improving the ELL system to overcome those difficulties by developing the current version of Equine Lameness Locator ®. The current system uses three wireless sensors to collect motion signals from a horse and a laptop to receive and analyze those signals, as shown in Figures 1.5 and 1.6.

Figure 1.5: A wireless gyroscope (middle) and two wireless accelerometers [2].

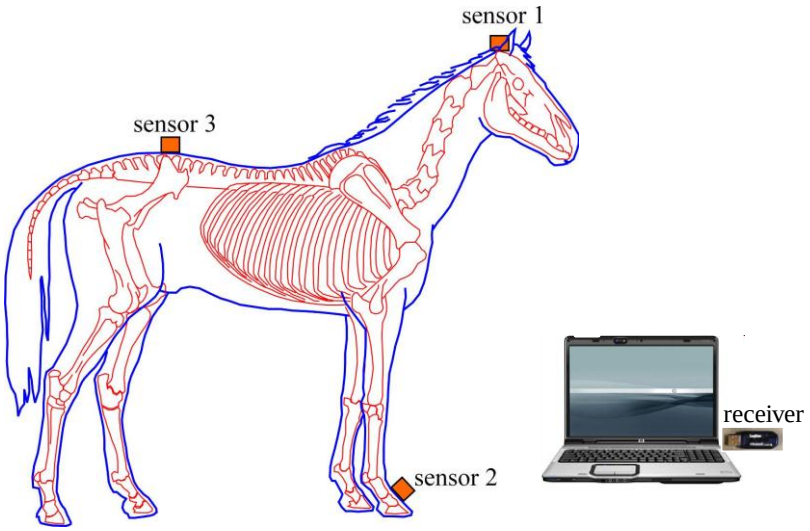

Figure 1.6: A motion measurement system with three wireless sensors.

Sensor 2 is a gyroscope attached to the right front limb of the horse, measuring the angular velocity of the limb. This signal helps ELL identify the time segments during which the horse trots regularly. Also, it provides ELL the time occurrences of right and left stance phases. Sensors 1 and 3 are two accelerometers placed at the head and pelvis, recording vertical accelerations of these two locations [1-3,5-8]. The received accelerations are double integrated to give vertical displacements of the head and pelvis. Then, ELL calculates the main variables DiffMax and DiffMin from both head and pelvis vertical displacements to detect and evaluate severity of lameness. Finally, ELL compares the time segments of right and left stance phases with the maximum and minimum head and pelvis positions to identify the type and location of lameness. The flowchart of ELL program is shown in Figure 1.7.

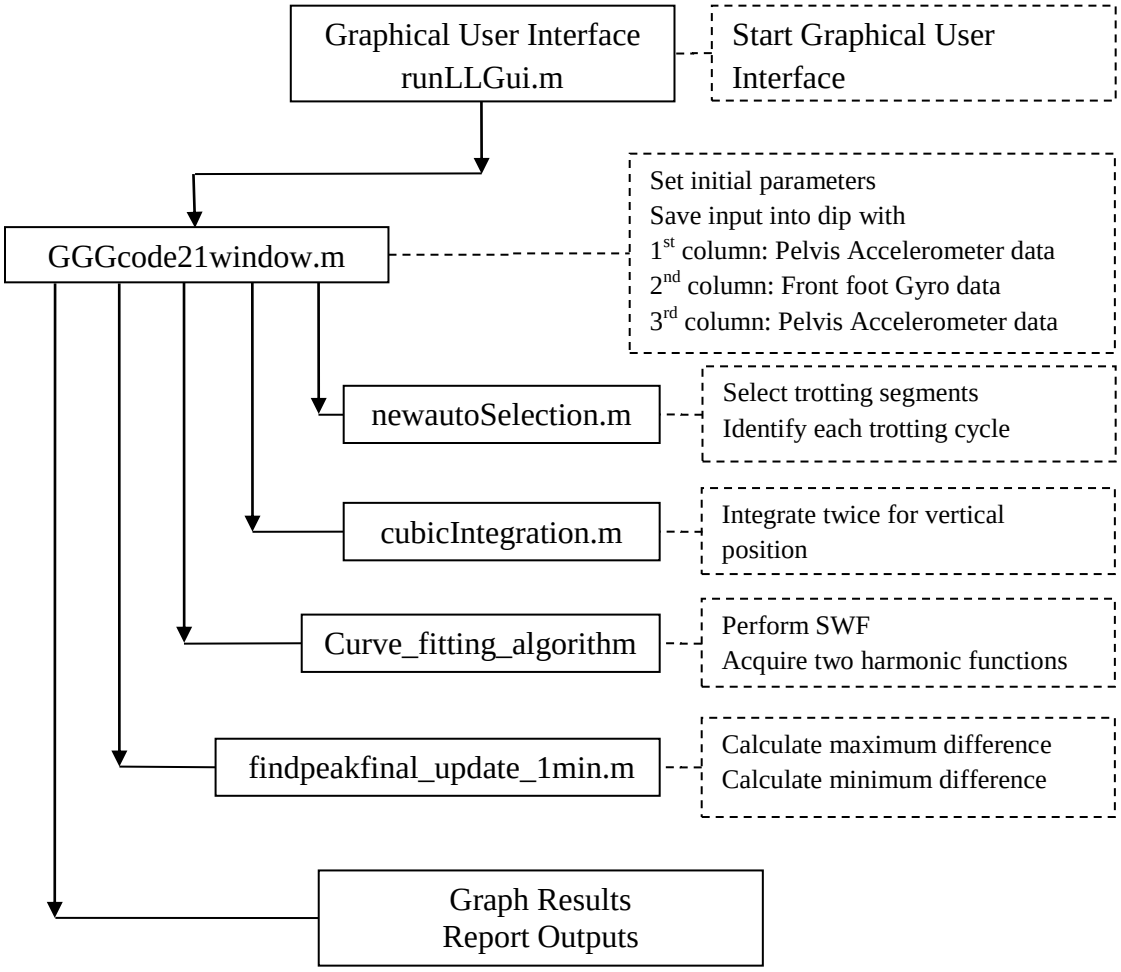

Figure 1.7: The flowchart of ELL program.

With these improvements, ELL is more compact and robust and much cheaper than the camera-based system. It is easy to set up and can be used for on-site testing without hospitalizing and training the horse to run on a treadmill. Also, the horse owner can watch the whole process. However, the current ELL also comes with its own challenges.

1.3. Motivation and Thesis Organization

While it eliminates the two main limitations posed by the camera system, the current ELL also faces a number of obstacles. First, such wireless accelerometers used in the current ELL only measure accelerations, but numerical lameness indicators are derived from displacements [1-3, 5-8]. Second, there are limitations and issues about the accuracy and attachment of the wireless MEMS sensors shown in Figure 1.5.

Integrating accelerations into displacements for lameness detection is a challenging numerical process. Such displacements acquired directly from double integration contain very large moving average and certain amount of noise due to integration error and extraneous movement of the horse.

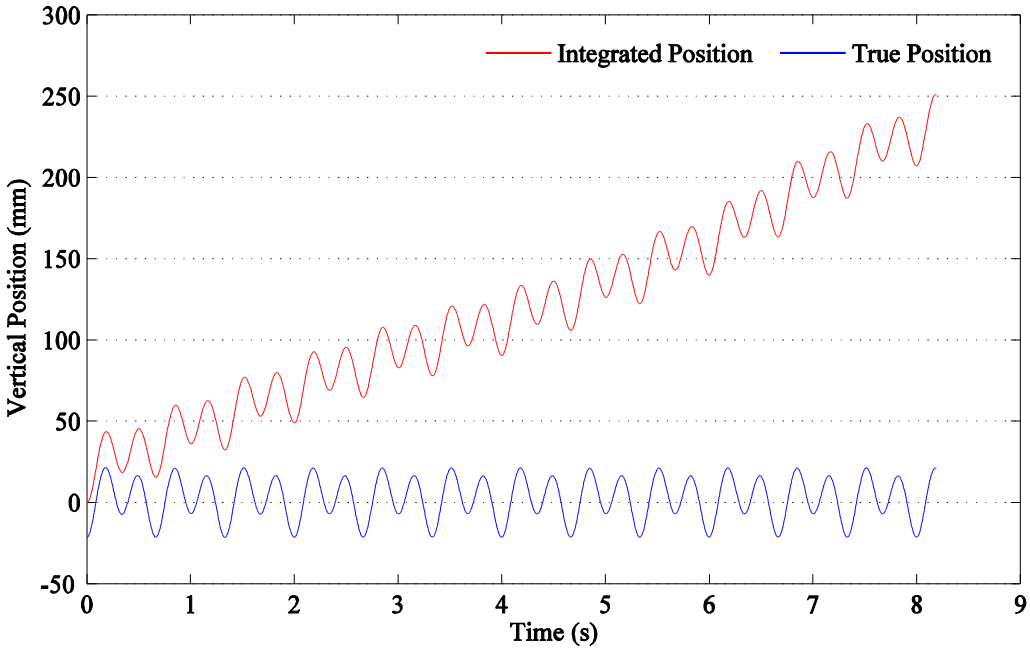

Figure 1.8: True and integrated vertical positions.

Figure 1.8 shows two position signals from one of our experiments presented later in Chapter 3. One is a very accurate vertical position signal, while the other is obtained by double integration of the acceleration measured by an accelerometer. Since this is a controlled experiment, the moving average seems to have a simple form, a straight line. However, it is still very large comparing with the true position signal. Furthermore, the moving average of real horse data can have a much more complicated form as shown in Figure 1.9.

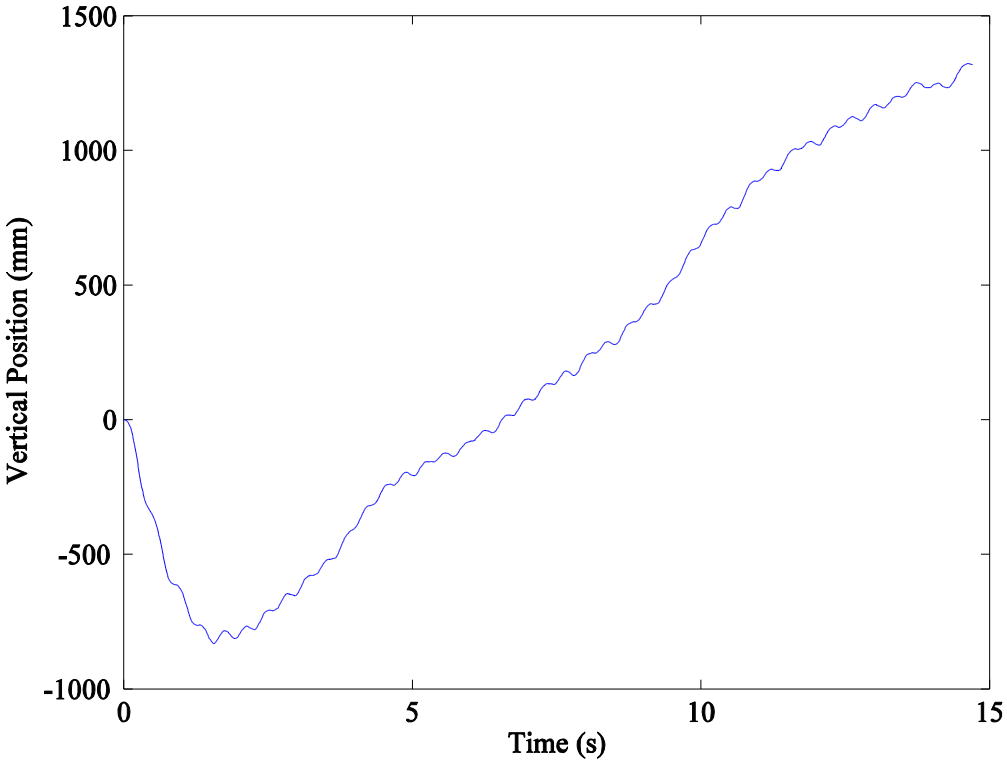

Figure 1.9: Vertical position of a horse's head during a trot with complicated moving average.

Hence, obtaining true vertical displacements from measured accelerations of the head and pelvis requires advanced signal processing techniques. Currently, ELL uses Dr. Pai's sliding-window fitting (SWF) algorithm to remove noise and moving average. Based on

the displacements measured using a high-speed camera system (see Figure 1.2), the vertical movement of a trotting horse's head (or pelvis) is observed to contain three basic components. They are two harmonic components with frequencies about 3 – 4 Hz and 1.5 – 2 Hz, representing the sound trot movement and the unilateral limb lameness movement, respectively. Moreover, a moving average represents the horse's extraneous movement and possible integration errors due to non-zero initial conditions and others. The sliding-window fitting uses this assumption to decompose a vertical movement signal into two harmonics and one moving average. Recently, Hilbert Huang transform (HHT) is developed as a very powerful tool for signal decomposition without assuming the frequencies of the harmonic components. Hence, we want to examine whether ELL can be more accurate and efficient if the current SWF is replaced with the HHT for signal processing.

Moreover, the measured acceleration signals themselves may not be accurate due to rotations of the head and pelvis. When trotting, a horse's head and pelvis not only move up and down but also rotate with respect to different axes. However, the accelerometers shown in Figure 1.5 only measure accelerations in the direction perpendicular to their top surfaces. Hence, the measured accelerations can be different from the wanted vertical accelerations. This research is also to develop a method for obtaining accurate vertical accelerations by correcting the measured accelerations using the measured signals from the three sensors and two additional gyroscopes, one on the head and one on the pelvis.

The two main goals of this research are discussed in more details in subsequent chapters. Chapter Two presents and compares different signal decomposition methods and numerical simulations. Then, the study concludes from the numerical studies and gives a

recommended signal decomposition method for the next version of ELL. Chapter three presents advanced numerical integration and differentiation techniques. Chapter four presents different approaches for conditioning and improving the measured accelerations. It also shows how to use the gyroscope signals to calculate real rotation angles of the horse's head and pelvis during a trot. Then, it concludes whether the measured accelerations need to be revised to account for the influences of rotations and provides the appropriate algorithm. Chapter five summarizes all the tasks performed in this thesis and draws some conclusions. It also provides some possible future works for this area of research.

Chapter 2: SIGNAL DECOMPOSITTION METHODS AND NUMERICAL RESULTS

The Equine Lameness Locator ® (ELL) is currently using a sliding-window fitting method (SWF) to process a horse's vertical movement signals during trotting for lameness detection and evaluation. In order to further improve the accuracy and efficiency of ELL, this work is to examine the use of two newly developed signal processing techniques: Hilbert Huang transform (HHT) and conjugate-pair decomposition (CPD). HHT is suitable for decomposing nonlinear and non-stationary signals [9], such as the vertical motion signals of horses studied in this thesis. However, HHT cannot provide accurate instantaneous frequencies and amplitudes at the beginning and ending of a signal due to Gibbs' effect. On the other hand, CPD improves SWF and can track the instantaneous frequency and amplitude of a signal without being affected by Gibbs' effect. Hence, we propose a hybrid HHT-CPD method that uses HHT to decompose the middle segment of a signal and CPD to track frequencies and amplitudes of the beginning and ending segments of that signal. For convenience, we call this HHT-CPD-end method. This chapter first describes and explains all signal decomposition methods mentioned above along with some improvements for this particular application. Second it compares numerical results obtained by using SWF and HHT-CPD-end methods. And third, it discusses and decides a signal decomposition method for use in the next version of ELL.

2.1. Sliding-Window Fitting Method

The sliding-window fitting (SWF) is a technique that can perform time-frequency analysis. While there are several versions of SWF used in the research community [8,9], Pai used in ELL a particular set of functions to perform SWF [8]. Because the vertical displacement of a horse's head or pelvis contains only three components as mentioned in Chapter one, such a displacement signal $z(t)$ can be assumed to be a combination of two harmonic functions with frequencies ω and 2ω, and a moving average described by a cubic polynomial as [8]

$$z(t) = e_1 \cos(\omega t) + e_2 \sin(\omega t) + e_3 \cos(2\omega t) + e_4 \sin(2\omega t) + e_5 + e_6 t + e_7 t^2 + e_8 t^3 \qquad (2.1)$$

If we define a shifted time $\bar{t} \equiv t - t_s$ with t_s being the time instant under observation, Eq. (2.1) can be rewritten as

$$z(\bar{t}) = C_1 \cos(\omega \bar{t}) + C_2 \sin(\omega \bar{t}) + C_3 \cos(2\omega \bar{t}) + C_4 \sin(2\omega \bar{t}) + C_5 + C_6 \bar{t} + C_7 \bar{t}^2 + C_8 \bar{t}^3 \qquad (2.2)$$

where

$$\begin{aligned} &C_1 \equiv \sqrt{e_1^2 + e_2^2} \cos(\omega t_s - \phi_1),\ C_2 \equiv -\sqrt{e_1^2 + e_2^2} \sin(\omega t_s - \phi_1),\ \tan\phi_1 \equiv \frac{e_2}{e_1} \\ &C_3 \equiv \sqrt{e_3^2 + e_4^2} \cos(2\omega t_s - \phi_2),\ C_4 \equiv -\sqrt{e_1^2 + e_2^2} \sin(2\omega t_s - \phi_2),\ \tan\phi_2 \equiv \frac{e_4}{e_3} \\ &C_5 \equiv e_5 + e_6 t_s + e_7 t_s^2 + e_8 t_s^3,\ C_6 = e_6 + 2e_7 t_s + 3e_8 t_s^2,\ C_7 \equiv e_7 + 3e_8 t_s,\ C_8 = e_8 \end{aligned} \qquad (2.3)$$

If $Z(t)$ is the measured displacement, the frequencies ω and 2ω can be identified from the two peaks of the spectrum of $Z(t)$ obtained using fast Fourier transform (FFT). Then the coefficients C_j $(j = 1...8)$ can be calculated by curve fitting through minimizing the square error Er defined as

$$Er = \sum_{i=-m}^{m} \alpha_i (z_i - Z_i)^2 \tag{2.4}$$

where α_i is a weighting factor chosen to be $\alpha_i = 1/\left(1+99\left|i\right|/m\right)$, and m is the number of points from each side of the point at t_s. Numerical simulations show that $2m\Delta t$ (Δt is the constant sampling step) needs to be greater or equal to two periods of the lowest harmonic (i.e., $4\pi/\omega$) [8]. In other words, $m\Delta t \geq 2\pi/\omega$ is needed. Note that the sampling step Δt is determined by the sampling frequency f_s chosen for data acquisition. For the cases presented in this work, $f_s = 200$ Hz is used, and hence $\Delta t = 0.005\ s$.

It follows from Eq. (2.4) that the error is minimized when

$$\frac{\partial Er}{\partial C_j} = 0,\ j = 1,...,8 \tag{2.5}$$

In other words,

$$\sum_{i=-m}^{m} 2\alpha_i (z_i - Z_i) \frac{\partial z_i}{\partial C_j} = 0,\ j = 1,...,8 \tag{2.6}$$

The C_j ($j = 1...8$) can be obtained by solving the eight algebraic equations shown in Eq. (2.6). Since at $\bar{t} = 0$ (i.e., $t = t_s$), $z(0) = C_1 + C_3 + C_5$. It indicates that the horse's head or pelvis vertical position consists of the lameness harmonic component C_1, the normal harmonic component C_3, and the moving average C_5. Also, it follows from Eq. (2.3) that

$$\phi_1 = \tan^{-1}\frac{e_2}{e_1} = \omega t_s - \theta_1, \quad \theta_1 \equiv \tan^{-1}\frac{-C_2}{C_1}$$
$$\phi_2 = \tan^{-1}\frac{e_4}{e_3} = 2\omega t_s - \theta_2, \quad \theta_2 \equiv \tan^{-1}\frac{-C_4}{C_3} \tag{2.7}$$

Because e_i $(i = 1,2,3,4)$ are constants and hence ϕ_1 and ϕ_2 are constants, the frequencies can be calculated using finite difference as

$$\omega = \frac{d\theta_1}{dt} \approx \frac{\sum_{i=-1}^{2}[\theta_1(t_s + i\Delta t) - \theta_1(t_s + (i-1)\Delta t)]}{4\Delta t}$$
$$2\omega = \frac{d\theta_2}{dt} \approx \frac{\sum_{i=-1}^{2}[\theta_2(t_s + i\Delta t) - \theta_2(t_s + (i-1)\Delta t)]}{4\Delta t} \tag{2.8}$$

Finally, the relative error can be calculated as the difference between the fitted and the original data divided by $Z(t)$. The fitting accuracy is measured by the standard deviation of the relative error calculated above [8].

2.2. Hilbert-Huang Transform

Hilbert-Huang transform (HHT) is a time-frequency signal processing method often used to process nonlinear and non-stationary signals [10-14]. It is recently developed, but is well known among researchers because of its unique features. Hilbert-Huang transform composes of two steps: first, decomposing a signal into intrinsic mode functions (IMFs) using the empirical mode decomposition (EMD), and second, calculating the instantaneous frequency and amplitude of each IMF using Hilbert transform (HT). Intrinsic mode functions are functions that have the number of extrema equal or different from the number of zero crossing by one in the whole data length. Each IMF has two envelopes defined respectively by the local maxima and minima and the average of these two envelopes is about zero [10].

2.2.1. Empirical Mode Decomposition

Empirical mode decomposition separates a time-domain signal $u(t)$ into n IMFs $c_i(t)$ $(i = 1...n)$ as

$$u(t) = \sum_{i=1}^{n} c_i(t) + r_n \tag{2.9}$$

where r_n is the residue. First, EMD searches for local maxima and minima of the signal. Then it connects each of the set of local maxima and the set of local minima with a natural cubic spline curve, as shown in Figure 2.1. Ideally, the envelopes should cover the whole signal, but in reality, the envelopes may overshoot or undershoot the signal, especially at the beginning and ending segments [10].

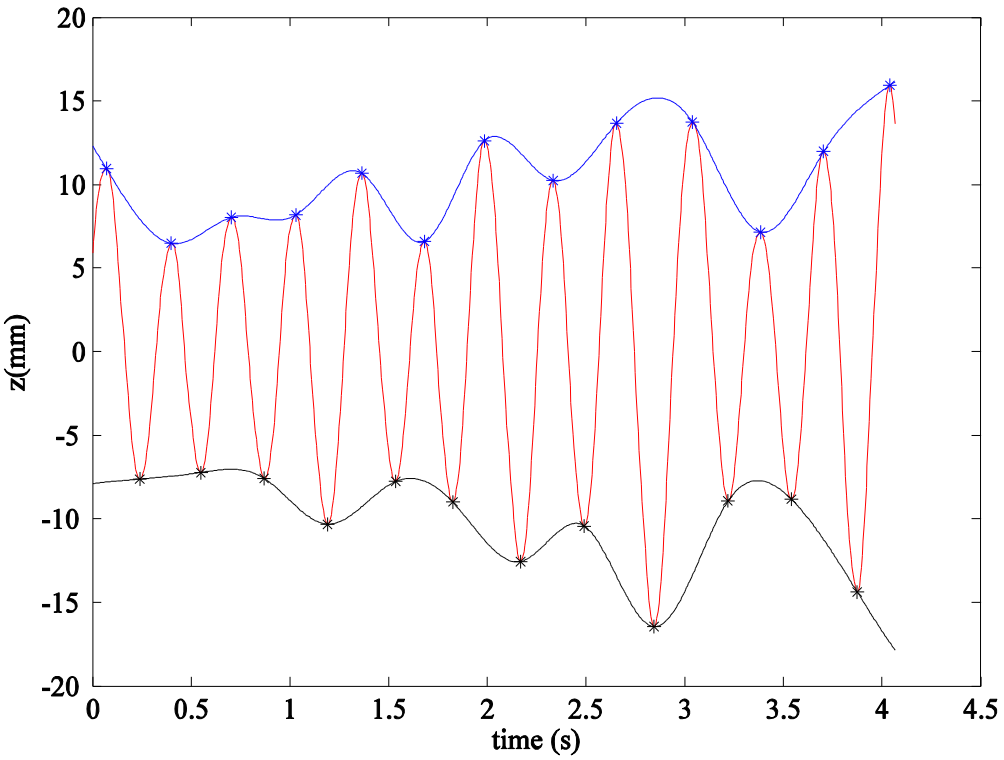

Figure 2.1: Two cubic spline envelopes.

Next, EMD subtracts the mean of the two envelopes, m_{11}, from the signal $u(t)$ and treats the remainder c_{11} defined below and shown in Figure 2.2 as a new signal:

$$c_{11} = u(t) - m_{11} \tag{2.10}$$

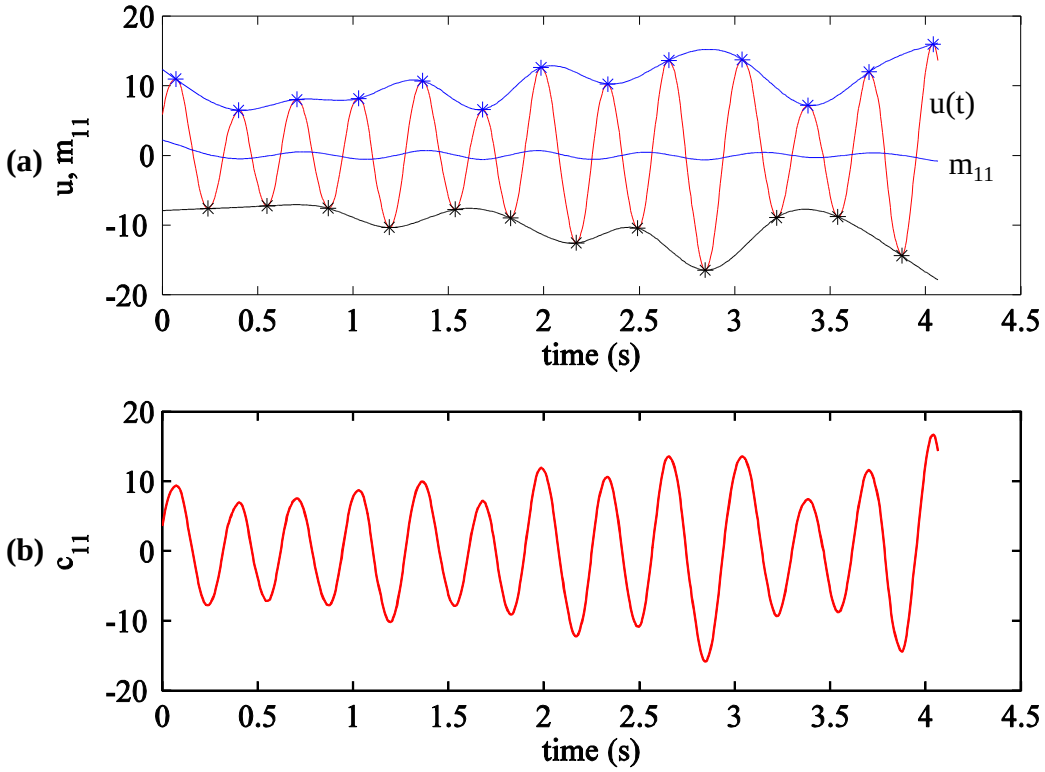

Figure 2.2: EMD: (a) u and m_{11}, and (b) the remainder c_{11}.

These steps are repeated K times until the two envelopes are symmetric with respect to the zero line, and hence m_{1K} is close to zero. Then the remainder of the signal is taken as the first IMF as shown in Figure 2.3 and

$$c_{1k} = u - m_{11} - m_{12} - \ldots - m_{1k} = c_{1(k-1)} - m_{1k},\ k = 2, \ldots, K \tag{2.11}$$

where c_{1k} is the next new signal, $c_{1(k-1)}$ is the previous new signal, and m_{1k} is the average of envelopes at step k. After K steps, c_{1K} is taken as the first IMF c_1, and $r_1 (\equiv u - c_1 = m_{11} + \cdots + m_{1K})$ is treated as a new signal to extract the second and other IMFs. Figure 2.3 compares the original signal $u(t)$ with c_1 $(= c_{1\,20})$ and r_1 after 20 (=K) iterations. This shifting process is performed until enough IMFs are obtained or until the remainder becomes a monotonic function. A monotonic function increases or decreases continuously over the entire signal length, and it cannot be further decomposed into IMFs.

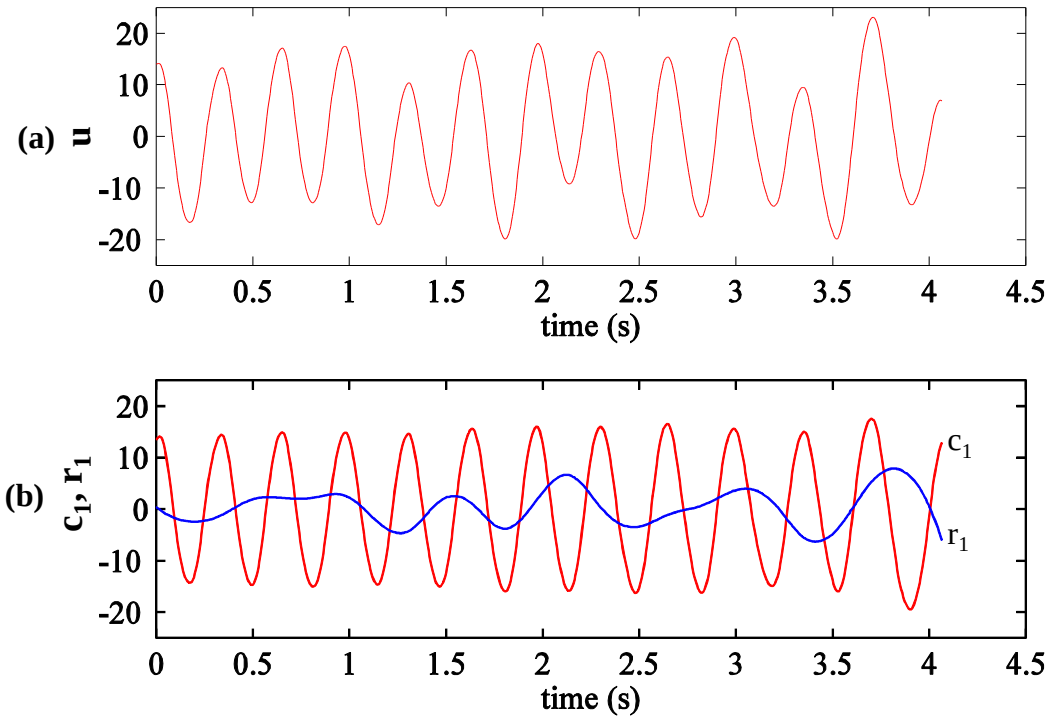

Figure 2.3: EMD: (a) original signal *u*, and (b) the first IMF c_1 and the residue r_1.

The maximum and minimum envelopes, however, are not always perfectly symmetric; or it may take a great number of iterations until they are symmetric. To reduce the

computational time while maintaining adequate accuracy, a deviation D_v defined below is calculated between the two consecutive sifting results in order to set a standard for stopping the iteration:

$$D_v \equiv \sqrt{\frac{\sum_{i=1}^{N}[c_{1k}(t_i)-c_{1k-1}(t_i)]^2}{\sum_{i=1}^{N}c_{1k-1}^2(t_i)}} \tag{2.12}$$

where $t_i = i\Delta t$ and $T = N\Delta t$ is the sampling period. Another method to limit the computational time is to set the maximum number of iterations. In this work, $D_{v\max}$ is set to be 0.001, and the maximum number of iterations is set to be 20. The iteration will stop when one of these two criteria is met.

Empirical mode decomposition (EMD) is driven by the natural characteristic of the data itself, specifically the maxima and minima of the signal. Because the shifting process does not assume the form of the processed signal, EMD is more objective than other traditional signal decomposition techniques, such as fast Fourier transform (FFT) and wavelet transform (WT) [15,16] . However, EMD cannot accurately decompose a signal with a fast changing moving average. If the moving average fluctuates significantly over time, it may hide some local maximum and minimum points such that EMD cannot identify them. Also, for a local maximum (or minimum) right next to one data end, there are not enough maximum points to fit a cubic spline and hence $\ddot{u} = 0$ is assumed in a natural cubic spline. Therefore, the maximum and minimum envelope splines are inaccurate at the data ends. Because EMD fits local maxima and minima using two natural cubic spline curves, the extracted IMFs may have large errors at the beginning and ending segments of the signal, as shown in Figure 2.4.

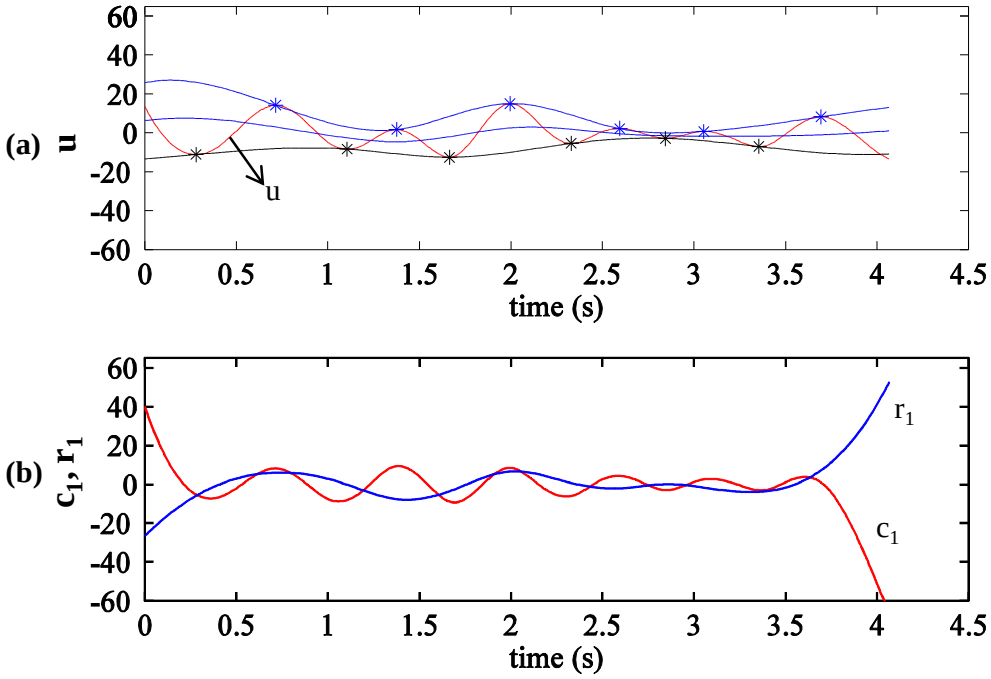

Figure 2.4: EMD: (a) u and $m_{1\ 20}$, and (b) the first IMF c_1 and the residue r_1.

For the purpose of horse lameness detection studied in this work, EMD is used to extract only two IMFs c_1 and c_2, which are the two main harmonic components caused by the four-legged locomotion. The remainder is the moving average. However, because the vertical displacements of head and pelvis are obtained by double integrations on the measured vertical accelerations, they often contain very large, fluctuating moving averages. Hence, we derive methods to remove the moving average by polynomial curve fitting and to improve the accuracy of the EMD process around the two data ends, as shown next.

2.2.2. Polynomial Curve Fitting

Each displacement signal in ELL is subtracted by a high-order polynomial in order to remove its large moving average introduced by double integration. The order of the

polynomial is estimated based on the frequency and the general length of the displacement signal. Also, each polynomial is found by using the least-square fitting method. The best-fit polynomial should follow the signal's global trend, instead of local trends. Clearly, a low-order polynomial cannot resemble the global average very well because of extraneous movement of the horses. On the other hand, a high-order one will fit the data to every detail. For this application, we decided to use sixth-order polynomials based on the frequencies of the harmonics (about 2 Hz and 4 Hz) and the general minimum length of the signal (around 10 seconds). A sixth-order polynomial may have five peaks, three maxima and two minima or reverse. Hence, for a 10-second segment, the frequency of either maximum or minimum is about 0.2 Hz, which is much lower than the two interested frequencies. Therefore, even for a slightly shorter data segment, removing a fitted sixth-order polynomial from the signal is not likely to affect the two important harmonics. A sixth-order polynomial $P(t)$ has the form

$$P(t) = C_0 + C_1 t + C_2 t^2 + C_3 t^3 + C_4 t^4 + C_5 t^5 + C_6 t^6 \tag{2.13}$$

Hence, the sum of squared errors, *SE*, between the original signal $u(t)$ and the polynomial is

$$SE = \sum_{i=1}^{n} (C_0 + C_1 t + C_2 t^2 + C_3 t^3 + C_4 t^4 + C_5 t^5 + C_6 t^6 - u(t))^2 \tag{2.14}$$

where n is the total number of data points. The unknown coefficients C_j $(j = 0,...,6)$ can be obtained by minimizing SE as

$$\frac{\partial SE}{\partial C_j} = 0, \ (j = 0,...,6) \tag{2.15}$$

Or

$$\sum_{i=1}^{n}\begin{bmatrix} 1 & t & t^2 & t^3 & t^4 & t^5 & t^6 \\ t & t^2 & t^3 & t^4 & t^5 & t^6 & t^7 \\ t^2 & t^3 & t^4 & t^5 & t^6 & t^7 & t^8 \\ t^3 & t^4 & t^5 & t^6 & t^7 & t^8 & t^9 \\ t^4 & t^5 & t^6 & t^7 & t^8 & t^9 & t^{10} \\ t^5 & t^6 & t^7 & t^8 & t^9 & t^{10} & t^{11} \\ t^6 & t^7 & t^8 & t^9 & t^{10} & t^{11} & t^{12} \end{bmatrix}\begin{Bmatrix} C_0 \\ C_1 \\ C_2 \\ C_3 \\ C_4 \\ C_5 \\ C_6 \end{Bmatrix} = \sum_{i=1}^{n}\begin{Bmatrix} u(t) \\ t\times u(t) \\ t^2\times u(t) \\ t^3\times u(t) \\ t^4\times u(t) \\ t^5\times u(t) \\ t^6\times u(t) \end{Bmatrix} \tag{2.16}$$

Numerical simulations show that a sixth-order polynomial does not always fit a signal's moving average very well. However, subtracting such a polynomial from a displacement signal from double integration always eliminates a significant part of the moving average and hence improves the conditions for and the results from EMD analysis.

2.2.3. Improvement on EMD

To help EMD work better at the two data ends, we adopt an improved slope-based method (ISBM) proposed by Wu and Qu [17]. Empirical mode decomposition is well known for being not accurate around the beginning and ending segments of a signal because there are not enough extrema to guide cubic spline curves. Hence, Dätig and Schlurmann [18] proposed a slope-based method (SBM) by adding a pair of maximum and minimum to each end of the signal. These extrema are generated based on the slope and characteristic time scale of the beginning and ending segments of the signal.

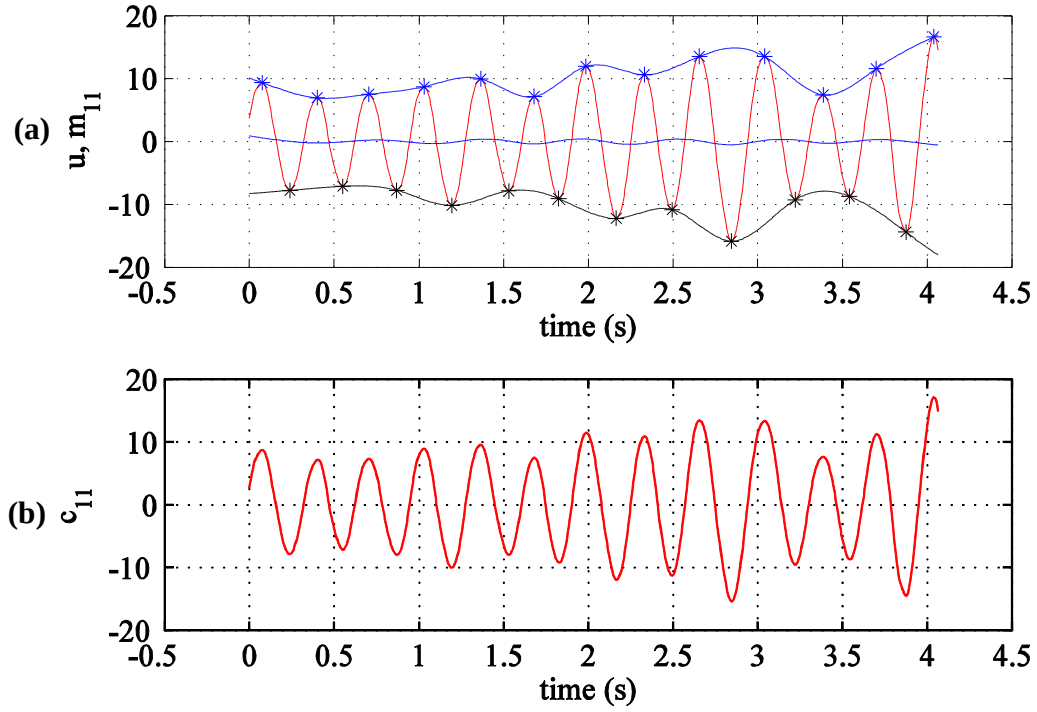

Figure 2.5: Normal EMD procedure: (a) $u(t)$ and m_{11}, and (b) c_{11}.

Figure 2.5 shows a normal EMD procedure. Now, let $U(i)$ and $t_U(i)$ and $L(i)$ and $t_L(i)$ be the ordinate and abscissa values of the i^{th} maximum and minimum, respectively. If the first and last extrema are both maxima, define the beginning minimum-peak slope s_1 and maximum-peak slope s_2 as follow

$$s_1 \equiv \frac{U(2)-L(1)}{t_U(2)-t_L(1)}$$
$$s_2 \equiv \frac{L(1)-U(1)}{t_L(1)-t_U(1)} \tag{2.17}$$

Also, the maximum-peak time gap $\Delta t_U(1)$ and the minimum-peak time gap $\Delta t_L(1)$ are defined as

$$\begin{aligned} \Delta t_U(1) &\equiv t_U(2) - t_U(1) \\ \Delta t_L(1) &\equiv t_L(2) - t_L(1) \end{aligned} \tag{2.18}$$

Then, the abscissa and ordinate values of an added beginning minimum are defined as

$$\begin{aligned} t_L(0) &\equiv t_L(1) - \Delta t_L(1) \\ L(0) &\equiv U(1) - s_1(t_U(1) - t_L(0)) \end{aligned} \tag{2.19}$$

The abscissa and ordinate values of an added beginning maximum are defined as

$$\begin{aligned} t_U(0) &\equiv t_U(1) - \Delta t_U(1) \\ U(0) &\equiv L(0) - s_2(t_L(0) - t_U(0)) \end{aligned} \tag{2.20}$$

Similarly, the ending minimum-peak slope s_3 and maximum-peak slope s_4 are defined as

$$\begin{aligned} s_3 &\equiv \frac{L(N) - U(N-1)}{t_L(N) - t_U(N-1)} \\ s_4 &\equiv \frac{U(N) - L(N)}{t_U(N) - t_L(N)} \end{aligned} \tag{2.21}$$

And the end maximum-peak time gap $\Delta t_U(N)$ and the end minimum-peak time gap $\Delta t_L(N)$ are

$$\begin{aligned} \Delta t_U(N) &= t_U(N) - t_U(N-1) \\ \Delta t_L(N) &= t_L(N) - t_L(N-1) \end{aligned} \tag{2.22}$$

Finally, the abscissa and ordinate values of an added ending minimum are defined as

$$\begin{aligned} t_L(N+1) &\equiv t_L(N) + \Delta t_L(N) \\ L(N+1) &\equiv U(N) + s_3(t_L(N+1) - t_U(N)) \end{aligned} \tag{2.23}$$

The abscissa and ordinate values of an added ending maximum are defined as

$$t_U(N+1) \equiv t_U(N) + \Delta t_U(N)$$
$$U(N+1) \equiv L(N+1) + s_4(t_U(N+1) - t_L(N+1)) \tag{2.24}$$

After the beginning and ending extrema are created, EMD can generate upper and lower envelopes and carry out its task normally as seen in Figure 2.6. A similar process can be followed if the first extremum is a minimum or the last extremum is a minimum.

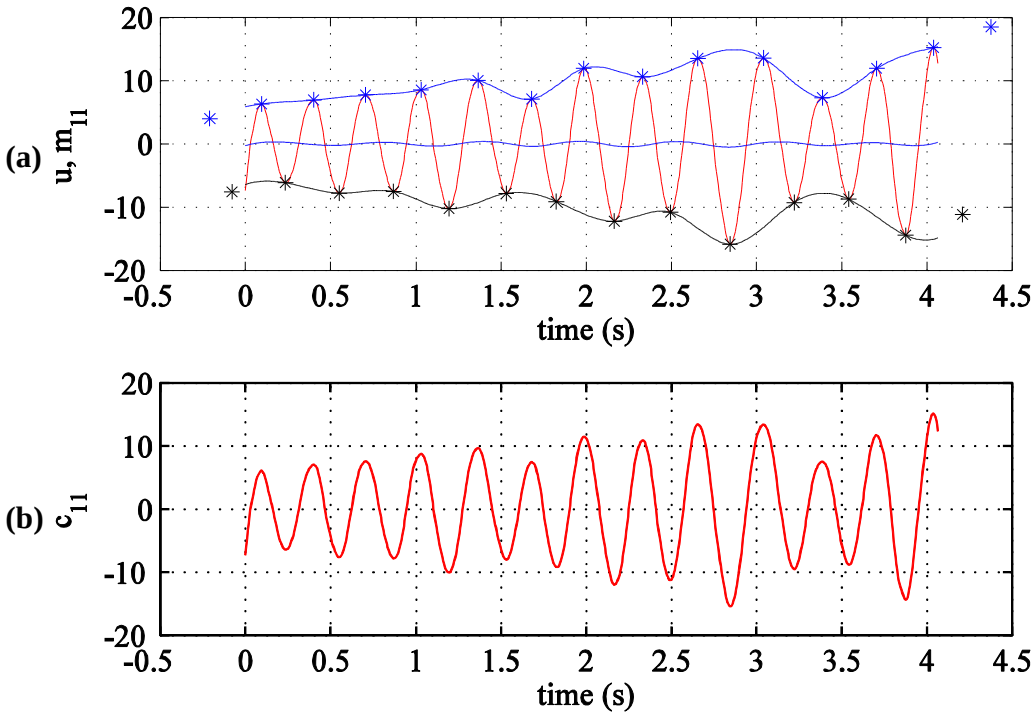

Figure 2.6: Improved EMD procedure with 4 added extrema: (a) $u(t)$ and m_{11} and (b) c_{11}.

While SBM is simple and utilizes the characteristic of the signal itself to generate beginning and ending extrema, it may fail to account for the signal variation at these ending segments. The improved slope-based method (ISBM) offers a simple resolution to this problem by comparing the created extremum with the first and last points of the data [17]. For a random signal $u(t)$, if the first extremum is a maximum, ISBM uses SBM to

generate a beginning minimum $L(0)$. Then it compares $L(0)$ with the ordinate of the first data point $u(1)$. If $L(0) > u(1)$, then it uses $u(1)$ as the first additional minimum; else it keeps $L(0)$ as the first additional minimum. After that, ISBM calculates the first additional maximum $U(0)$ by using SBM. Likewise, if the first extremum is a minimum, then ISBM compares the first generated maximum with the first data point. Whichever greater is chosen as the first additional maximum. The additional minimum will be calculated normally by using SBM. Finally, the same process is done for the ending extrema.

Another method to reduce the end effect of EMD is to increase the processed data length. For convenience, we called this Extended End method (EE). In the Equine Lameness Locator, only part of the collected data, during which the horse trots uniformly, is analyzed. Because the requirement is very strict, some analyzable data points are also omitted. Hence, we increase the selected data length at both ends. When EMD finishes decomposing the extended signal, we confine the segment to its original length and disregard the extended sections. After that, the data can be processed by ELL. Experiment data show that we can extend the selected data by about 200 points (1 second in time length) at each end, as shown in Figure 2.7. If there are not enough 200 points at the beginning or ending segment, we take all the available data points. While this method cannot eliminate all the errors created by EMD at the ending segments, it reduces the error significantly.

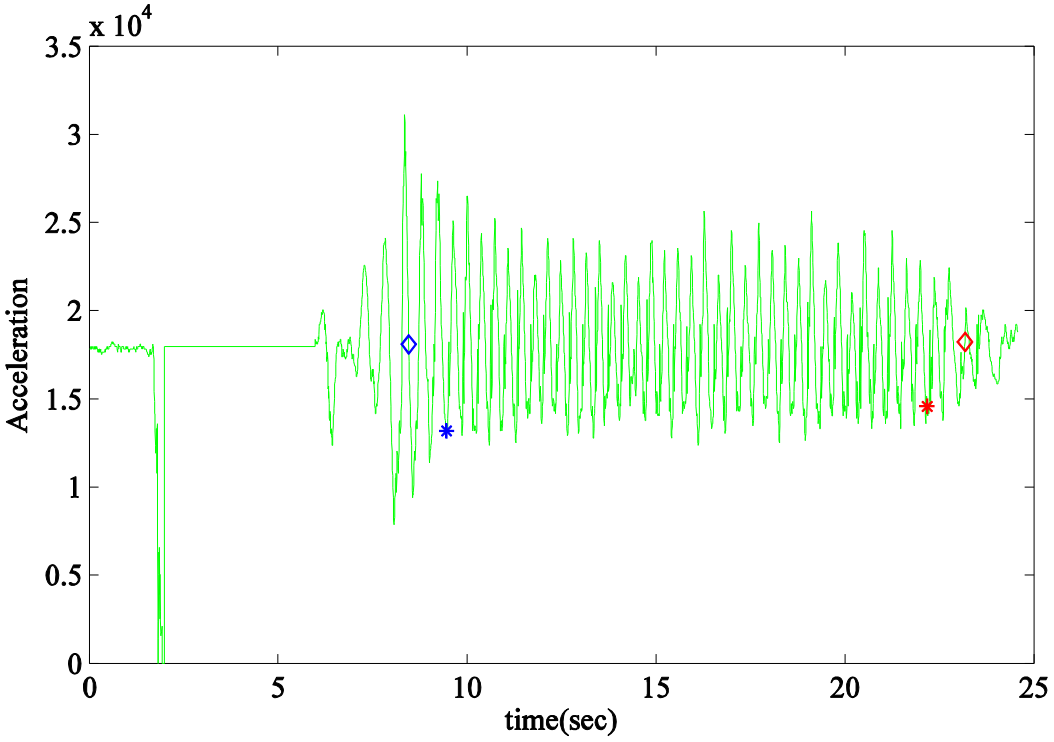

Figure 2.7: Two extended ends for EMD analysis.

2.2.4. Hilbert Transform

Hilbert transform (HT) is the second step of HHT. It calculates the time-varying frequency and amplitude of each IMF or each harmonic component in ELL [9]. First, Hilbert transform is performed to find $d_i(t)$ from each IMF $c_i(t)$ as

$$d_i(t) = HT(c_i(t)) \tag{2.25}$$

Then the instantaneous amplitude and frequency of the IMF are calculated as

$$A_i = \sqrt{c_i^2 + d_i^2} \tag{2.26}$$

$$\omega_i = \dot{\theta}_i,\ \theta_i = \tan^{-1}(\frac{d_i}{c_i}) \tag{2.27}$$

Since Hilbert transform uses Fourier transform [14], it is also not accurate at the two data ends due to the discontinuity between the beginning data point and the ending data point. This is called Gibbs' phenomenon.

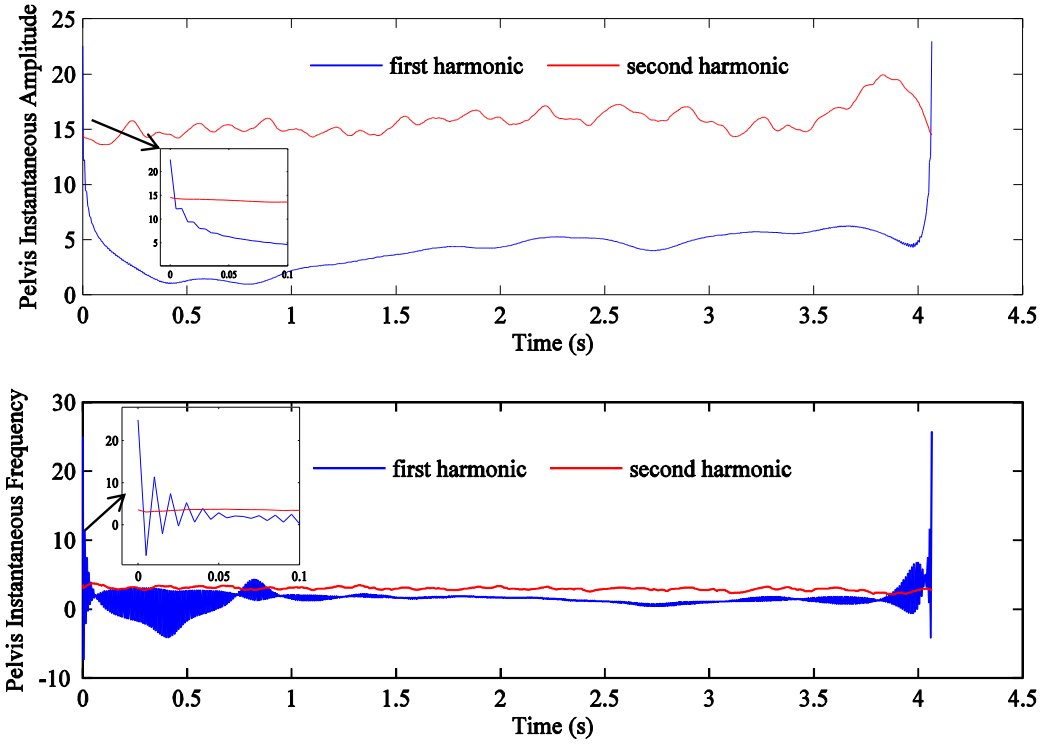

Figure 2.8: Instantaneous frequency and amplitude from HHT analysis.

Figure 2.8 shows results of HHT analysis of a real horse's pelvis motion data. Note that the instantaneous amplitude and frequency at both beginning and ending sections are greatly different from the middle section. On the other hand, CPD is not affected by Gibbs' effect because CPD is based on curve fitting. Therefore, we use CPD, instead of HT, to calculate the instantaneous frequency and amplitude of each IMF at the two data ends. Experimental results show that replacing about ten percent of the signal length at each data end reduces errors significantly. As a result, we replace HT with CPD for

twenty percent of the data length. This hybrid approach is named in this work the HHT-CPD-end method.

2.3. Conjugate-Pair Decomposition Method

Conjugate-pair decomposition improves the SWF method and enables on-line frequency and amplitude tracking of a signal [19]. Similar to SWF, CPD assumes that a signal has a moving average C_0 and p harmonic components with initially estimated/guessed frequencies ω_i in the following form:

$$u(t) = C_0 + \sum_{i=1}^{p} [a_i \cos(\omega_i t + \phi_i)] = C_0 + \sum_{i=1}^{p} [C_i \cos(\omega_i \bar{t}) - D_i \sin(\omega_i \bar{t})] \tag{2.28}$$

where $C_i \equiv a_i \cos(\omega_i t_n + \phi_i)$, $D_i \equiv a_i \sin(\omega_i t_n + \phi_i)$, ω_i is the frequency at previous time step, t_n is the current time instant, and $\bar{t} = (t - t_n)$ is the shifted time. Then C_0, C_i and D_i can be found by minimizing the following squared error *Er*:

$$Er = \sum_{k=-(m-1)/2}^{(m-1)/2} (U_{n+k} - u_{n+k})^2 \tag{2.29}$$

where $m(\geq 1+2p)$ is the total number of processed data points and is assumed to be an odd number here. The instantaneous frequencies and amplitudes of the signal can be calculated as

$$a_i = \sqrt{C_i^2 + D_i^2} \tag{2.30}$$

$$\omega_i = \dot{\theta}_i \approx \frac{\theta_i(t_n) - \theta_i(t_n - q\Delta t)}{q\Delta t} \tag{2.31}$$

where $\theta_i \equiv \omega_i t_n + \phi_i = \tan^{-1}(\frac{D_i}{C_i})$. If a signal is already decomposed into several IMFs by using EMD, CPD can be used to track the instantaneous frequency and amplitude of each IMF $c_i(t)$ by assuming

$$c_i(t) = C_0 + C_1 \cos(\omega_i \bar{t}) - D_1 \sin(\omega_i \bar{t}) \tag{2.32}$$

The reason is that the frequency of an IMF varies within a very narrow frequency band. Moreover, $C_0 = 0$ can be assumed because the moving average of each IMF is zeroed by the EMD process. To start amplitude and frequency tracking using CPD, the starting initial guess of ω_i can be calculated using the Teager-Kaiser algorithm (TKA) [20]. However, for our applications, since on-line frequency and amplitude tracking is not needed, we use the starting frequency computed from HHT.

Because CPD is based on curve fitting, it is not affected by the discontinuity of the two data ends and provides much better estimations of instantaneous frequencies and amplitudes for the ending segments than HHT. Besides, CPD is an adaptive method that can update the initial guess of frequency by using Eq. (2.31), the accuracy of the instantaneous frequency can be improved by running several iterations on Eq. (2.31).

However, CPD is very sensitive to dense data and cannot provide good estimation with horse data collecting at a high sampling frequency (e.g., 200 Hz). CPD can provide accurate time-frequency analysis only if the *m* data points used in Eq. (2.29) can cover at least one quarter of the signal's period [19]. As a result, we have to down sample around two data ends to make it suitable for the proposed HHT-CPD-end method. For this

application, we calculate instantaneous amplitude and frequency of each data instant by skipping points. We specifically use a step of 6 data points in our analysis.

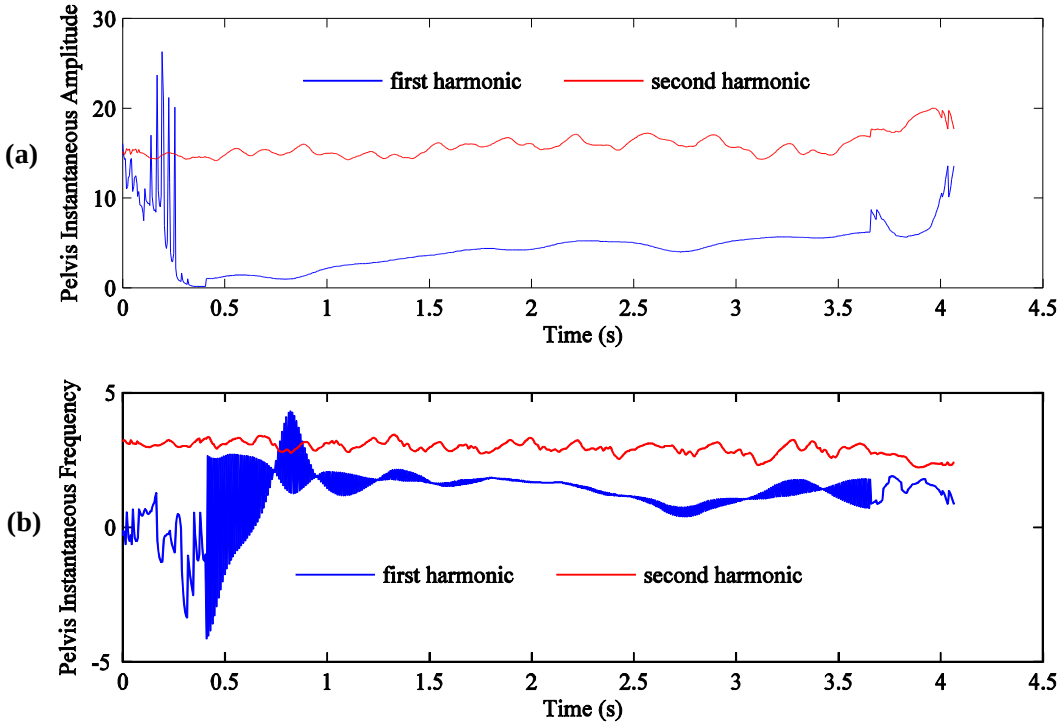

Figure 2.9: Results from HHT-CPD-end analysis: (a) instantaneous amplitude, and (b) instantaneous frequency.

Figure 2.9 shows results from HHT-CPD-end analysis of the same data processed and shown in Figure 2.8. We can see that the instantaneous frequency and amplitude at the ending segments are much more reasonable than those in Figure 2.8 from HHT analysis.

2.4. The New Program

The new Equine Lameness Locator ® (ELL) program is organized exactly the same as the old one, except we replace the SWF with the hybrid HHT-CPD-end method, as shown in Figure 2.10. Next we perform comprehensive numerical simulations and signal

processing of experimental data to compare the accuracy and efficiency of the old SWF method and the new HHT-CPD-end method.

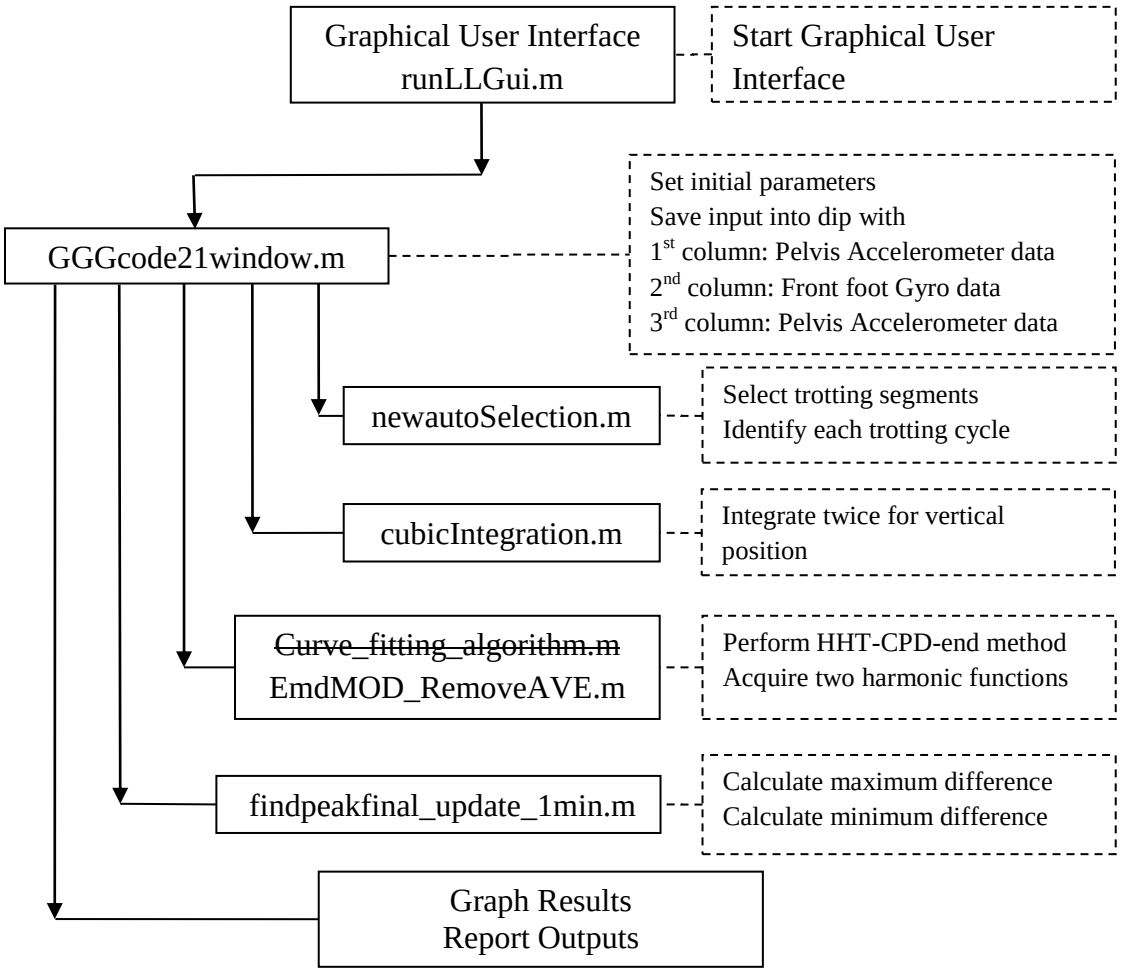

Figure 2.10: The new ELL program using the HHT-CPD-end method.

2.5. Numerical Analysis and Results

The HHT-CPD-end method is evaluated by comparing it with the SWF method using the Lameness Locator ® program. After numerical studies, the more accurate and efficient method will be proposed for use in the next version of ELL. For the purpose of comparison, the main variables that will be compared are the mean of DiffMax, the mean

of DiffMin, the standard deviation of DiffMax, and the standard deviation of DiffMin. The means of DiffMax and DiffMin need to be accurate because they characterize the type and severity of lameness. On the other hand, the standard deviations of DiffMax and DiffMin show the precision of the calculation. To accomplish this goal, we run the ELL programs for two sets of data: a set of artificial ideal data and a set of actual horse data.

Ten ideal data sets were created based on the common frequency and amplitude of head/pelvis vertical displacement observed in live horses. The normal component is assumed to be a harmonic with an amplitude of 10 mm and a frequency of 4 Hz as

$$Z_N = 10\cos(8\pi t) \tag{2.33}$$

The lameness component is assumed to be a harmonic with an amplitude of 5 mm, a frequency of 2 Hz, and a phase angle φ with respect to $Z_n(t)$ as

$$Z_L = 5\sin(4\pi t + \varphi) \tag{2.34}$$

Hence, the total head/pelvis vertical movement is:

$$Z = Z_N + Z_L = 10\cos(8\pi t) + 5\sin(4\pi t + \varphi) \tag{2.35}$$

and the vertical acceleration becomes

$$\ddot{Z} = \ddot{Z}_N + \ddot{Z}_L = -640\pi^2\cos(8\pi t) - 80\pi^2\sin(4\pi t + \varphi) \tag{2.36}$$

Then, random noise is added to the acceleration signals. The noise is a normal distribution vector with a zero mean and a standard deviation of $4\pi^2$. The gyro signal assumed to be measured from the right front limb is just a simple harmonic signal with an average frequency of 1.5 Hz. Finally, the amplitudes of acceleration and gyro signal are

converted to voltage values for the Lameness Locator program. For this analysis, because the signals are assumed ideal data, we only need to try the improved slope-based method (ISBM) for improving EMD and do not evaluate the Extended End method (EE). For convenience, the HHT-CPD-end method referred in this ideal analysis is the HHT-CPD-end with the improvement of ISBM.

Tables 2.1 and 2.2 give the exact values of the main variables and the calculated values using both HHT-CPD-end and SWF. The results show that the mean values from HHT-CPD-end are mostly closer to the exact values, and the standard deviation values are slightly smaller than those from SWF. In other words, the Lameness Locator with HHT-CPD-end gives slightly more accurate and precise values for both DiffMax and DiffMin for most of the cases. However, this improvement is not significant. Also, for a few cases where the DiffMax or DiffMin are very small or close to zero, HHT-CPD-end overestimates the variables. Hence, the implement of HHT-CPD-end into ELL may not be necessary.

Table 2.1: Analysis of ideal head acceleration data.

		Mean DiffMax Head (mm)					SD DiffMax Head (mm)			Mean DiffMin Head (mm)					SD DiffMin Head (mm)		
Case	Phase Difference (rad)	Exact	SWF Method	Percent Error	HHT-CPD-end Method	Percent Error	SWF Method	HHT-CPD-end Method	Percent Difference	Exact	SWF Method	Percent Error	HHT-CPD-end Method	Percent Error	SWF Method	HHT-CPD-end Method	Percent Difference
1	$\pi/2$	10.00	9.33	6.68%	9.42	5.82%	0.10	0.08	17.17%	0.00	0.00	NA	0.00	NA	0.10	0.07	27.55%
2	π	0.00	0.01	NA	0.01	NA	0.10	0.07	27.55%	-10.00	-9.32	6.76%	-9.41	5.88%	0.11	0.07	32.11%
3	$3\pi/2$	-10.00	-9.33	6.72%	-9.42	5.84%	0.11	0.09	16.36%	0.00	-0.01	NA	-0.01	NA	0.10	0.08	23.47%
4	$\pi/4$	7.05	6.55	7.12%	6.61	6.28%	0.13	0.09	27.78%	7.05	6.56	7.01%	6.62	6.16%	0.10	0.08	15.79%
5	$5\pi/4$	-7.05	-6.55	7.15%	-6.61	6.30%	0.12	0.09	24.17%	-7.05	-6.54	7.25%	-6.60	6.38%	0.12	0.10	17.36%
6	$\pi/5$	5.83	5.40	7.36%	5.47	6.26%	0.13	0.11	19.85%	8.07	7.50	7.16%	7.60	5.90%	0.12	0.10	17.07%
7	$3\pi/5$	9.49	8.85	6.73%	8.93	5.88%	0.09	0.08	17.02%	-3.07	-2.86	6.78%	-2.91	4.96%	0.12	0.10	14.17%
8	$6\pi/5$	-5.83	-5.42	7.06%	-5.49	5.95%	0.10	0.08	20.00%	-8.07	-7.50	7.15%	-7.60	5.87%	0.11	0.09	18.58%
9	$8\pi/5$	-9.49	-8.85	6.75%	-8.93	5.89%	0.11	0.09	20.18%	3.07	2.86	6.78%	2.91	5.02%	0.12	0.11	13.22%
10	$\pi/6$	4.96	4.59	7.40%	4.66	5.99%	0.13	0.09	30.53%	8.64	8.05	6.83%	8.15	5.73%	0.11	0.08	26.79%

Table 2.2: Analysis of ideal pelvis acceleration data.

		Mean DiffMax Pelvis (mm)					SD DiffMax Pelvis (mm)			Mean DiffMin Pelvis (mm)					SD DiffMin Pelvis (mm)		
Case	Phase Difference (rad)	Exact	SWF Method	Percent Error	HHT-CPD-end Method	Percent Error	SWF Method	HHT-CPD-end Method	Percent Difference	Exact	SWF Method	Percent Error	HHT-CPD-end Method	Percent Error	SWF Method	HHT-CPD-end Method	Percent Difference
1	$\pi/3$	-8.64	-8.05	6.86%	-8.14	5.77%	0.12	0.09	22.69%	-4.96	-4.61	NA	-4.68	NA	0.12	0.10	17.80%
2	$2\pi/3$	-8.64	-8.04	NA	-8.13	NA	0.11	0.09	18.42%	4.96	4.62	6.91%	4.69	5.52%	0.11	0.09	17.27%
3	$4\pi/3$	8.64	8.05	6.91%	8.14	5.82%	0.12	0.09	26.27%	4.96	4.62	NA	4.69	NA	0.13	0.10	25.38%
4	$3\pi/4$	-7.05	-6.55	7.16%	-6.60	6.34%	0.10	0.09	18.27%	7.05	6.57	6.82%	6.63	5.97%	0.12	0.10	18.03%
5	$7\pi/4$	7.05	6.54	7.19%	6.60	6.34%	0.13	0.10	25.00%	-7.05	-6.55	7.16%	-6.60	6.45%	0.16	0.10	41.36%
6	$2\pi/5$	-9.49	-8.83	6.96%	-8.91	6.13%	0.12	0.10	15.38%	-3.07	-2.88	6.16%	-2.93	4.37%	0.12	0.11	3.48%
7	$4\pi/5$	-5.83	-5.41	7.30%	-5.47	6.19%	0.13	0.10	20.47%	8.07	7.53	6.79%	7.63	5.54%	0.12	0.09	22.61%
8	$7\pi/5$	9.49	8.85	6.72%	8.93	5.89%	0.12	0.08	36.67%	3.07	2.84	7.34%	2.90	5.41%	0.13	0.09	30.23%
9	$9\pi/5$	5.83	5.39	7.51%	5.46	6.38%	0.10	0.09	14.42%	-8.07	-7.53	6.70%	-7.62	5.57%	0.18	0.10	44.63%
10	$5\pi/6$	-4.96	-4.63	6.67%	-4.70	5.26%	0.12	0.10	16.67%	8.64	8.05	6.86%	8.15	5.74%	0.14	0.11	19.12%

Next, we process 158 sets of signals measured from live horses using SWF and HHT-CPD-end (referred as HHT from here on), respectively. Among those data sets, the ELL with HHT plus EE improvement cannot process 38 data sets, HHT plus ISBM improvement cannot process 29 data sets, but SWF can process all data sets. This is because the HHT fails to decompose those signals into 2 harmonic components. Hence, ELL cannot detect enough DiffMax and DiffMin. On the other hand, both improved HHT methods output some extreme values for standard deviations. Figure 2.11 plots 120 DiffMax standard deviations from ELL analysis using the HHT with EE improvement against those using the SWF method. One can see that HHT with EE improvement gives more than 10 standard deviations that are above 100, significantly larger than those from SWF. The extreme values of the HHT with ISBM improvement are even worse.

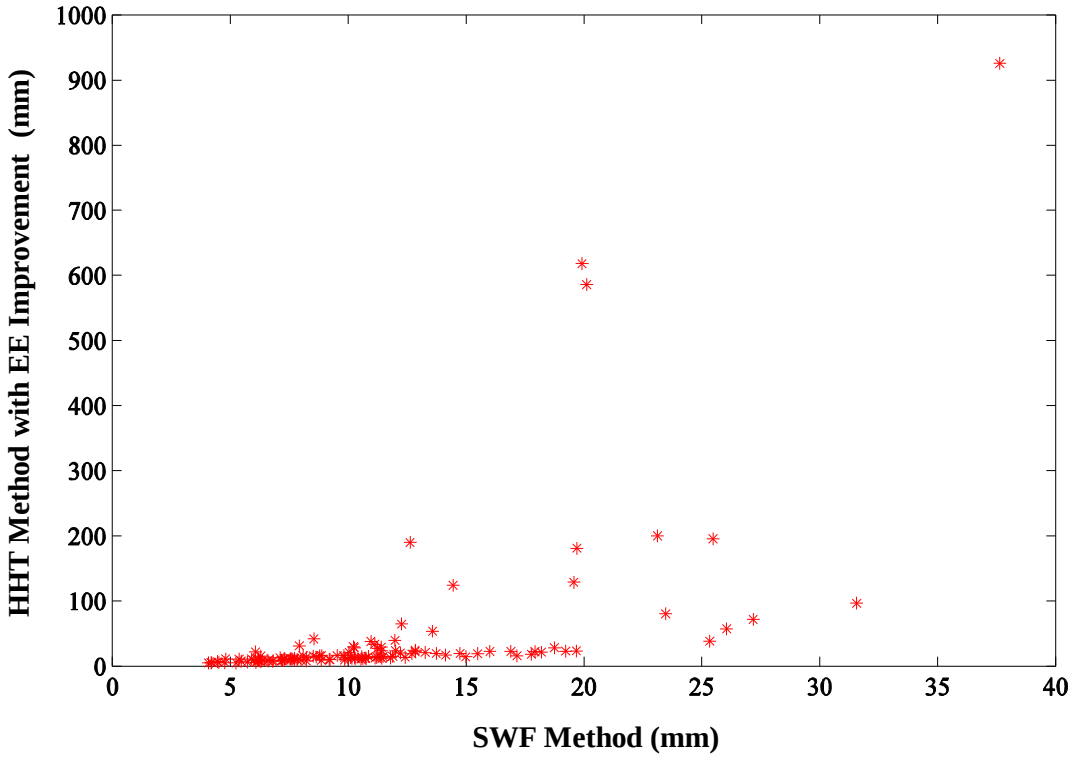

Figure 2.11: Standard deviations of DiffMax from the HHT with EE improvement and the SWF.

After eliminating these extreme values, we plot the standard deviation of DiffMax from one method against another along with a straight line $y = x$. Figure 2.12 plots 108 pairs of DiffMax standard deviations from the HHT with EE improvement and the SWF methods. On the other hand, Figure 2.13 plots 107 pairs of DiffMax standard deviations from the HHT with ISBM improvement and the SWF method. Both Figures 2.12 and 2.13 show that most of the points are above the line, which indicates that the standard deviations from both HHT-CPD-end methods are mostly larger than those from the SWF method. The actual values plotted in Figures 2.12 and 2.13 are also reported in Tables A.1 and A.3 of appendix A.

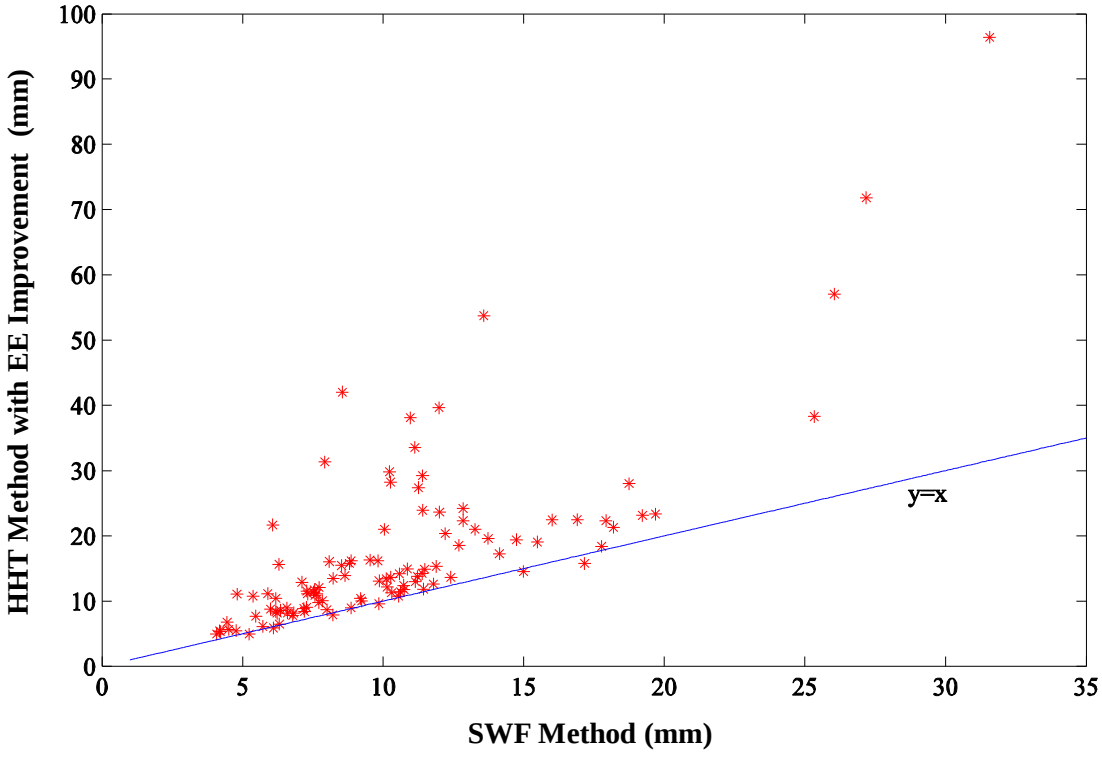

Figure 2.12: Standard deviations of DiffMax from the HHT with EE improvement and the SWF.

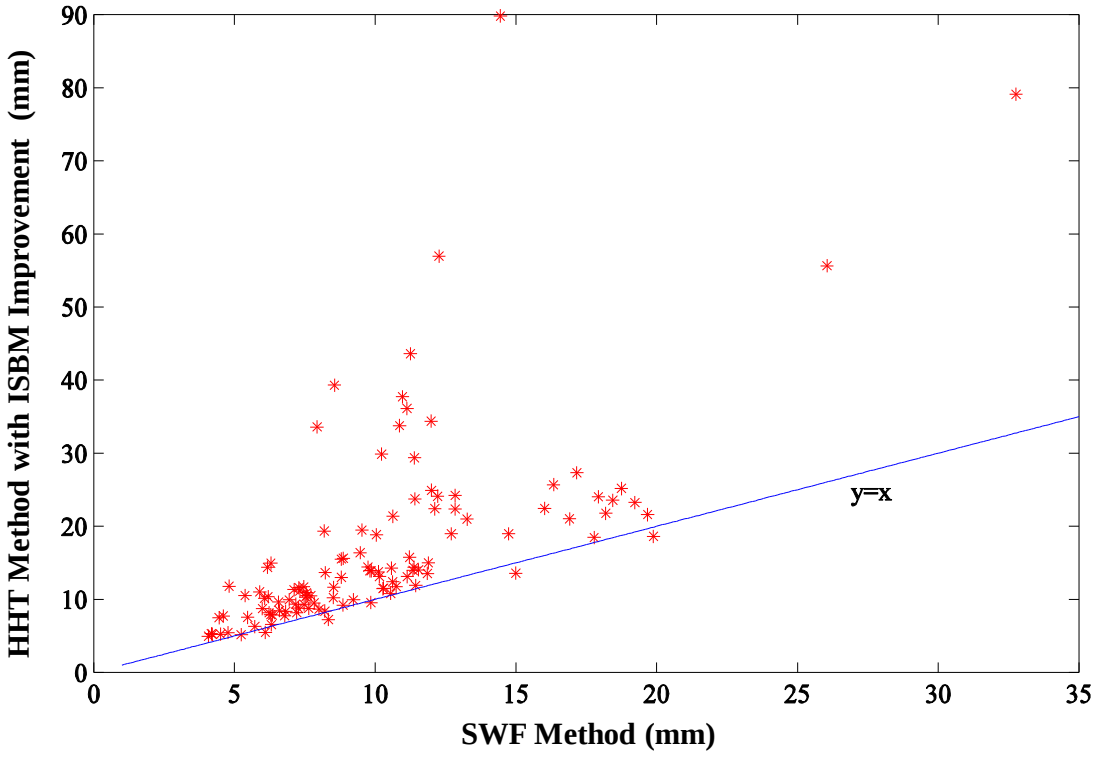

Figure 2.13: Standard deviations of DiffMax from the HHT with ISBM improvement and the SWF.

Clearly, for live horse data, the SWF method is more robust and accurate than the HHT with EE improvement and the HHT with ISBM improvement. We believe that robustness and precision are very important in analyzing lameness in horses. Also, ideal data test shows that HHT is not much more accurate than SWF. Hence, we decided not to implement HHT into the Lameness Locator program ®. However, HHT gives the instantaneous frequency of each harmonic component, which may be helpful for analyzing other gaits such as canter or gallop. Further research is needed to explore this potential of HHT and CPD methods.

Chapter 3: NUMERICAL INTEGRATION AND DIFFERENTIATION AND GYRO SIGNAL FABRICATION

Because the current ELL processes accelerations measured by wireless accelerometers to obtain displacements before lameness evaluation analysis, methods for numerical integration are needed. Also, because the measurement accuracy of wireless accelerometers will be calibrated against the displacements measured by a camera-based motion analysis system, numerical differentiation methods are also needed. This chapter is to present and evaluate methods for numerical integration and differentiation. Furthermore, we will present a method for creating (without actually measuring) the right foot angular velocity from the vertical accelerations of the head and pelvis (see Figure 1.6) to be used for determining the right and left stance phases.

3.1. Numerical Integration Method

We use the trapezoidal rule to perform numerical integrations. Given the acceleration values at consecutive time instants, Figure 3.1 shows that the velocity at time t_i is approximated by the trapezoidal rule as

$$v(t_i) = v(t_{i-1}) + \frac{a(t_{i-1}) + a(t_i)}{2}(t_i - t_{i-1}) = v(t_{i-1}) + \frac{a(t_{i-1}) + a(t_i)}{2}\Delta t \qquad (3.1)$$

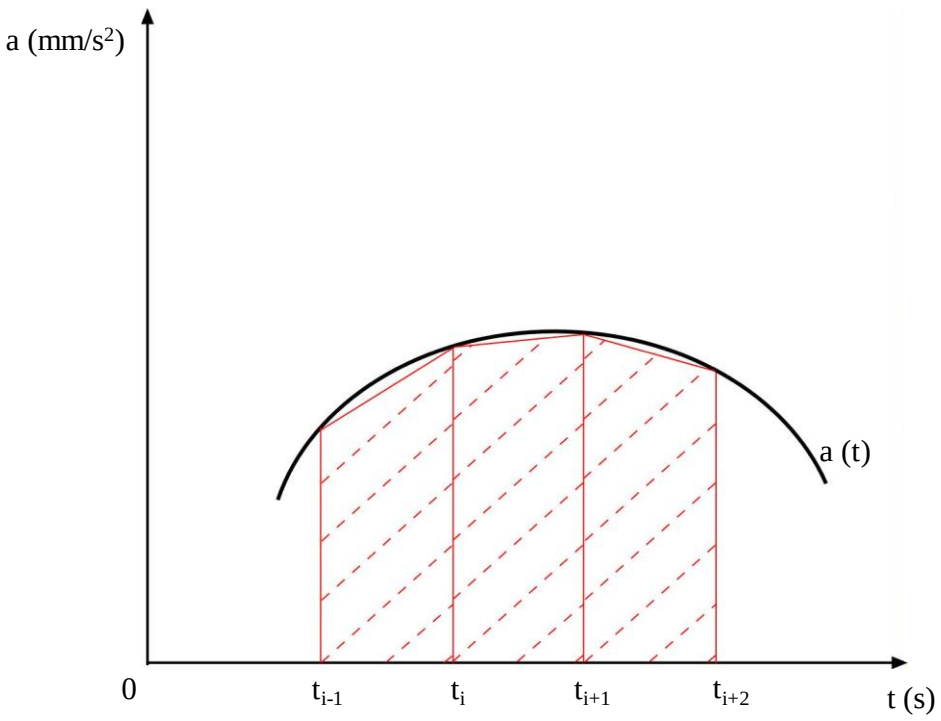

Figure 3.1: The trapezoidal rule for numerical integration.

While the trapezoidal rule is accurate only if a small Δt is used, it is appropriate for our application here because a relatively high sampling frequency is used and a horse's head and pelvis vertical motion frequency is just a few cycles per second. As shown later in Section 3.3, for a sampling frequency of 200 Hz and signals consisting of 2Hz and 4Hz harmonics, even results from double integration are quite reasonable. For real horses' data, we assume that the vertical positions, vertical velocities and angular signals of head and pelvis have zero means.

3.2. Numerical Differentiation Method

To obtain better time derivatives of discrete experimental data, this work uses a curve-fitting differentiation method. For a point at $t = t_k$ of a signal $P(t)$, we fit a second-order polynomial $p(t)$ over itself and four neighboring points as

$$p(\bar{t}) = c_1 + c_2\bar{t} + c_3\bar{t}^2 \tag{3.2}$$

where $\bar{t} \equiv t - t_k$. For the first beginning point, we use four points right after it. For the second beginning point, we use one point before it and three points right after it. For a middle section point, we use two points before it and two points after it. Similarly, for the last point, we use four points before it. The three constants c_1, c_2 and c_3 are obtained by least-squares fitting. The first and second derivatives of $p(\bar{t})$ are

$$\dot{p}(\bar{t}) = c_2 + 2c_3\bar{t} \tag{3.3}$$

$$\ddot{p}(\bar{t}) = 2c_3 \tag{3.4}$$

At $\bar{t} = 0$ (i.e., $t = t_k$), we have $\dot{p}(0) = c_2 = \dot{P}(t)$. Hence, the first and second derivatives at each point t of the signal $P(t)$ are c_2 and $2c_3$. However, results from the accelerometer-videogrammetry test presented later in Section 4.3 show that the acceleration from this method contains a considerable amount of noise. Figure 3.2 compares the numerical acceleration obtained by using Eq. (3.4) on the camera-measured position signal (see Figure 1.2) with the acceleration signal directly measured by an accelerometer (see Figure 1.6).

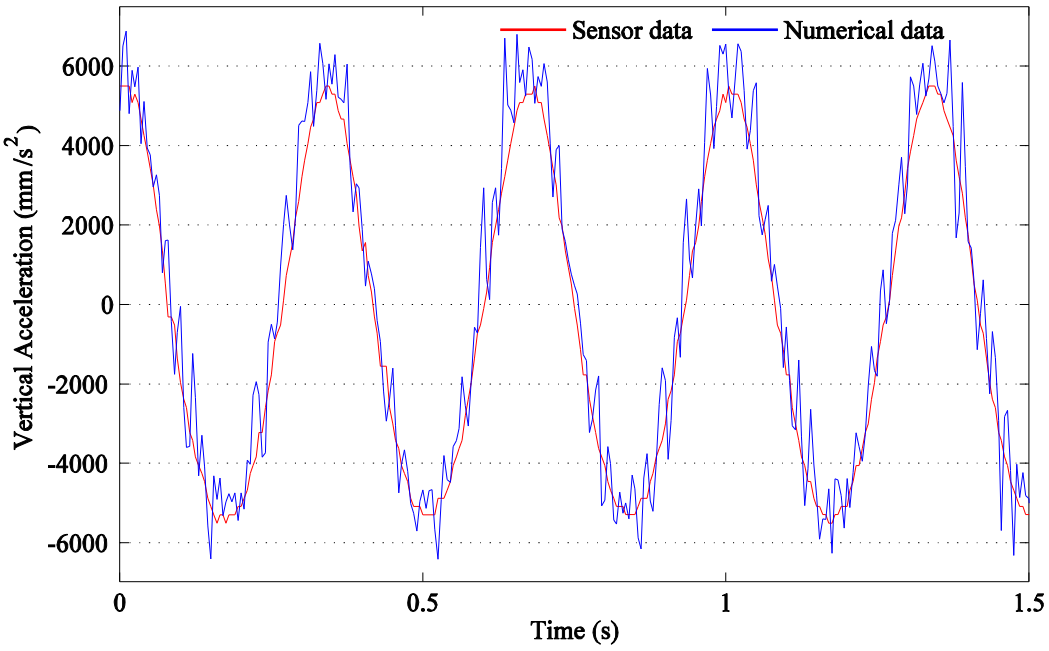

Figure 3.2: Directly measured acceleration and acceleration from single curve fitting.

It can be seen from Figure 3.2 that the sensor-recorded acceleration signal is quite smooth while the acceleration from single curve fitting is very noisy. To reduce this problem, we perform the same polynomial fitting on the obtained $\dot{P}(t)$ and then take its first derivative to obtain $\ddot{P}(t)$. Figure 3.3 compares the so-obtained acceleration signal from double curve fitting with the sensor-recorded acceleration signal. Figures 3.2 and 3.3 show that the double curve fitting significantly reduces the numerical noise.

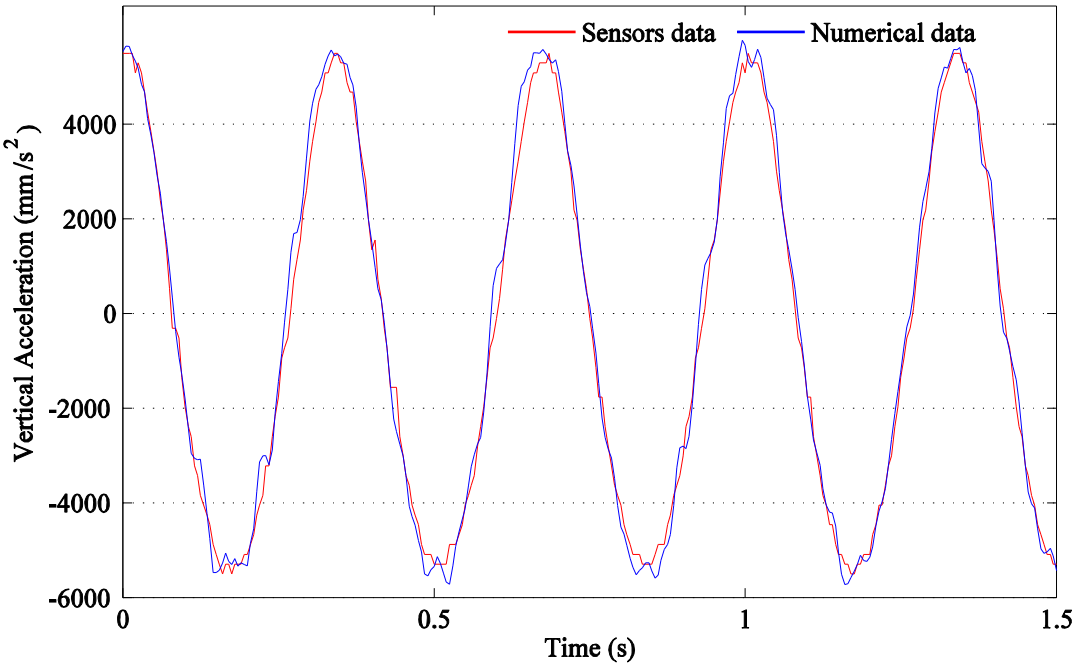

Figure 3.3: Directly measured acceleration and acceleration from double curve fitting.

It can be seen from Figure 3.3 that the numerical acceleration matches the sensor acceleration very well. Also, numerical results shown next in Section 3.3 indicate that this double differentiation technique is good enough for our application.

3.3. Numerical Integration and Differentiation Results

To check the accuracy of the numerical differentiation and integration methods for our application, we consider the following ideal position signal

$$u(t) = -10\cos(4\times 2\pi t) - 5\sin(2\times 2\pi t + \pi/2) \quad (mm) \tag{3.5}$$

Then, the ideal acceleration signal is

$$\ddot{u}(t) = 10(4\times 2\pi)^2 \cos(4\times 2\pi t) + 5(2\times 2\pi)^2 \sin(2\times 2\pi t + \pi/2) \ (mm/s^2) \tag{3.6}$$

These two signals have amplitudes and frequencies similar to those observed in real horses. Also, we sample these two signals at 200 Hz for numerical analysis. First, we obtain acceleration from the ideal position signal by using the double curve fitting approach. Comparing this numerical signal with the ideal acceleration, we found that the two signals are almost the same. The maximum absolute error for this curve-fitting differentiation process is only 216 mm/s^2, resulting in only about 1.5% relative error. Hence, we conclude that the double curve-fitting differentiation method is appropriate for our purpose. Figure 3.4 demonstrates that the differentiated acceleration almost overlaps with the ideal signal.

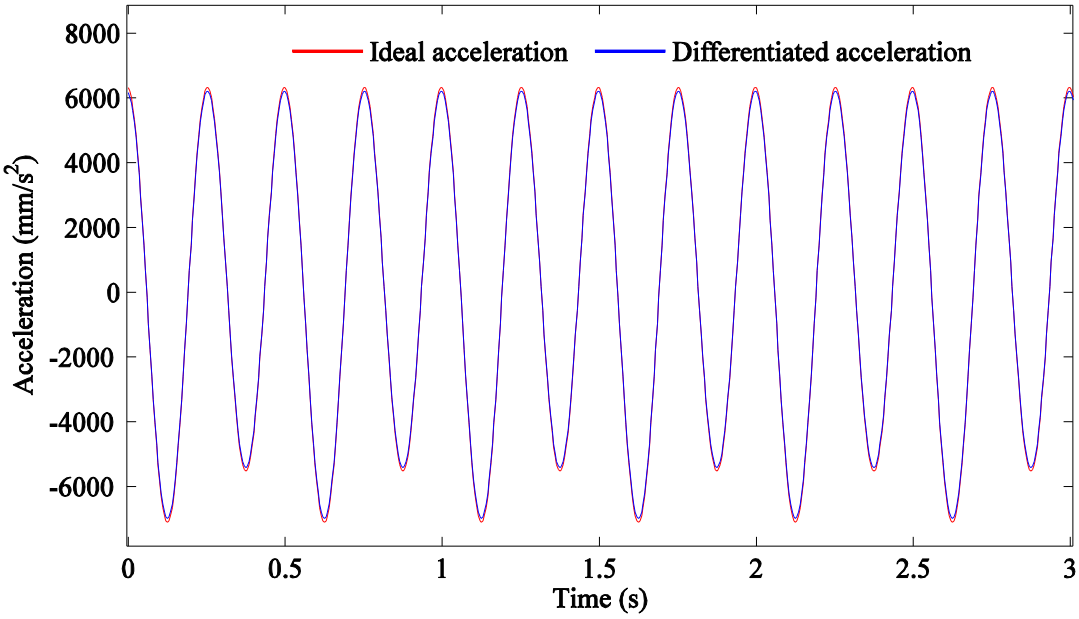

Figure 3.4: Acceleration from double curve fitting and the ideal acceleration.

Next, we obtain the numerical position by double integrating the acceleration obtained from double curve fitting. Again, numerical study shows that the numerical position signal is almost the same as the ideal position signal, as shown in Figure 3.5.

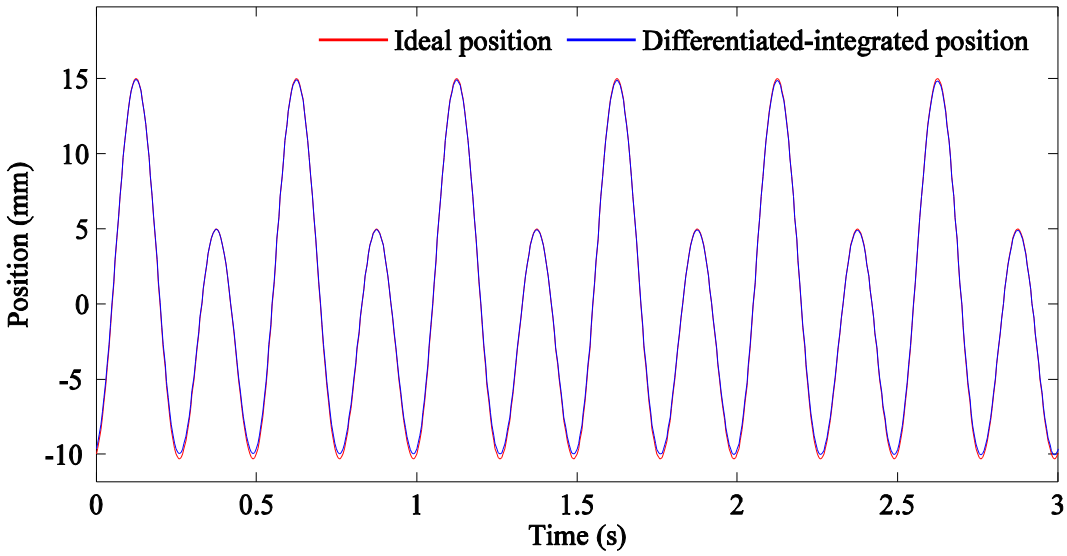

Figure 3.5: The differentiated-integrated position and the ideal position.

The maximum absolute error between the differentiated-integrated position signal and the ideal position signal is only 0.373 mm, resulting in only about 1.5% error. We can see that although we do both double differentiation and double integration, the final position signal is still very close to the ideal one. Most certainly, the curve fitting differentiation and the numerical integration are good enough for our application. However, we also want to check if these numerical processes can work with experimental data.

As shown later in Section 4.3, the vertical position signals measured by the camera system in the accelerometer-videogrammetry test are very accurate. Using the proposed double curve fitting method on these position signals, we obtain numerical acceleration signals. Then we obtain the numerical position signals by numerically integrating these acceleration signals twice using the trapezoidal rule. Comparing this numerical position signal with the camera-measured position signal, we find that the relative error is also

very small, only about 1%. The numerical position and the camera-measured position from one typical trial are plotted in Figure 3.6.

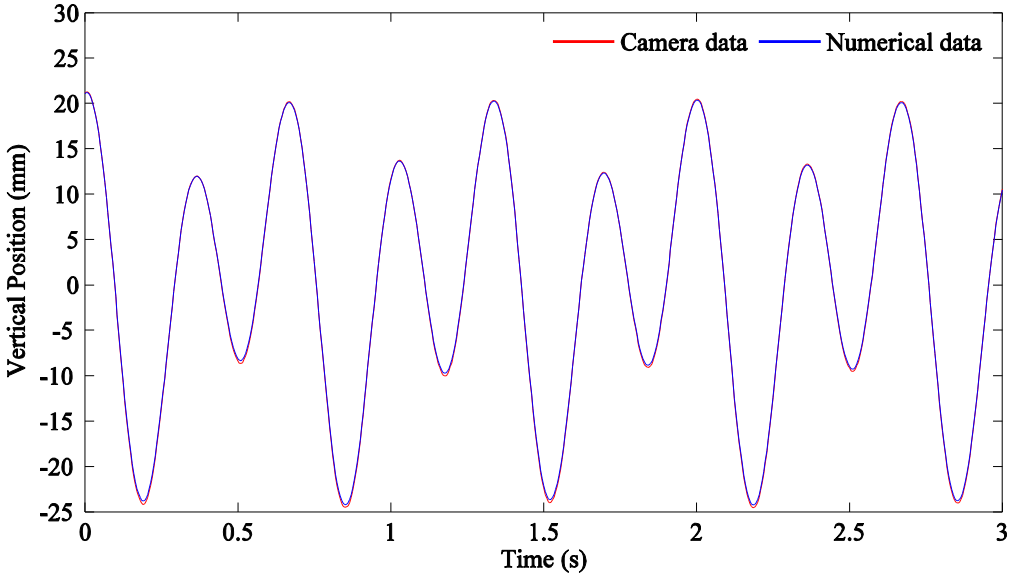

Figure 3.6: The differentiated-integrated numerical position and the camera-measured position from the accelerometer-videogrammetry test.

While these numerical methods work great for low frequencies (2 – 4 Hz) and a sampling rate at 200 Hz, they are not accurate for signals of higher frequencies (e.g., 8 Hz) sampled at the same sampling rate. To show this we consider the following ideal one-harmonic position signal

$$u(t) = -10\cos(8\times 2\pi t)\ (mm) \tag{3.7}$$

The corresponding ideal acceleration signal is

$$\ddot{u}(t) = 10(8\times 2\pi)^2\cos(8\times 2\pi t)\ \ (mm/s^2) \tag{3.8}$$

We obtain the numerical acceleration from Eq. (3.7) using the proposed double curve fitting. Figure 3.7 shows that the numerical acceleration is not very accurate, and the maximum relative error is about 5%.

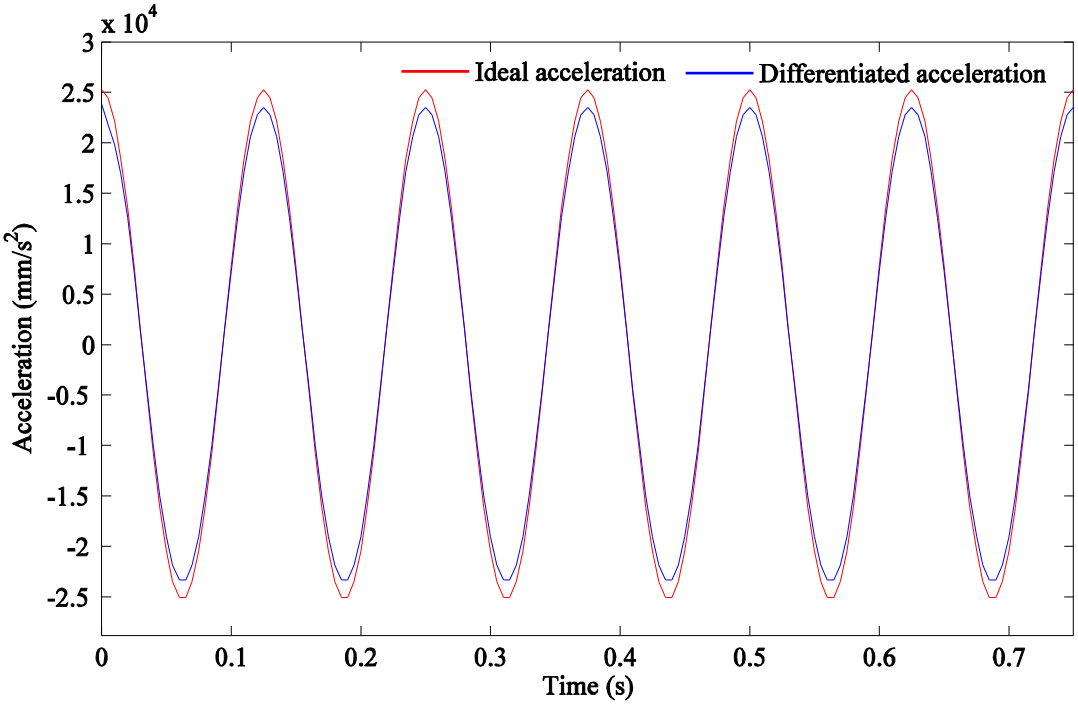

Figure 3.7: Acceleration from double curve fitting and the ideal acceleration of an 8-Hz harmonic.

On the other hand, numerical integration proves to be quite accurate for signals of higher frequencies. Numerical results show that, if the sampling rate is kept at 200 Hz, numerical integration starts to result in significant errors only when the signal's frequency is higher than 32 Hz. To show this we consider the following ideal one-harmonic position signal

$$u(t) = -10\cos(32\times 2\pi t)\ (mm) \tag{3.9}$$

The corresponding ideal acceleration signal is

$$\ddot{u}(t) = 10(32 \times 2\pi)^2 \cos(32 \times 2\pi t) \ (mm/s^2) \tag{3.10}$$

Numerically integrating the ideal acceleration signal twice, we obtain the numerical position signal shown in Figure 3.8. It shows that the integrated position signal is not accurate because the ideal acceleration signal is not sampled at enough points to present a smooth sinusoidal wave.

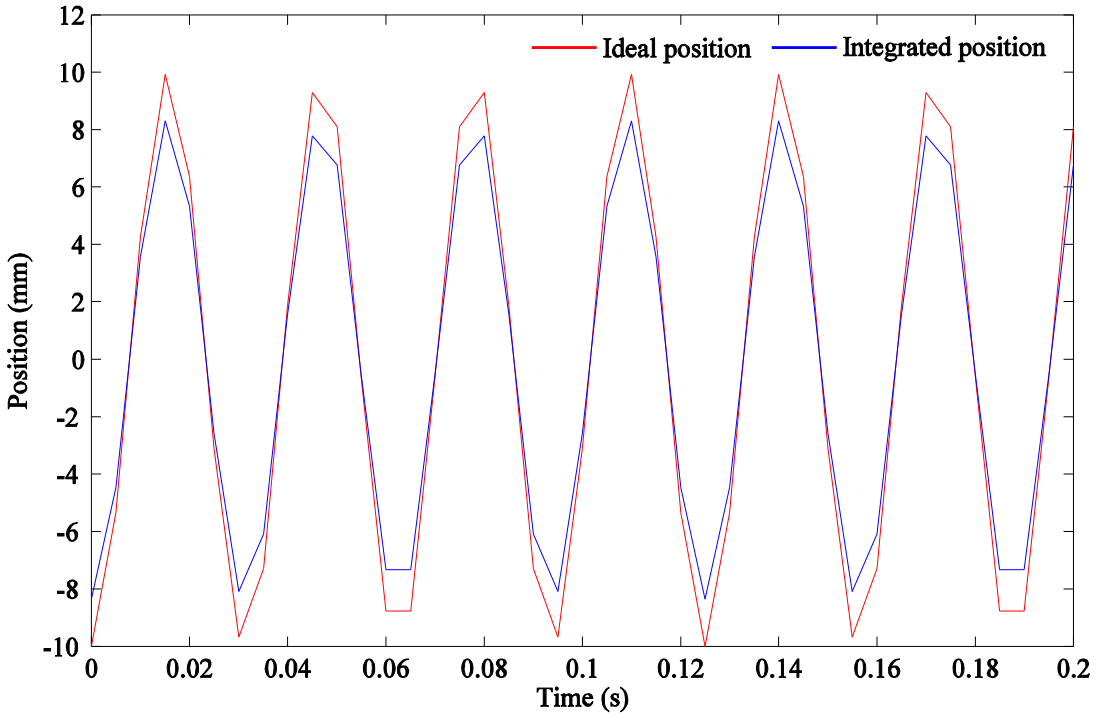

Figure 3.8: The position from double integrations and the sampled curve of a 32-Hz harmonic.

As a result, we believe that high frequency noise not only may affect the measured values of sensors but also can reduce the accuracy of numerical analysis. Hence, we recommend noise filtering before integration in the ELL analysis.

3.4. Fabrication of Right Foot Gyroscope Signal for ELL

The current ELL uses a gyroscope to measure the right foot angular rate of a trotting horse. This signal is important for determining the analyzable data segments as well as for identifying the right and left stance phases as mentioned in Chapter 1. Without this signal, the experiments simulated later in Chapter 4 cannot evaluate horse lameness with only two acceleration signals generated from these experiments.

This section present a method to create a gyroscope signal based on a simulated acceleration signal. We generate the gyroscope signal based on two criteria. First, the gyroscope signal has a frequency quite similar to that of the lameness component (1.5 – 2 Hz), which is one half of the normal component. Second, the gyroscope signal should be consistent with the acceleration signal. That means the acceleration signal from an experiment trial has a corresponding unique gyroscope signal that reflects how their frequency and amplitude change over time. Hence, the best way to fabricate the gyroscope signal is to create a cubic spline curve based on the acceleration signal itself. First, we smooth the acceleration signal $a(t)$. Then we find the local maxima of $a(t)$ as shown in Figure 3.9.

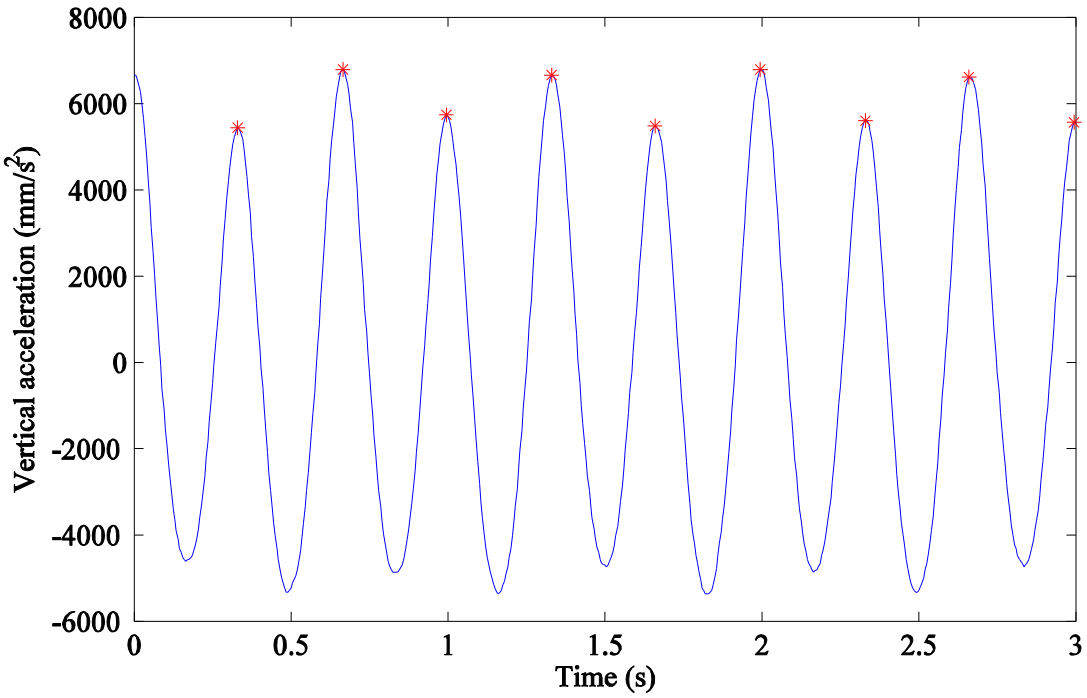

Figure 3.9: Finding the local maxima of $a(t)$.

After that, we multiply -1 with every other maximum value as depicted in Figure 3.10.

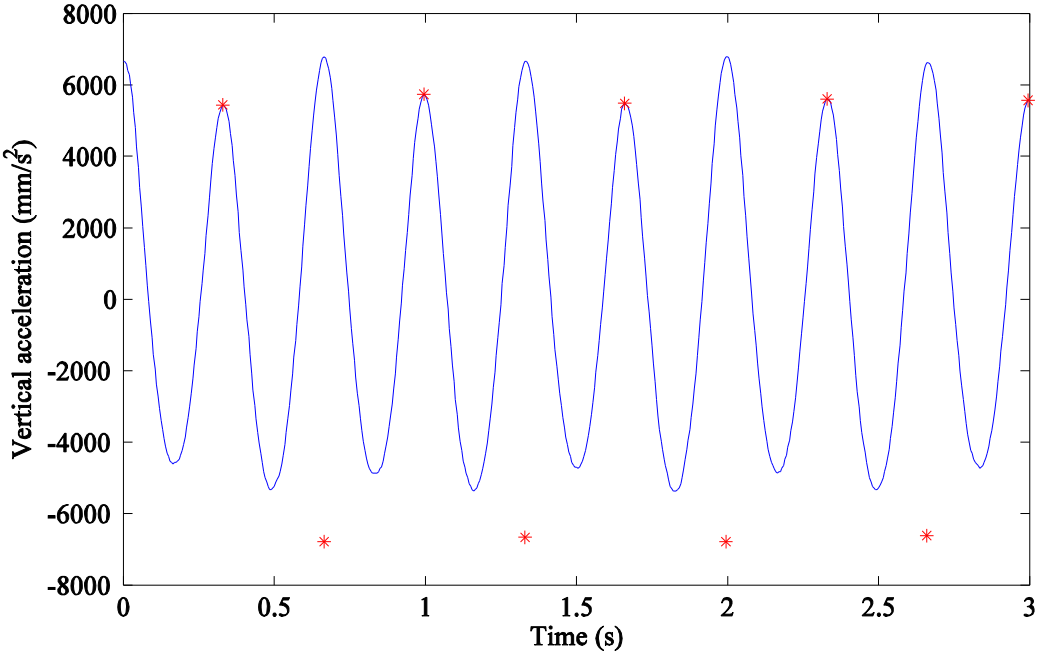

Figure 3.10: Every other maximum value is multiplied by -1.

Finally, we fit a cubic spline curve over all the points to get the gyroscope signal that satisfies the two requirements mentioned above. The gyroscope signal is shown in Figure 3.11. Notice that we can increase or decrease the amplitude of the gyroscope signal such that we can visualize it better in the ELL graphs just by multiplying the signal with a constant factor.

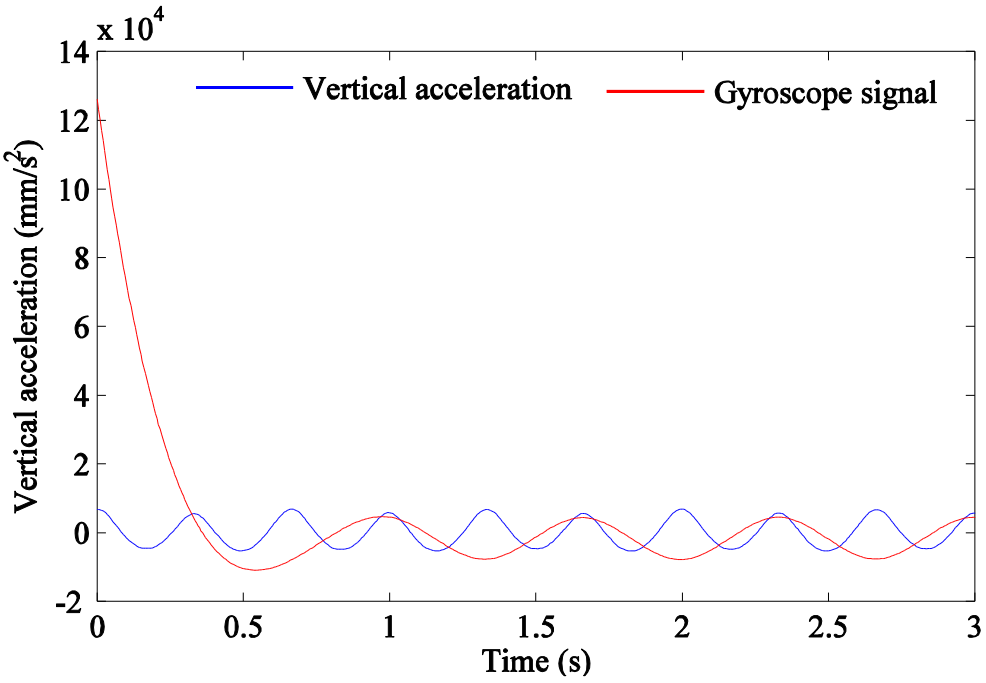

Figure 3.11: The created gyroscope signal and the original acceleration signal.

We can also see that the beginning of the gyroscope signal is not consistent with the rest of the signal because of the inherent properties of the cubic spline curve. This is also true for the ending segment of the gyroscope signal that is not shown here. As a result, these beginning and ending acceleration segments will not be analyzed in the ELL program. However, this is not a problem because the beginning and ending segments are usually very short comparing to the overall length of the signal.

Chapter 4: SENSORS CONDITIONING AND NUMERICAL RESULTS

The Equine Lameness Locator ® (ELL) software assumes that the two accelerometers (see Figure 4.1) always provide the true vertical accelerations. However, the sensors do not really measure the true vertical accelerations because of three reasons. First, each sensor can only measure the acceleration in the direction perpendicular to its top surface. Unfortunately, a horse's head and pelvis continuously rotate during a trot along the directions shown in Figure 4.1. Therefore, the attached accelerometers also change their directions continuously. Second, as the accelerometer rotates, an induced centripetal acceleration is generated. This acceleration component affects the measured acceleration value, but it cannot be separated from the actual acceleration of the measurement point. Third, these accelerometers are designed to use a high-pass Butterworth filter with a cut-off frequency of 0.1 Hz to eliminate the constant gravitational acceleration. When such an accelerometer rotates, the recorded gravitational acceleration no longer stays constant but fluctuates like a combination of two harmonic functions with frequencies of 1.5 – 2 Hz (same as the lameness component's frequency) and of 3 – 4 Hz (same as the normal component's frequency). Hence, gravity is not exactly eliminated by the Butterworth filter and it affects the output acceleration value. To eliminate the errors from these three sources and obtain true vertical accelerations, we need to condition the accelerometer outputs.

Initial analysis shows that this conditioning algorithm is significantly affected by the sensor's tilt angle and rotational speed. Hence, we incorporate a gyroscope into each sensor box to measure its angular rate and calculate its rotation angle during motion. Then we condition the accelerometer output accordingly. This chapter presents a theoretical algorithm for conditioning the output accelerations, two experiment setups to experimentally validate the developed conditioning algorithm, a method to calculate the rotation angle from the gyroscope signal, an empirical correction algorithm to condition the accelerations, and finally the normal range of horses' head and pelvis rotation angles during trotting.

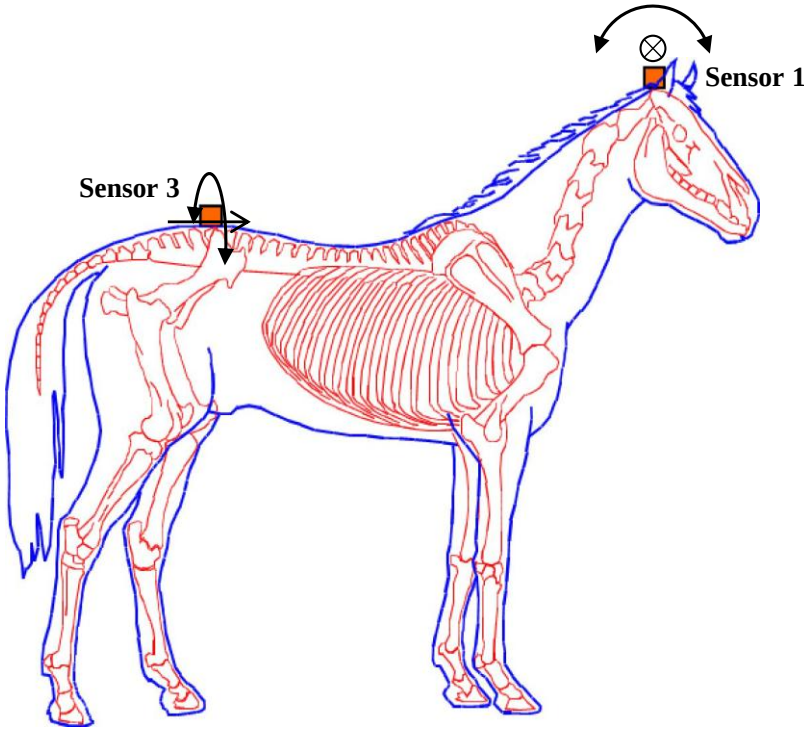

Figure 4.1: The main rotation directions of a horse's head and pelvis.

4.1. Theoretical Algorithm

The theoretical algorithm is developed based on physics and dynamics laws in order to condition the accelerometer output such that it reflects the true vertical acceleration. We consider that a sensor rotates around an instantaneous center O located at the origin of a global XYZ coordinate system as shown in Figure 4.2. Considering the special bone structure and locomotion of a horse, this instantaneous center is assumed to move constantly along the global Y direction during trotting. Hence, the motion of the instantaneous center does not affect the acceleration of the sensor box. The free-body diagram of the sensor box is portrayed below.

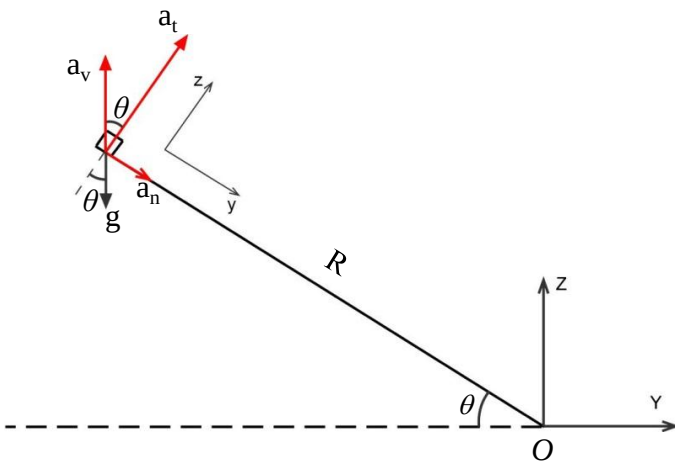

Figure 4.2: Acceleration components of an accelerometer.

Because the accelerometer only measures acceleration along the local z direction, it follows from Figure 4.2 that the accelerometer output a_s includes the motion-induced tangential acceleration a_t and the tangential component of the gravitational acceleration g as

$$a_s = a_t - g\cos\theta \tag{4.1}$$

The actual vertical acceleration a_v of the accelerometer is related to the tangential acceleration a_t, the centripetal acceleration a_n and the rotation angle θ as

$$a_v = a_t \cos\theta - a_n \sin\theta \tag{4.2}$$

The normal acceleration a_n can be calculated as

$$a_n = R\omega^2 = v^2 / R = |\omega v| \tag{4.3}$$

where $\omega = \dot{\theta}$ is the angular velocity, and $v = v_0 + \int_0^t a_t dt$ is the tangential velocity. The initial velocity v_0 is a part of the moving average and is essentially removed by the empirical mode decomposition process. Substituting Eqs. (4.1) and (4.3) into Eq. (4.2) gives

$$a_v = [a_s + g\cos\theta]\cos\theta - \left|\dot{\theta}[v_0 + \int_0^t (a_s + g\cos\theta)dt]\right| \sin\theta \tag{4.4}$$

in which $\dot{\theta}$ is measured by the integrated gyroscope, and θ is the rotation angle obtained from the rotation rate as $\theta = \theta_0 + \int_0^t \dot{\theta} dt$. The initial angle θ_0 is also generally considered as part of the moving average that is removed by the empirical mode decomposition.

Since all the variables in Eq. (4.4) can be calculated or measured using the new sensor that integrates a gyroscope and an accelerometer together, the measured acceleration a_s can be conditioned to report the true vertical acceleration a_v. We designed two experimental setups to examine this theoretical algorithm. Dual-accelerometer testing

uses two accelerometers, and accelerometer-videogrammetry testing uses one accelerometer and one camera-based motion analysis system.

4.2. Dual-Accelerometer Test

Dr. Lopes [2] designed the dual-accelerometer test apparatus shown in Figure 4.3. It translates one sensor in the vertical direction while translates and rotates the second sensor to mimic a sensor on a horse. Comparing the acceleration signals from these two sensors, we can decide whether the second sensor's signal needed to be conditioned to provide the actual vertical acceleration value. Also, if conditioning is needed, we can examine if the proposed theoretical algorithm shown in Eq. (4.4) works well. The apparatus consists of a vertical cylinder, a translational platform, and a rotation bar as depicted in Figure 4.3. The vertical cylinder is 20 cm long and gives a 16 cm vertical excursion for the bearing. Both wireless sensors are place on the translational platform. The sensors are horizontally positioned when the platform is at the middle of the cylinder, and the rotation bar's tip is approximately 30 cm away from the platform at this position. The lubricated bearing system allows moving both wireless sensors up and down in the same path without significant noise. The rotation bar can slide back and forth and rotate the attached second sensor (the sensor on the left in Figure 4.3). For convenience, we call the translating sensor the head sensor and the translating-rotating sensor the pelvis sensor. This configuration allows the pelvis sensor rotate about 15 degrees up and 15 degrees down while translating along the vertical direction.

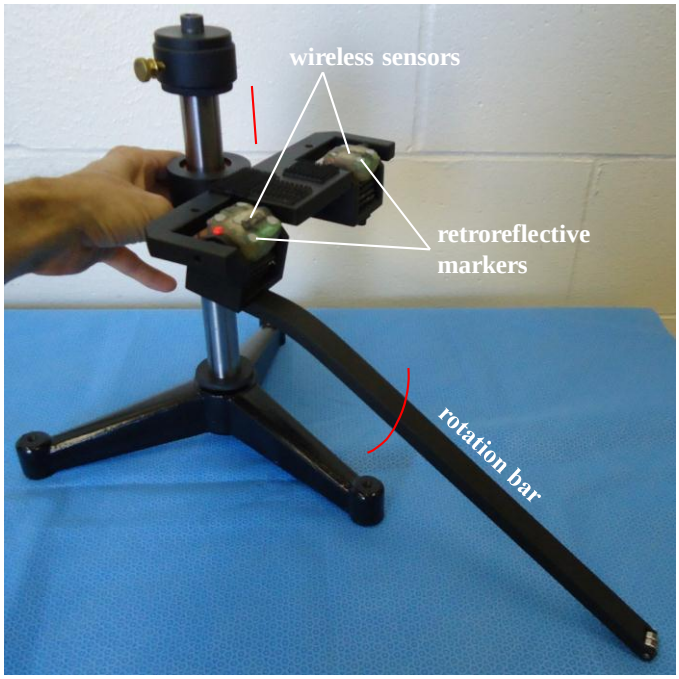

Figure 4.3: The dual-accelerometer test apparatus.

We move the bearing up and down as a horse would move its head (or pelvis) during trotting. For this experiment, we did 9 trials mimicking the head movements of both sound and lame horses. However, we only translate the sensors a little more than half of the vertical cylinder length, and the left sensor only rotates about $\pm 10^{\circ}$ to $\pm 12^{\circ}$, resulting in a rotation range of about 20° to 24°. Then, we compare the accelerations collected by both sensors without any correction. Numerical results show that, for all 9 experiments, the acceleration signals reported from both sensors are almost the same. Figure 4.4(a) shows one typical case in which the two acceleration signals almost overlap with each other.

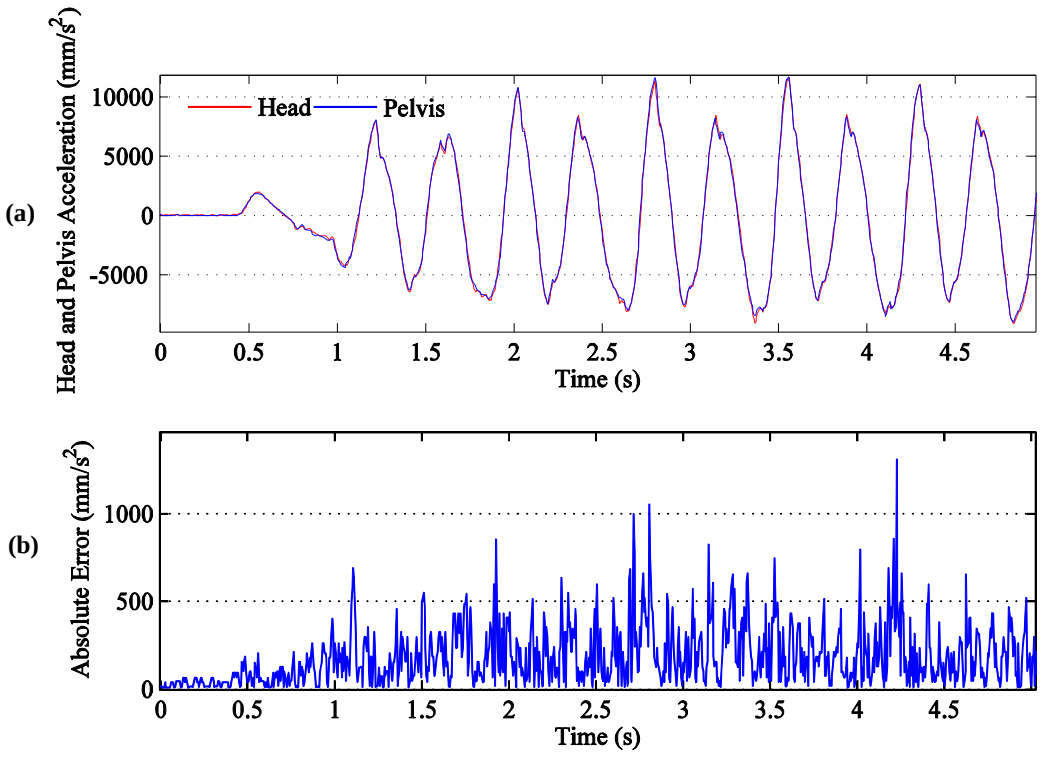

Figure 4.4: Accelerations from both sensors in the dual-accelerometer test: (a) accelerations, and (b) absolute error.

Figure 4.4(b) reports the point wise absolute error between the two acceleration signals. Clearly, the errors are mostly under $500\,\mathrm{mm/s^2}$, while the acceleration range is more than $15,000\,\mathrm{mm/s^2}$. Hence, the relative errors are mostly less than 3.3%. Nevertheless, the ELL processes positions, not accelerations, to characterize lameness. Therefore, we perform two more studies before concluding whether we should use the correction algorithm for this application. First, we integrate the acceleration signals twice to get position signals. After removing the moving average using the empirical mode decomposition (EMD), we compare the two position signals by plotting them together as shown in Figure 4.5(a).

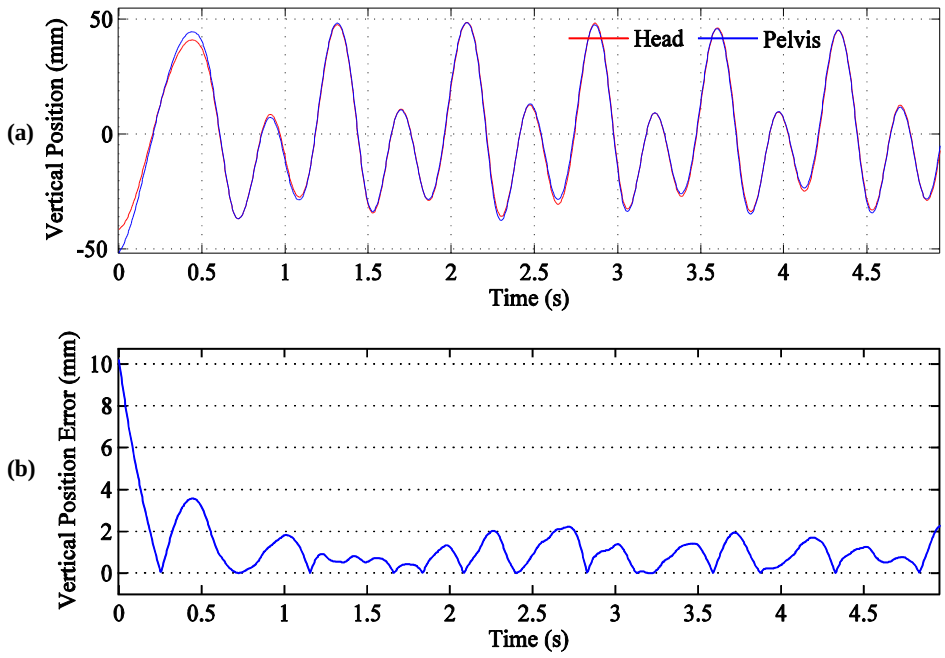

Figure 4.5: Integrated head and pelvis position signals from the dual-accelerometer test: (a) positions, and (b) absolute error.

Figure 4.5(a) reveals that the two position signals almost overlap with each other except at the beginning and a few peak locations. Figure 4.5(b) shows that the point wise absolute errors are mostly less than 2 mm after 0.75 second. On the other hand, the position variation range is about 80 mm. Therefore, the relative errors are mostly below 2.5%. From these two studies, we conclude that the rotation does not have significant influences on the measured vertical acceleration.

Finally, we run the raw acceleration signals through the ELL program to determine the means and standard deviations (SD) of DiffMax and DiffMin. One problem we have with this approach is that we do not have the foot gyroscope signal, which determines the right and left stance phase. Therefore, we fabricate this signal for each experimental data set. The detail of this process is explained in Section 3.4. Once the foot gyroscope signal is

added, ELL can analyze these experimental data for means and standard deviations of DiffMax and DiffMin. Table 4.1 shows that these values are essentially the same for both the head sensor (translation only) and the pelvis sensor (translation and rotation).

Table 4.1: DiffMax and DiffMin from the dual-accelerometer test.

	Mean DiffMax (mm)		SD DiffMax (mm)		Mean DiffMin (mm)		SD DiffMin (mm)	
Trial name	Head	Pelvis	Head	Pelvis	Head	Pelvis	Head	Pelvis
1 – large maxdiff	17.418	17.488	1.569	1.554	-1.663	-1.781	1.042	1.187
2 – large maxdiff	16.822	16.656	1.532	1.563	-1.979	-2.044	1.546	1.487
3 – large maxdiff	18.638	18.710	1.006	0.882	-2.458	-2.195	1.137	1.173
4 – large mindiff	0.753	0.493	1.234	1.239	14.460	14.773	1.462	1.834
5 – large mindiff	-3.377	-3.434	2.585	2.518	-15.817	-16.158	2.729	2.243
6 – large mindiff	1.851	1.327	1.190	0.895	15.554	15.481	0.632	1.123
7 – sound	0.037	-0.017	0.864	0.777	-0.559	-0.690	0.928	0.958
8 – sound	-0.182	-0.265	1.379	1.180	-0.858	-0.853	1.087	1.276
9 – sound	0.528	0.616	0.832	0.945	-0.116	0.003	1.102	1.266

From the above three tests, we conclude that the acceleration recorded by the translating sensor is essentially the same as that recorded by the rotating-translating sensor under a rotation range of 20 to 24 degrees. The reason we do not see significant difference between the two acceleration signals is that the rotation angles are not large. Analyzing Eq. (4.4) for a small rotation angle we can see that

$$a_v = [a_s + g\cos\theta]\cos\theta + \left|\dot{\theta}\int_0^t (a_s + g\cos\theta)dt\right|\sin\theta \approx a_s + g \tag{4.5}$$

First, when θ fluctuates from -12 to 12 degrees, $\cos(\theta)$ is very close to 1, ranging from 0.978 to 1.0. Hence,

$$[a_s + g\cos\theta]\cos\theta \approx [a_s + g\cos\theta] \approx a_s + g \tag{4.6}$$

Second, since the sensor rotates according to the up and down motion, the angular velocity is also a combined harmonic function with a frequency of about 1.5 – 2 Hz and 3 – 4 Hz as

$$\dot{\theta} = A_1 \sin(4\pi t + \varphi_1) + A_2 \sin(8\pi t + \varphi_2) \tag{4.7}$$

Which means the rotation angle is

$$\theta = \frac{A_1}{4\pi} \cos(4\pi t + \varphi_1) + \frac{A_2}{8\pi} \cos(8\pi t + \varphi_2) \tag{4.8}$$

Because θ ranges from -12 to 12 degrees or -0.209 to 0.209 radian, $\frac{A_1}{4\pi} + \frac{A_2}{8\pi} < 0.209$ radian. Hence $A_1 + A_2 < 0.209 \times 8\pi$ rad/s or $\dot{\theta} < 5.25$ rad/s. Besides, $\sin\theta$ is very close to zero; it ranges from 0 to 0.208. On the other hand, $\int_0^t (a_s + g\cos\theta)dt$ is quite small. Therefore,

$$[a_s + g\cos\theta]\cos\theta \gg \left|\dot{\theta}\int_0^t (a_s + g\cos\theta)dt\right| \sin\theta \tag{4.9}$$

Hence, Eq. (4.4) can be rewritten as

$$a_v \approx [a_s + g\cos\theta]\cos\theta \approx a_s + g \tag{4.10}$$

Because g is a constant, it only serves as an offset value and is removed from the acceleration signal during ELL analysis. As a result, no correction algorithm is needed for this experiment or for rotation with angles ranging from -12 to 12 degrees. To confirm this angle range, we use the gyroscope signal to calculate the rotation angle in these experiments. A detail explanation on this process is presented later in Section 4.3.1.

Below is the table of the maximum and minimum rotation angles in all 9 dual-accelerometer tests.

Table 4.2: The maximum and minimum rotation angles in dual-accelerometer test.

Name	Max Pelvis Angle (Degree)	Min Pelvis Angle (Degree)
1 – large maxdiff	15.720	-10.650
2 – large maxdiff	15.308	-11.948
3 – large maxdiff	16.542	-10.569
4 – large mindiff	9.651	-13.850
5 – large mindiff	10.641	-14.736
6 – large mindiff	9.309	-13.429
7 – sound	11.778	-12.422
8 – sound	11.257	-11.508
9 – sound	11.415	-11.762

We can see that the actual rotation angles range from -15 to about 16 degrees. Consequently, for horses that rotate their heads and pelvises less than this range during trotting, we do not need to condition the measured acceleration signals.

The dual-accelerometer test also brought an attention to us that high frequency noise can affect the accelerometer measurement. Using a normal ball bearing, we can see significant noise in both measured acceleration signals. A few trials show that the acceleration signals from the two sensors do not match at the local maximum peaks. Figure 4.6 compares the two acceleration signals from a trial with a normal ball bearing. We can see in Figure 4.6 (a) that both acceleration signals contain high frequency noise and do not agree with each other. While the two signals agree to some degree, there are serious errors at some of the maximum peaks. Hence, it is necessary to limit the high frequency noise in real horse testing for ELL.

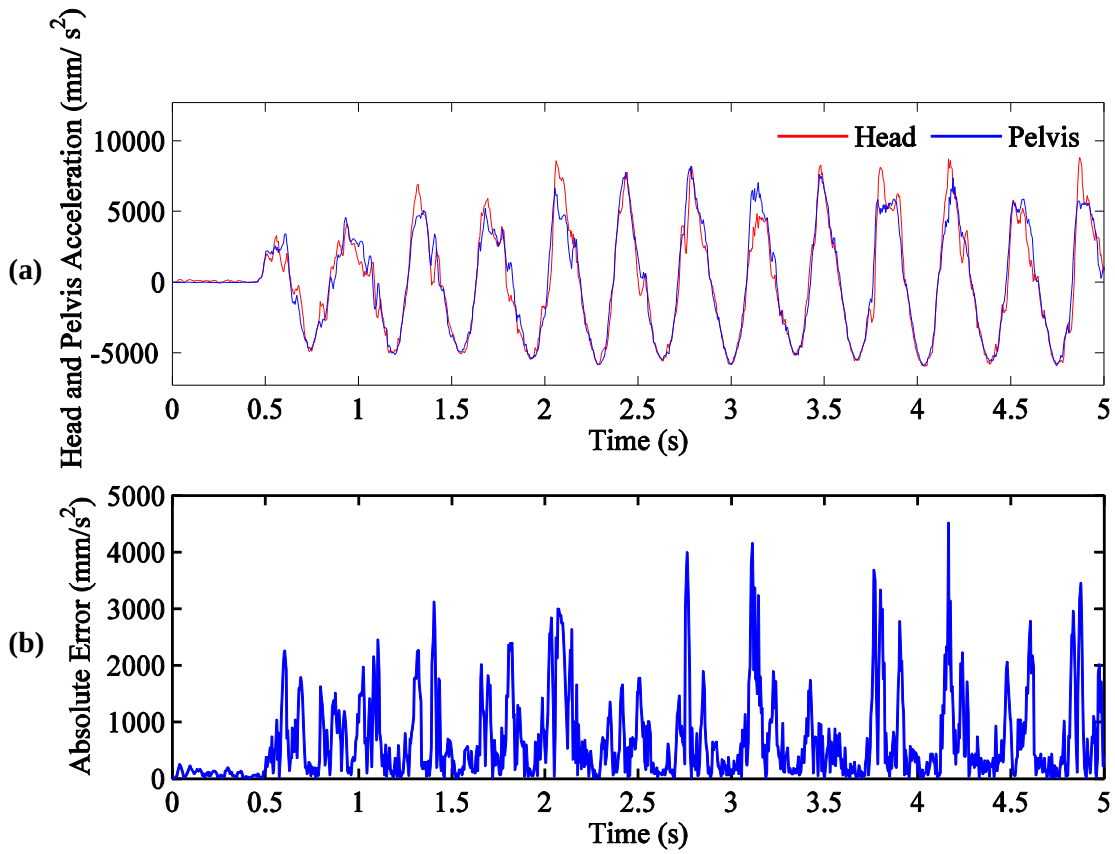

Figure 4.6: Dual-accelerometer test with a ball bearing: (a) head and pelvis acceleration signals, and (b) absolute pointwise error.

4.3. Accelerometer–Videogrammetry Test

In the previous dual-accelerometer test, the sensor is tilted by only about -15 to 15 degrees to each side of the vertical direction. Also, since we mimic horse movements by hand, there may be some inconsistency in the frequency and amplitude over time. The accelerometer-videogrammetry setup is designed to systematically test the accuracy of the wireless sensor under asymmetric and large rotations. Figure 4.7 shows that the apparatus consists of a supporting case, a rotation bar, and a K2007E0 miniature shaker from the Modal Shop, Inc. The rotation bar is connected to the tip of the shaker through a

fix axis such that when the shaker moves its tips, the bar translates and rotates the sensor. At the same time, a high speed camera system records the 3D time-varying positions of the four circular retro-reflective markers on the sensor. The vertical positions of the sensor recorded by the camera system are very accurate and serve as the gold standard for conditioning the accelerometer output.

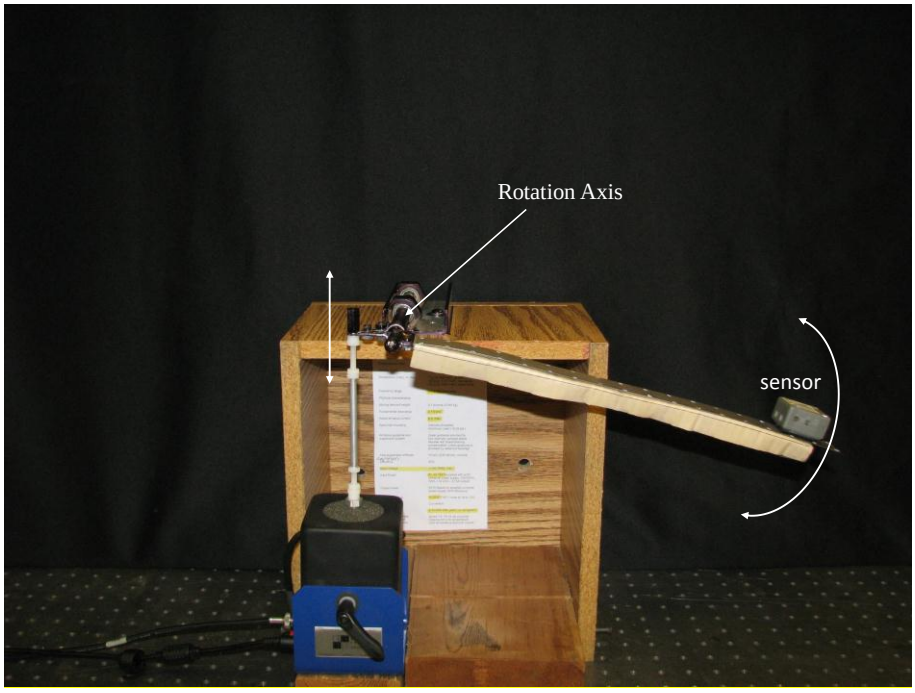

Figure 4.7: The accelerometer-videogrammetry test setup.

The shaker can receive a voltage signal from the phone jack of a laptop computer generated by the MATLAB command "sound" to move its shaker head accordingly. However, the shaker head does not exactly follow the input voltage signal. For example, the shaker head's motion is a distorted harmonic motion while the input voltage to the shaker is a harmonic function. Fortunately, such a setup is still valid for the intended applications because live horse data contain a lot of noise, and the vertical motion signals of the head and pelvis during trotting is not exactly a combination of two harmonic

functions. With an input voltage signal that consists of two harmonics, Figure 4.8 shows one retro-reflective marker's vertical displacement recorded by the camera system. After the initial transient event for about 5 seconds, the sensor motion is consistently similar to the head or pelvis motion of a lame horse during trotting.

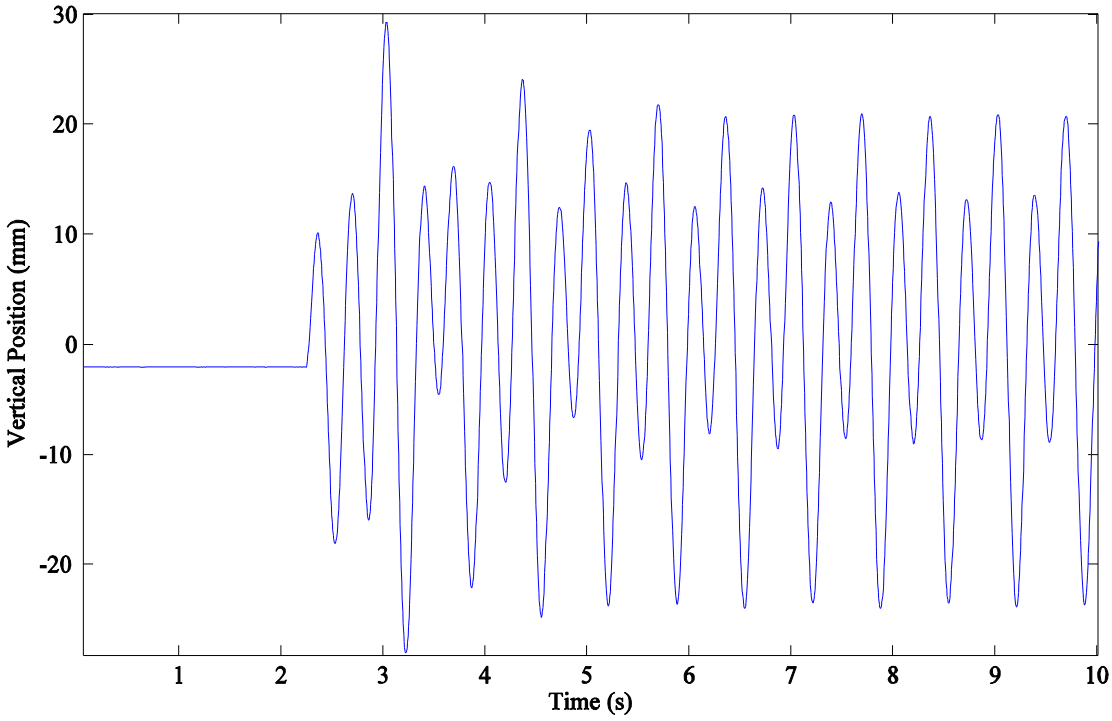

Figure 4.8: A typical sensor motion during the accelerometer-videogrammetry test.

For this experiment, we generate 84 different digital signals using MATLAB such that the shaker head can mimic a variety of head and pelvis movements during trotting. Each signal is a combination of two harmonic functions with a frequency of 3 Hz for the normal component and a frequency of 1.5 Hz for the lameness component. We created two sets of digital signals. A set of 42 signals is to simulate calm horses that move their heads and pelvises little during trotting, and another set of 42 signals is to simulate active horses that move their heads and pelvises more. The digital normal component is

$y_{N1} = 0.06\cos(6\pi t)$ for a calm horse and $y_{N2} = 0.12\cos(6\pi t)$ for an active horse. For each type of normal components, we generate different types of lameness with different degrees of severity by changing the phase difference and the amplitude of the lameness component. The lameness component has the following form

$$y_L = A\sin(3\pi t + \varphi) \tag{4.11}$$

In which, φ is the phase difference and is sequentially set at 0, $\pi/4$, $\pi/2$, and $3\pi/4$ radians. These four phase differences allow us to generate the two most general and common types of lameness, which are the Type 1 and Type 3 shown in Figure 1.4. Moreover, A is the amplitude of the lameness component. For each phase difference, A is sequentially set at 0%, 20%, 40%, 60%, 80%, 100%, 110%, 130%, 150%, 160%, 180%, and 200% of the amplitude of the respective normal component. The trials with the lameness component amplitude set at 0% of its normal component amplitude simulate sound horses. On the other hand, trials with the lameness amplitude set at 200% of its normal component amplitude simulate severely lame horses.

Comparing the 84 trials' data collected from the sensor and the camera system, we can examine if the asymmetric, extreme rotations can affect the measured vertical acceleration values. However, direct comparison of the acceleration measured by the sensor with the position measured by the camera system is impossible. Therefore, we perform three assessments to fully understand the effect of rotation. For the first assessment, we differentiate the camera's vertical position signal twice to get the vertical acceleration by using the double curve fitting method shown in Section 3.2. Then, we compare the two acceleration signals. The study described in Section 3.3 shows that this

double derivative is very accurate for these low-frequency signals. It will not introduce much noise and affect our study. Numerical results from the 84 trials indicate that there are significant differences between the camera's vertical acceleration signal and the sensor's acceleration signal. Figure 4.9 plots the acceleration signals obtained from the camera system and the sensor.

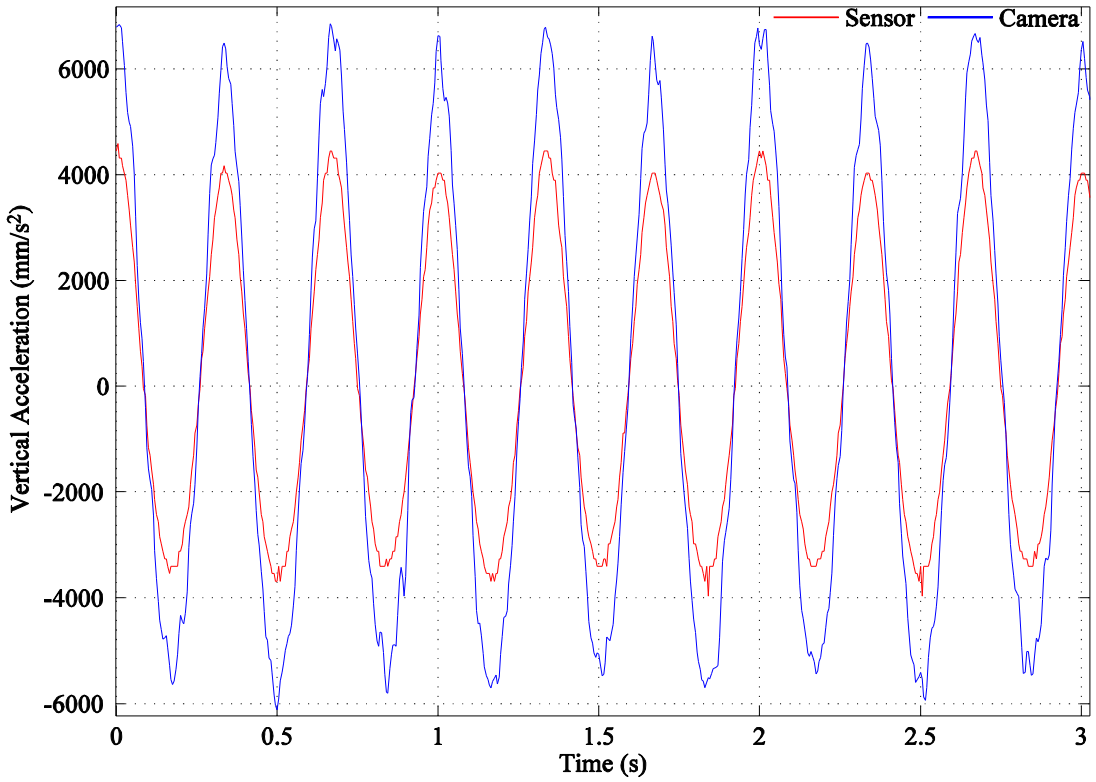

Figure 4.9: Comparison of the sensor's acceleration and the camera's vertical acceleration.

Clearly, the errors are high, especially around the peak areas. According to the theoretical analysis shown in Section 4.2, the accelerations should not deviate so much from each other even with larger rotation angles. Hence, we hypothesize that there is an error in converting the accelerometer's voltage output to the acceleration in mm/s^2. Also, since

the voltage output is linearly dependent on the acceleration, it is highly possible that a constant factor is missing from the following assumed conversion formula:

$$a_{sensor} = (0.0143 \times 9807) V_{dc} \tag{4.12}$$

where V_{dc} represents the acceleration-induced voltage inside the accelerometer. To confirm this hypothesis, we come back to the dual-accelerometer test, where the head sensor is translated only in the vertical direction. If the acceleration conversion formula is correct, there should only be small differences between the accelerations obtained from the head sensor and the one from the camera system. However, we find out that for all 9 trials, the accelerations reported by the head sensor is consistently smaller than the ones recorded by the camera. Figure 4.10(a) illustrates the significant difference between the two acceleration signals from one typical trial.

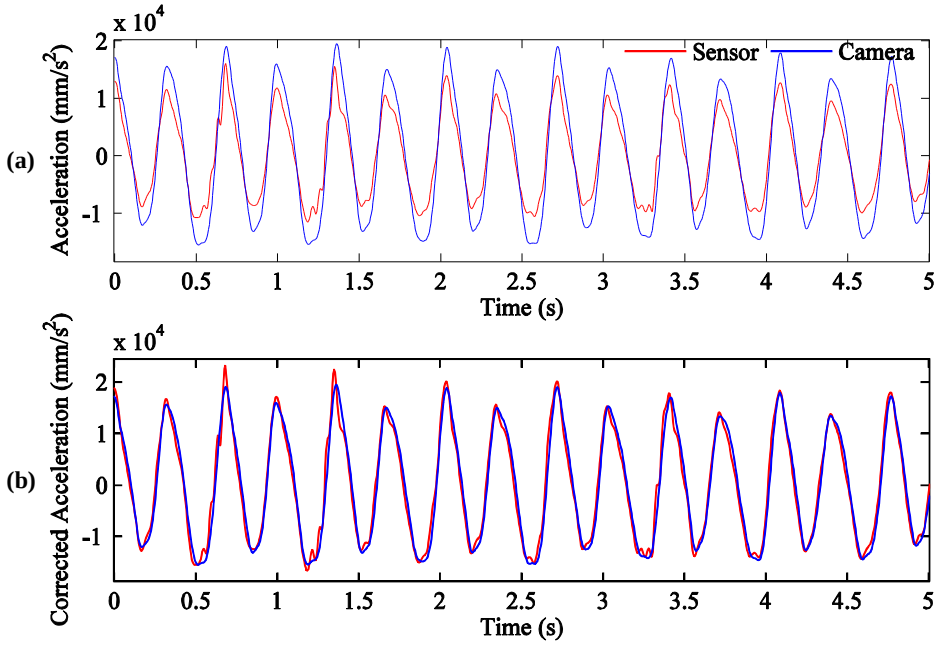

Figure 4.10: Comparison of the sensor's acceleration and the camera's vertical acceleration: (a) without correction, and (b) with correction on the sensor's acceleration.

From this study we can confirm that the acceleration conversion formula is incorrect. To fully check the hypothesis, we attempt to find the constant factor missing from Eq. (4.12). For each of the 9 trials, we detect the local maxima and minima of both acceleration signals calculated from the head sensor (i.e., the non-rotating sensor in Figure 4.3) and the camera system. As we can see from Figure 4.10 (a), the local extrema from both signals align very well with respect to time. In other words, for each local extremum from the sensor's acceleration signal, there is a local extremum from the camera recorded acceleration signal at the same time instant. We take the absolute ratio between each local extremum of the camera's vertical acceleration over the corresponding local extremum of the sensor's acceleration. Then, the average of those absolute ratios is chosen as the correction factor. Figure 4.10 (b) shows that after multiplied by a correction coefficient of 1.4428, the acceleration recorded by the sensor matches the acceleration recorded by the camera system very well. Doing the same steps for all 9 trials, we found that the 9 correction factors are reasonably close to each other. Hence, we conclude that the hypothesis is correct and the average correction coefficient is 1.48. In other words, the acceleration conversion equation should be:

$$a_{sensor} = 1.48 \times (0.0143 \times 9807) V_{dc} \tag{4.13}$$

Applying Eq. (4.13) to convert the sensor's acceleration signals in the accelerometer-videogrammetry test, we can assess the effect of large rotation on accelerometer measurements. For most of the 84 trials, the two acceleration signals calculated from the sensor and from the camera system match quite well, but not perfect. There are small errors that may cause serious effects in the integrated position signal. Figure 4.11 shows a pair of acceleration signals from the accelerometer-videogrammetry tests.

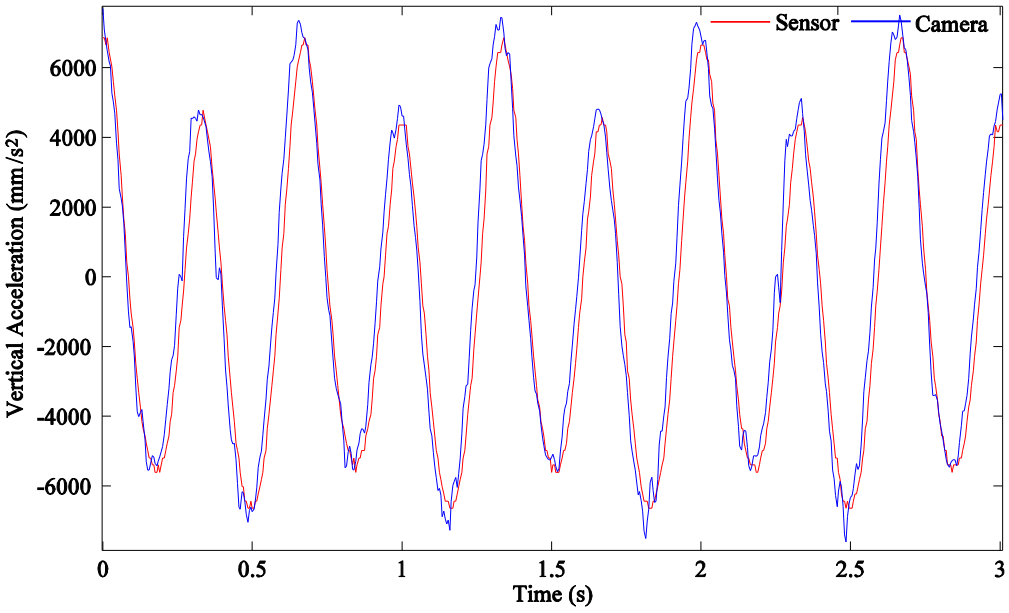

Figure 4.11: Comparison of a sensor's acceleration and a camera's vertical acceleration from the accelerometer-videogrammetry test.

Furthermore, the ELL uses displacements instead of accelerations to evaluate horse lameness. Therefore, we also compare velocity and displacement signals from both the wireless sensor and the camera system before concluding whether we should condition the sensor's accelerations for large and asymmetric rotation effect.

The second test assesses the errors due to numerical integration by comparing the velocity signals obtained from both the sensor and the camera system. Numerically integrating the acceleration signal from the sensor once, we have the sensor velocity signal. Numerically differentiating the position signal from the camera system once using the proposed curve fitting approach, we have the camera velocity signal. Comparing these two signals against each other, we found that the relative errors do not increase

much comparing to the relative errors of acceleration signals. Figure 4.12 shows the velocity signals of the trial that has the acceleration signals shown in Figure 4.11.

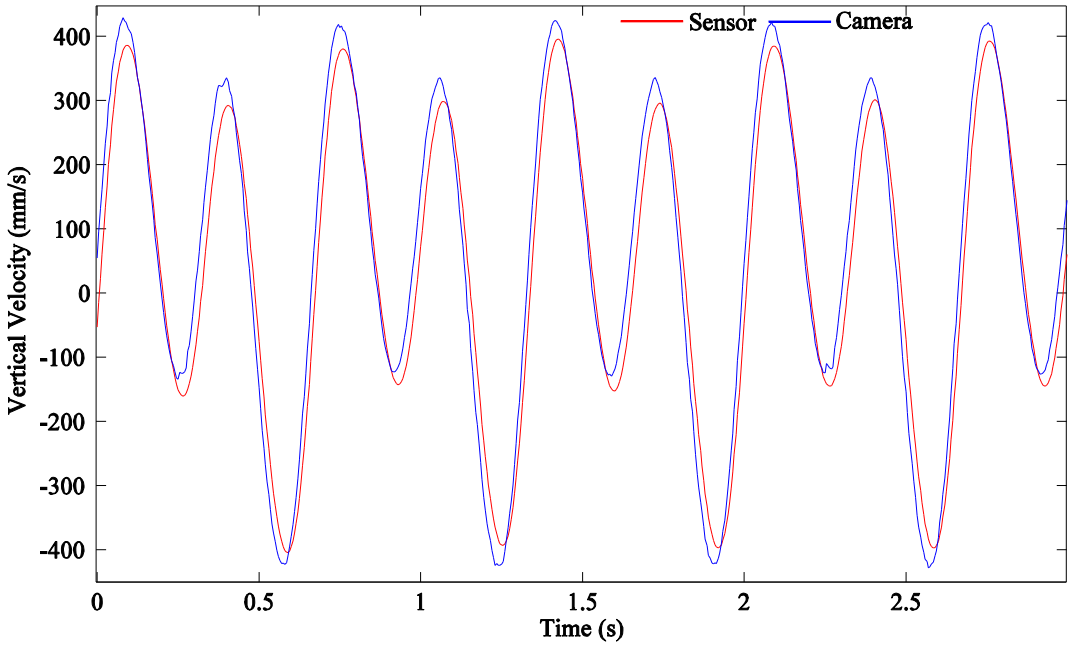

Figure 4.12: Comparison of a sensor's velocity and a camera's vertical velocity from the accelerometer-videogrammetry test.

From this study, we conclude that the single numerical integration does not significantly increase the error. However, an interesting phenomenon is observed. Note that, in Figure 4.12, the local maximum peaks of the sensor signal are consistently lower than those of the camera signal. On the other hand, the sensor signal's minimum peaks around $-100\ mm/s$ are consistently lower than those of the camera signal, while for the minimum peaks around $-400\ mm/s$, the situation is reversed. If we consider taking the DiffMax and DiffMin of these velocity signals for lameness evaluation, the mean of DiffMax from both signals will be quite similar, but the mean of DiffMin from the sensor signal will be significantly lower than that from the camera signal. For this reason, we

expect greater errors between the position signals acquired from the sensor and the camera system. However, directly comparing the position signals is very difficult because double numerical integration is needed. Numerical differentiation does not introduce any moving average, but numerical double integration generates a huge moving average as mentioned in Chapter 1. Eliminating the moving average component perfectly from a position signal requires advanced signal processing techniques like the empirical mode decomposition. Therefore, we check the effect of rotation on the accelerometers by using the ELL program. The third test sequentially runs acceleration signals from the sensor and position signals from the camera system through ELL. Notice that numerical integration is taken out of ELL when running position signals from the camera system. Also, a right front limb gyroscope signal is numerically created as shown in Section 3.4. Comparing the means and standard deviations of DiffMax and DiffMin calculated from each pair of signals from the sensor and the camera system, we can assess the effect of rotation on lameness evaluation. The result for this test is reported in Table B.1 (Appendix B). We can see that there are significant differences between the means of DiffMax and DiffMin between analyses using the camera system position signals and the sensor acceleration signals. Hence, a correction algorithm for accelerometer outputs is needed in cases where the rotation angles are large and asymmetric. The rotation angle in these experiments can be calculated using the camera system or the gyroscope sensor integrated with the accelerometer. Section 4.3.1 estimates the rotation angle in these experiments and also explains the method to calculate the rotation angle using the gyroscope sensor.

4.3.1. Calculation of Rotation Angles

The sensor's rotation angle is defined to be the angle between the sensor's top surface and the horizontal plane. First, we calculate the rotation angle using the displacement data measured by the camera system. Then we use that result to configure the gyroscope outputs. Finally, the rotation angle and speed signals from the gyroscope are used in Eq. (4.4) to condition the accelerometer outputs.

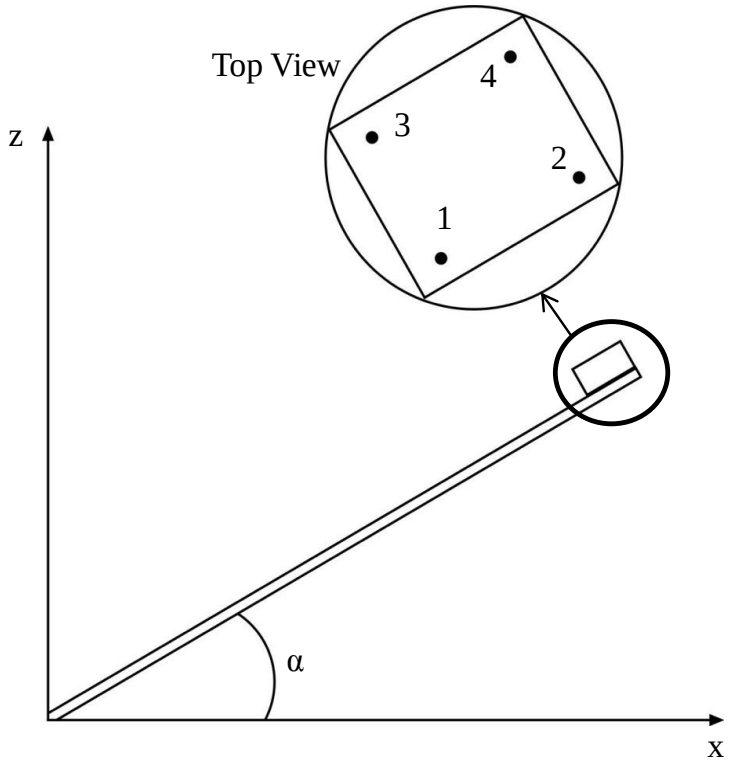

Figure 4.13: The sensor's rotation angle α.

Let (x_1, y_1, z_1), (x_2, y_2, z_2), (x_3, y_3, z_3) and (x_4, y_4, z_4) be the 3D coordinates of the four retro-reflective markers on the sensor, as shown in Figure 4.13. These coordinates are captured and reported by the camera system at 200 times per second during the accelerometer-videogrammetry test (see Figure 4.7). In each trial, because of the

experiment setup, the sensor only moves in a unique vertical plane. Therefore, we can calculate the rotation angle α using either coordinates of markers 3 and 4 or coordinates of markers 1 and 2 as

$$\alpha = \arctan\left(\frac{z_4 - z_3}{\sqrt{(x_4 - x_3)^2 + (y_4 - y_3)^2}}\right) = \arctan\left(\frac{z_2 - z_1}{\sqrt{(x_2 - x_1)^2 + (y_2 - y_1)^2}}\right) \qquad (4.14)$$

Since the rotation angle calculated using coordinates of markers 3 and 4 is quite close to the angle calculated using coordinates of markers 1 and 2, it confirms that the sensor only moves in one unique vertical plane. For the 42 trials of calm horses, α ranges roughly from -10 to -25 degrees. While for the 42 trials of active horses, α can ranges from 3 to -35 degrees. Figure 4.14 reports the rotation angle ranges of all 84 experiment trials, and Figure 4.15 shows one calm horse rotation angle signal.

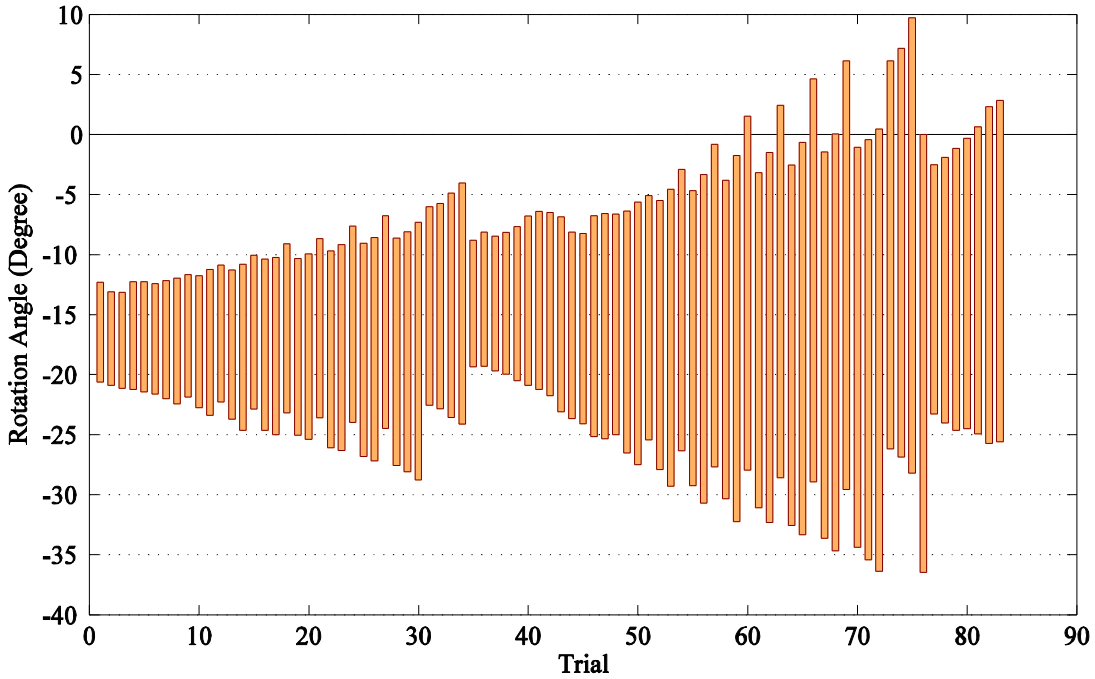

Figure 4.14: Rotation angle ranges in 84 accelerometer-videogrammetry test trials

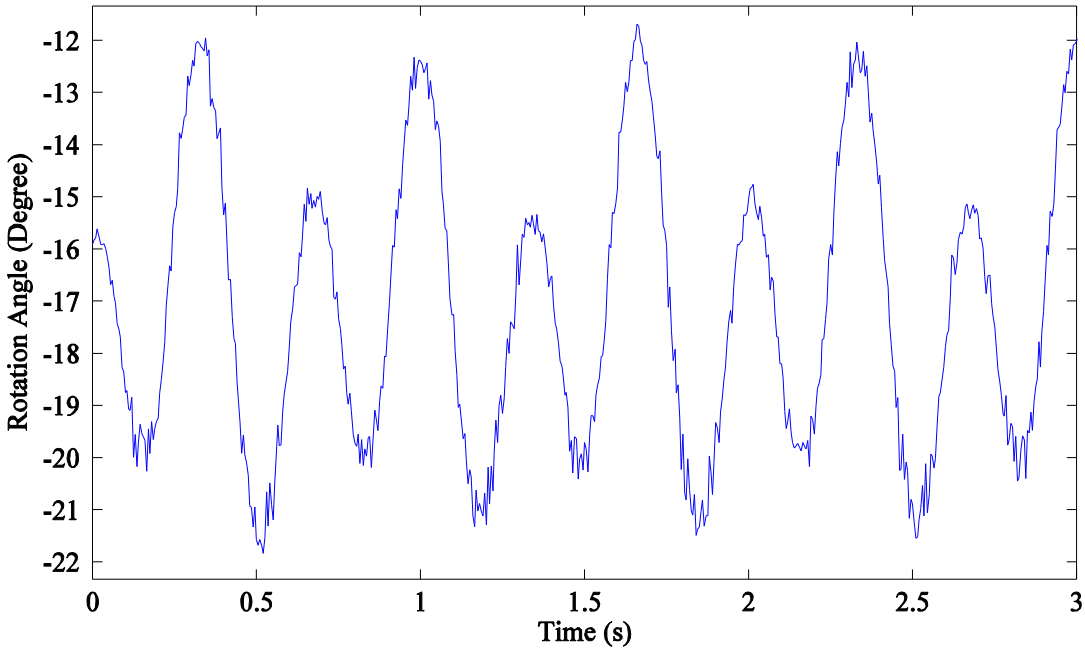

Figure 4.15: The sensor rotation angle caculated using the displacement data measured by the camera system.

We can see that the rotation angles amplitude in 42 trials of calm horses (about 5-7 degrees) are smaller than those from the dual-accelerometer test (10 – 15 degrees). Therefore, the sensor measurement is expected to be correct. However, the means of DiffMax and DiffMin calculated from the sensor acceleration signals are quite different from the means of DiffMax and DiffMin calculated from the camera position signals (see Table B.1, Appendix B). On the other hand, the actual rotation angle ranges are different between the two experiments. For the dual-accelerometer experiment (see Figure 4.3), the rotation angle range is around -15 to 15 degrees. While for the calm horse experiment using the setup shown in Figure 4.7, the range is around -10 to -25 degrees. We can see that the rotation angles in the second test deviate so much from zero. Such asymmetric and extreme values in the rotation angle are believed to affect the accelerometer measurement most.

Next we configure the gyroscope sensor such that it can report the true rotational velocity in degrees per second. Since the gyroscope voltage output is proportional to the rotational velocity, the rotational velocity can be obtained by multiplying the gyroscope output with a constant factor. Notice that a constant offset is not concerned because the rotational velocity signal has a zero mean.

The converting constant factor for the gyroscope sensor is determined using the same method used to determine the correction coefficient used in Eq. (4.13) for the wireless accelerometer. First, we numerically differentiate the rotation angle signals calculated from the camera system data to get angular velocity signals. Then, we determine the local extrema values from both signals, i.e., the gyroscope voltage output and the camera system's angular velocity. Next, we take the absolute ratio of each pair of extrema locating at the same time. The average of these absolute ratios is taken as the converting coefficient. From the 84 trials in the accelerometer-videogrammetry test, the average converting coefficient is 2.35 (degree/s)/mV. Figure 4.16 (a) compares the angular velocity signals calculated from the gyroscope sensor and the camera system.

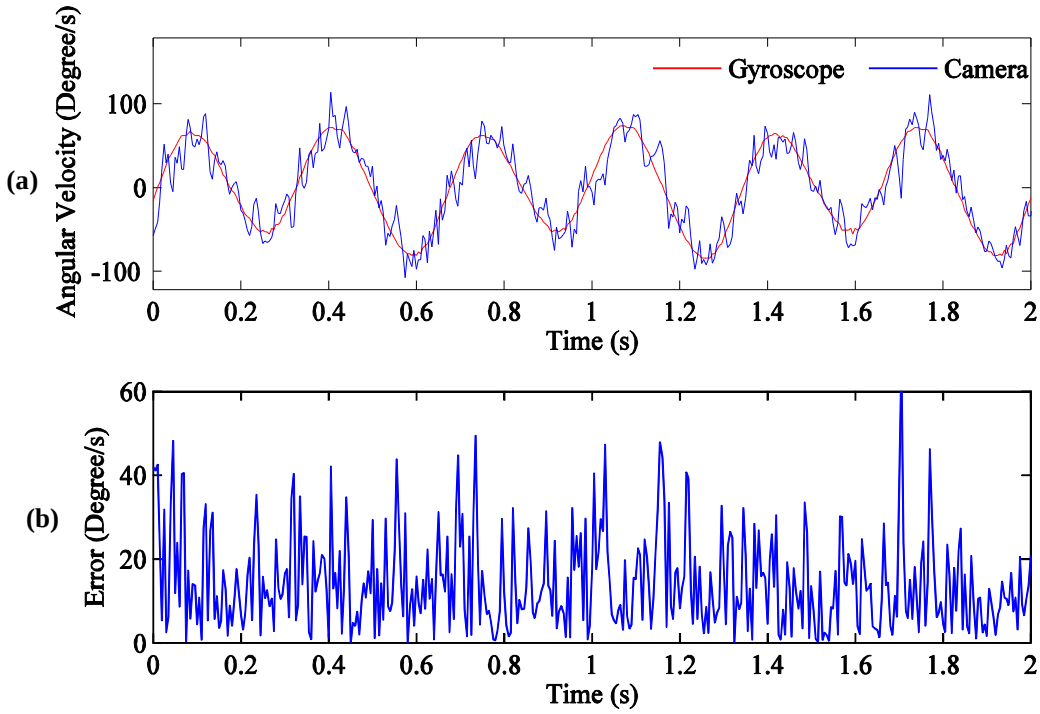

Figure 4.16: Angular velocities measured by the gyroscope sensor and the camera system: (a) comparison of the two velocities, and (b) difference between the two velocities.

We can see that the angular velocity signal from the camera system is very noisy, and the absolute error is quite large as shown in Figure 4.16 (b). Note that, because of this high level of noise, we have to smooth the angular velocity signal from the camera system before detecting the coefficient above. Besides, the trend of the angular velocity is almost the same. That means the angular velocity calculated from the gyroscope data should be correct. Integrating the gyroscope's angular velocity once, we have the rotation angle. Note that the initial angle is provided by the camera data in these cases. Numerical results show that the gyroscope's rotation angle signals are very close to the actual rotation angle calculated from the camera system data. Figure 4.17 shows the rotation angle signals

calculated from the gyroscope and the camera system. These rotation signals are calculated from the same trial reported in Figure 4.16.

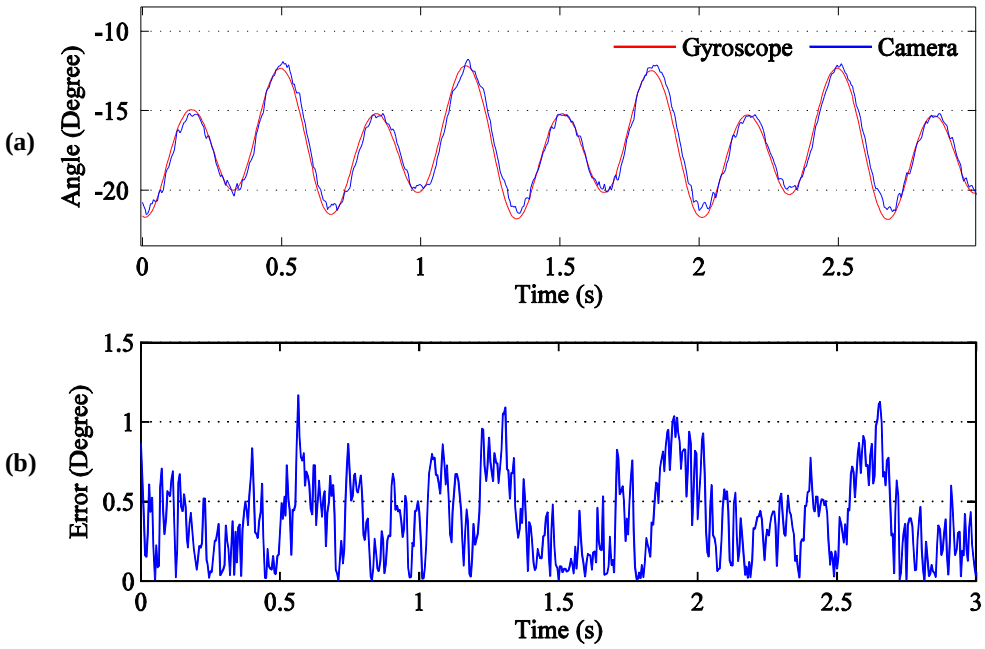

Figure 4.17: Rotation angles measured by the gyroscope sensor and the camera system: (a) comparison of the two angles, and (b) difference between the two angles.

We can see that the angle signals almost overlap with each other. Furthermore, the absolute errors are very small, mostly less than one degree. Note that the errors are high at peak angles; this implies that the gyroscope is not accurate when the angular velocity changes sign. For the 84 trials, the errors are consistently quite small. Hence, we accept this method to calculate angular velocities and rotation angles of the sensor.

4.3.2. Theoretical Correction of Acceleration

This section presents the numerical results of conditioning the sensor's acceleration outputs to remove the rotation effect using the theoretical approach explained in Section

4.1. Entering the angular velocity and the rotation angle calculated from the gyroscope sensor into Eq. (4.4) should give the true vertical acceleration. Ideally, this conditioned acceleration should be equal to the vertical acceleration calculated from the camera data. Numerical result shows that the conditioning process decreases the acceleration value. Figure 4.18 compares a sensor's original acceleration signal with a conditioned one.

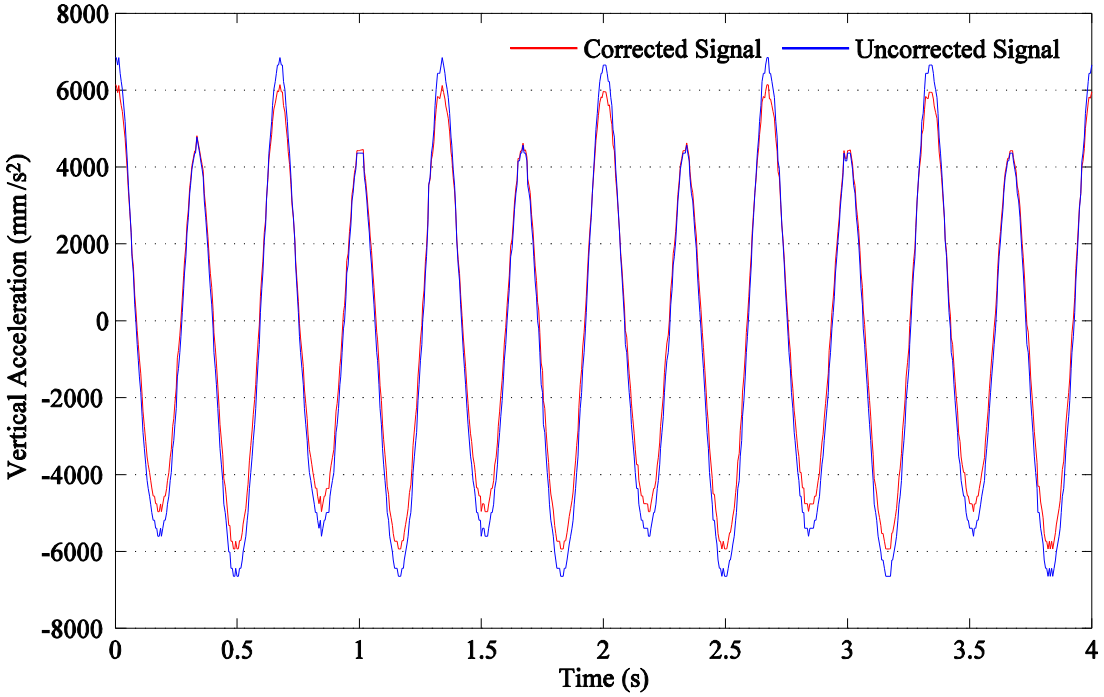

Figure 4.18: Uncorrected and corrected acceleration signals.

Also, Figure 4.19 demonstrates that the conditioned acceleration signal from the trial above is smaller than the camera vertical acceleration signal, especially around the highest and lowest peaks. Hence, the uncorrected acceleration signal is actually closer to the camera's vertical acceleration signal than the corrected acceleration signal is. The correcting algorithm actually creates more acceleration error.

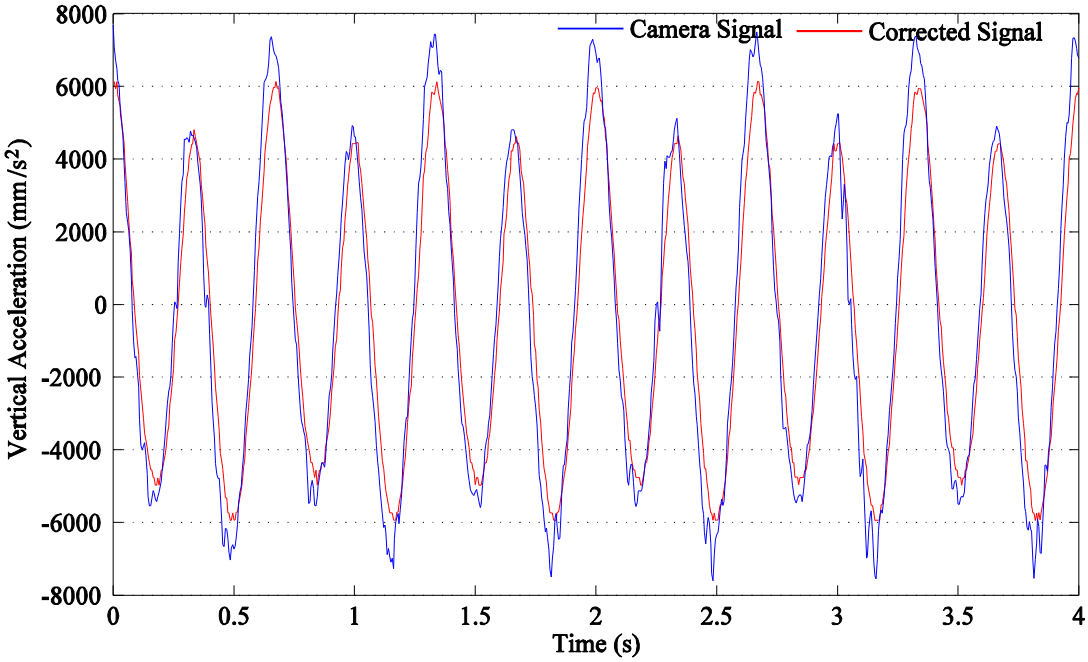

Figure 4.19: The vertical acceleration from the camera data and the corrected vertical sensor acceleration.

Next, we process the conditioned accelerations using ELL and compare their mean values of DiffMax and DiffMin with those obtained from the camera vertical position signals. Table B.2 in Appendix B reports the means and standard deviations of DiffMax and DiffMin of accelerometer-videogrammetry test trials using the camera position signals and the conditioned acceleration signals. It can be inferred from Table B.2 that the theoretical correction method shown in Eq. (4.4) does not improve the accuracy of the sensor measurement. The difference in the means of DiffMax and DiffMin obtained from the two signals can be easily visualized using linear curve fitting. Figure 4.20 shows the linear relationship between the means of DiffMax obtained from the conditioned acceleration signals and the means of DiffMax obtained from the camera vertical position

signals. Notice that only trials with the means of DiffMax in the ranges from -40 mm to 40 mm are used because any values beyond that range are unrealistic in live horses.

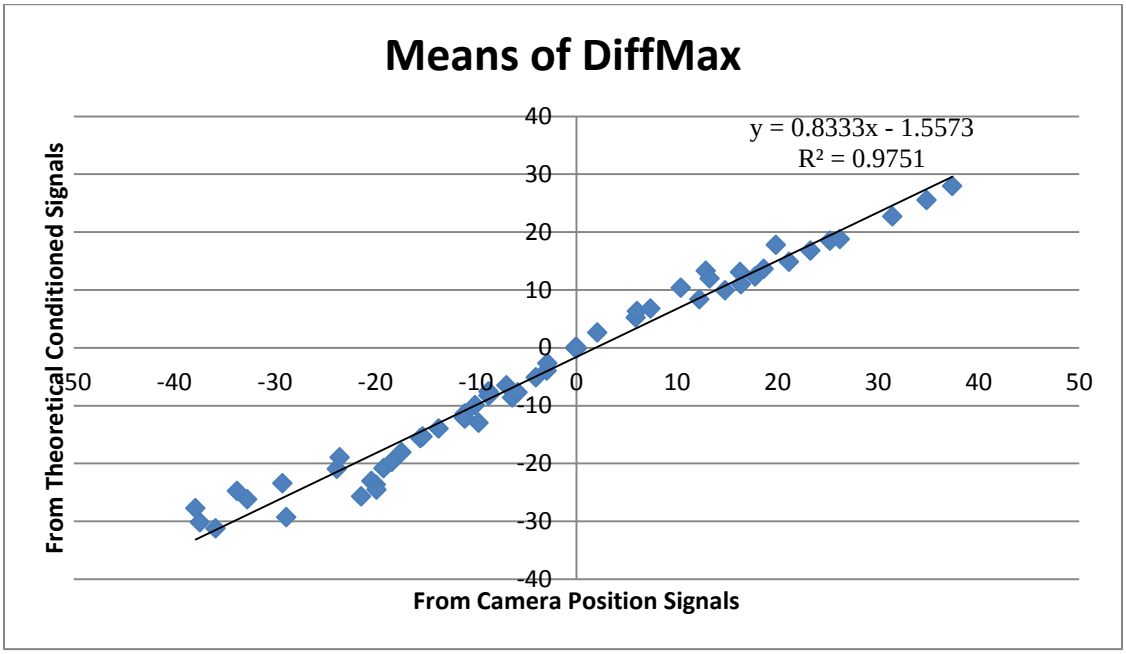

Figure 4.20: Linear relationship between the means of DiffMax from the use of two different signals.

The relationship between the means of DiffMax from both sources is highly linear because the R^2 value is very close to 1. R^2 is the coefficient of determination that indicates how well the linear regression curve fit the data, defined as

$$R^2 \equiv 1 - \frac{SS_{error}}{SS_{total}} \tag{4.15}$$

In which, SS_{total} is the total sum of squares calculated as

$$SS_{total} = \sum_i (y_i - \bar{y})^2 \tag{4.16}$$

And SS_{error} is the sum of squares of residuals calculated as

$$SS_{error} = \sum_i (y_i - f_i)^2 \tag{4.17}$$

Here, $\bar{y}$, y_i and f_i are the mean of the data values, data value at i and the fitted linear curve value at i respectively.

We can see from Figure 4.18 that the means of DiffMax from the conditioned acceleration signals are consistently smaller than those from the camera vertical position signals. The difference is about 17% as the slope is 0.833 instead of 1.0. We conclude that the theoretical approach does not help improve the sensor's acceleration signal.

4.4. Empirical Correction Method

First, the empirical correction method identifies how different conditioning factors affect the sensor acceleration signals and the means of DiffMax and DiffMin. Then it corrects the sensor acceleration signals such that their means of DiffMax and DiffMin get as close to those calculated from the camera position signals as possible. We can see from Eq. (4.4) that the major variables affecting the accelerometer's measurement are the gravity g and the rotation angle θ. More specifically, we believe that $g\cos\theta$ and $\cos\theta$ play a significant role in correcting the accelerometer's output. Since $g\cos\theta$ has the unit of acceleration, we try adding and subtracting the sensor acceleration signals by $g\cos\theta$. We found that both DiffMax and DiffMin decrease if $g\cos\theta$ is added to the sensor acceleration signals. And both DiffMax and DiffMin increases if $g\cos\theta$ is subtracted from the sensor acceleration signals. On the other hand, $\cos\theta$ has no unit. Hence, we try

to multiply and divide the acceleration signal by $\cos\theta$. The effects of these two corrections, along with adding and subtracting $g\cos\theta$ from the acceleration signals are reported in Table 4.3

Table 4.3: Effects of different correction methods on DiffMax and DiffMin.

Correction Type	DiffMax	DiffMin
$+g\cos(\theta)$	Decreases	Decreases
$-g\cos(\theta)$	Increases	Increases
$\times\cos(\theta)$	Decreases	Increases
$\div\cos(\theta)$	Increases	Decreases

Utilizing Table 4.3, we correct the sensor's acceleration signal such that the means of both DiffMax and DiffMin of each trial get as close to the means of DiffMax and DiffMin calculated from the camera signals as possible. Numerical results show that lameness types 1 and 3 require two different correction equations. For Type 1 lameness, we use

$$a_c = (a_s - 2g\cos\theta)\times\cos\theta \tag{4.18}$$

For Type 3 lameness, we use

$$a_c = (a_s - g\cos\theta)/\cos\theta \tag{4.19}$$

Lameness types 2 and 4 are just different cases of lameness types 1 and 3, respectively. Hence, we also use Eqs. (4.18) and (4.19) to correct for lameness types 2 and 4, respectively. Table B.3 of Appendix B reports the means and standard deviations of DiffMax and DiffMin calculated from the camera position signals and from the empirically corrected accelerations. We can see that the means of DiffMax and DiffMin from both sources of signals match really well. Also, using linear curve fitting, we can

see that the means of DiffMax calculated from the corrected acceleration signals is almost equal to those calculated from the camera position signals. Figure 4.21 shows the linear relationship between the means of DiffMax from both signals.

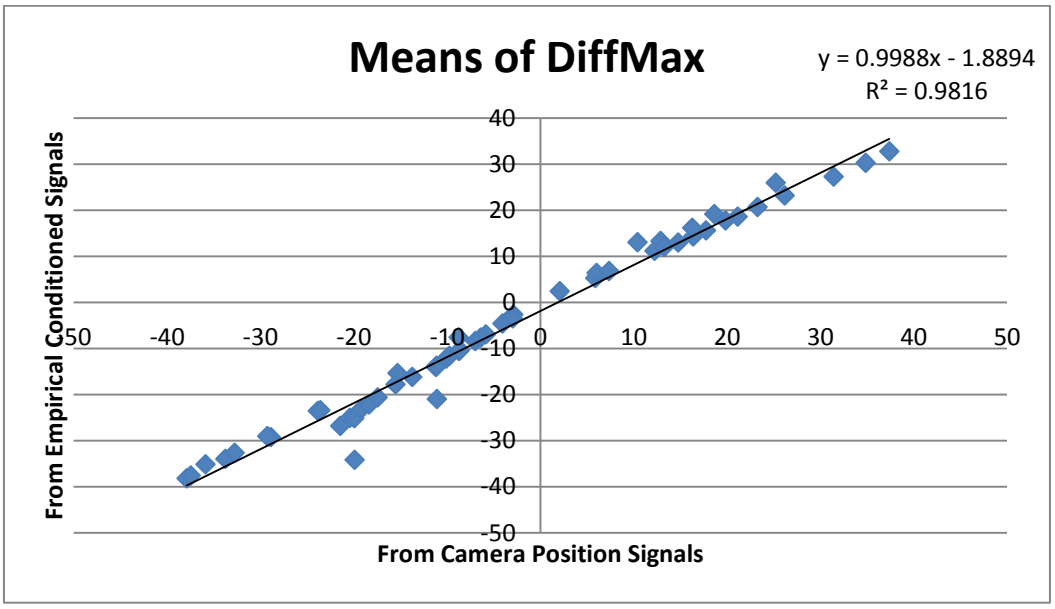

Figure 4.21: Linear relationship between the means of DiffMax from the use of two different signals.

While the empirical correction method greatly improves the accuracy for the means of both DiffMax and DiffMin, it uses two different equations to correct for DiffMax and DiffMin for different cases. This is unusual because theoretically, one correction algorithm should be able to correct all recorded accelerations for rotational effects. Examining the acceleration signals more closely reveals that the accelerometers may experience a measurement delay when accelerations change sign. Thus, the ELL needs two different correction algorithms.

Comparing a sensor acceleration signal with a camera vertical acceleration signal, we can see that at some peaks, the two signals match very well. However, at many other peaks,

the errors are much higher. An example of this phenomenon is shown in Figure 4.22, where an uncorrected acceleration signal is compared with a camera vertical acceleration signal.

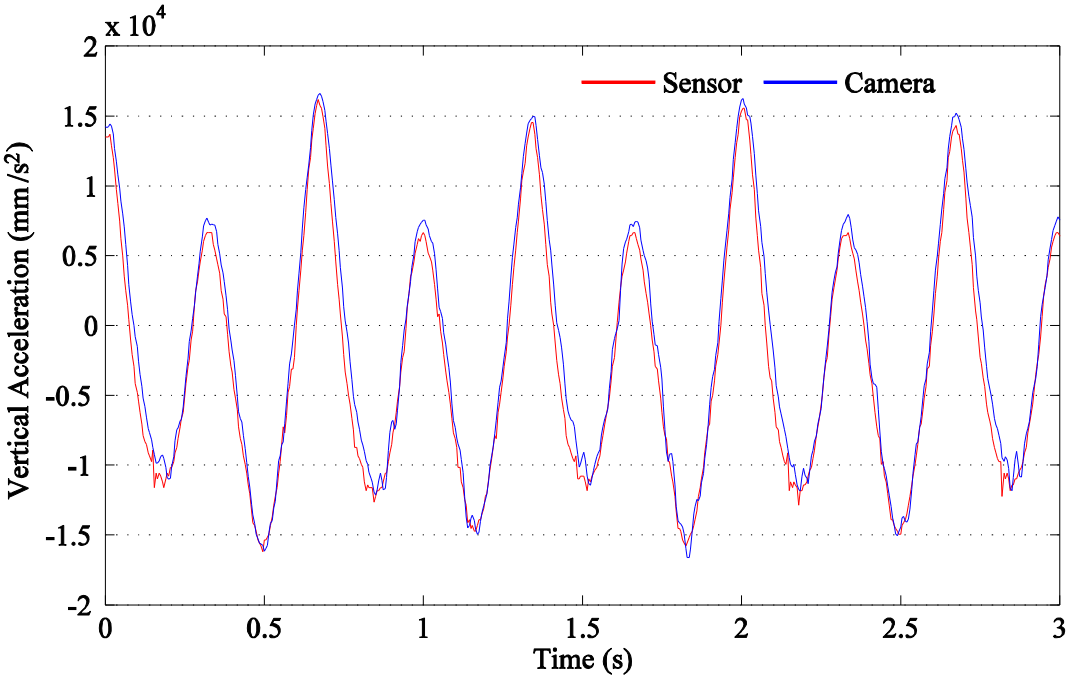

Figure 4.22: The original sensor acceleration and the vertical acceleration from the camera.

We can see that the two signals match quite well with each other. However, there are some differences at the lower maximum peaks as well as the segments from each higher maximum peak to the immediate following minimum peak. Hence, we infer that the inertia sensor experiences a measurement delay when acceleration changes direction. For every period, this delay causes a serious effect after numerical integration. As mentioned earlier in Section 4.3, this delay causes some miscalculation at the maximum and minimum peaks of the velocity signal. Consequently, it affects the calculation of only either DiffMax or DiffMin of the position signal. The problem stays not only in the accelerometer miss-measurement, but also in numerical integration. This explains why

we need two different acceleration corrections for different types of lameness. A closer look at Figure 4.23 and 4.24 can reveal the answer. Figure 4.23 displays the velocity signals calculated from the sensor and the camera data used in Figure 4.22. This signal is similar to the lameness Type 1 position signal.

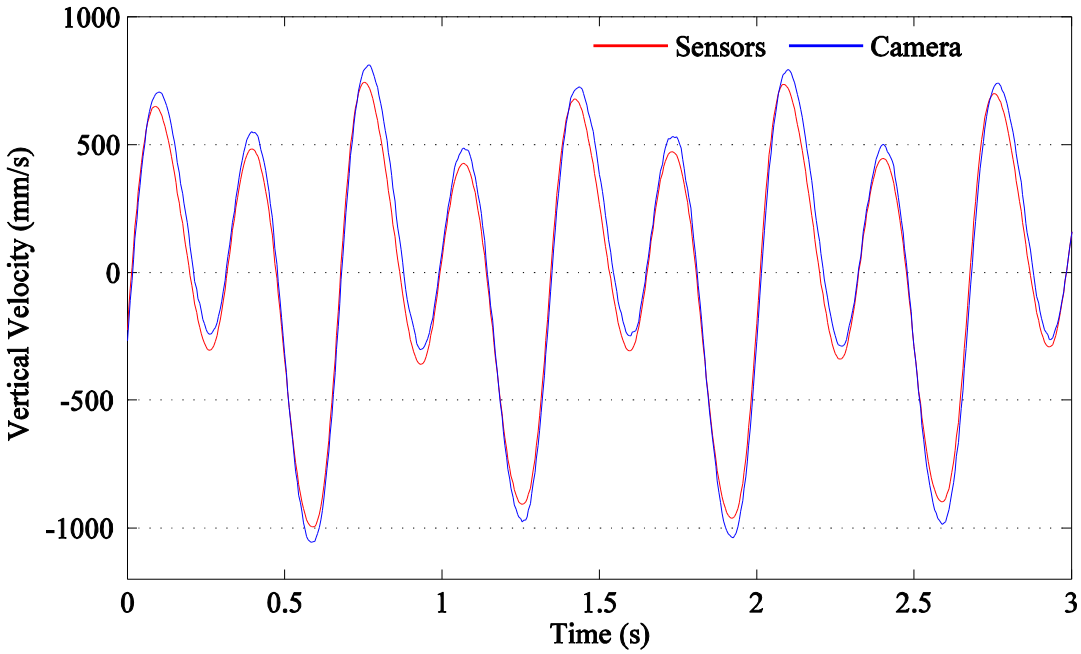

Figure 4.23: Vertical velocity signals from the sensor and the camera under the Type 1 lameness.

It can be inferred from Figure 4.22 that the numerical integration process not only increases the relative error but also underestimates some peaks while over estimates the others. All the maximum peaks and all the minimum peaks around $-300\ mm/s$ from the sensor signal are smaller than those from the camera signal. On the other hand, all the minimum peaks around $-1000\ mm/s$ from the sensor data are higher than those from the camera signal. This effect will cause the over estimation of DiffMax but not the DiffMin in the position signal as illustrate in Figure 4.24. Since the position at each time instant is the area under the velocity signal from zero to that time instant, the area

difference E_1, E_2, E_3 and E_4 (positive by definition) shown in Figure 4.24 contribute to the difference at the maximum and minimum peaks between the camera and sensor signals.

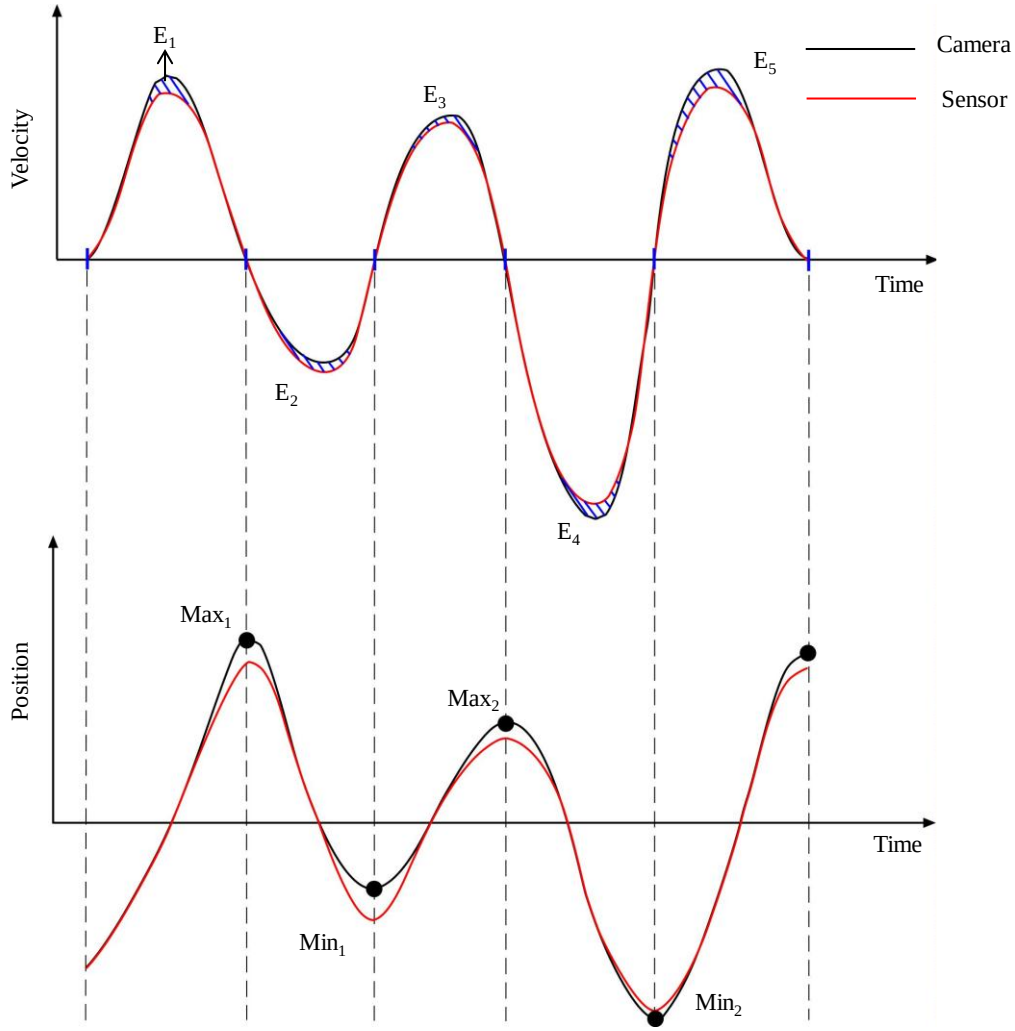

Figure 4.24: Numerical integration from velocity to position.

Let $CMax_1$, $CMax_2$, $SMax_1$ and $SMax_2$ be the maximum values of the camera and sensor position signals at the time instants Max_1 and Max_2, respectively. And

$CMin_1$, $CMin_2$, $SMin_1$ and $SMin_2$ be the minimum values of the camera and sensor position signals at the time instants Min_1 and Min_2, correspondingly. We have

$$\begin{aligned} CMax_1 - SMax_1 &= E_1 \\ CMin_1 - SMin_1 &= E_1 + E_2 \\ CMax_2 - SMax_2 &= E_1 + E_2 + E_3 \\ CMin_2 - CMin_2 &= E_1 + E_2 + E_3 - E_4 \end{aligned} \tag{4.20}$$

Hence,

$$\begin{aligned} CDiffMax &= CMax_2 - CMax_1 = SMax_2 - SMax_1 + (E_2 + E_3) = SDiffMax + (E_2 + E_3) \\ CDiffMin &= CMin_2 - CMin_1 = SMin_2 - SMin_1 + (E_3 - E_4) = SDiffMin + (E_3 - E_4) \end{aligned} \tag{4.21}$$

As a result, unless E_4 is much larger than E_3, the numerical integration process is likely to decrease DiffMax while not affect DiffMin much. A similar analysis can be done for signals that resemble Type 3 lameness.

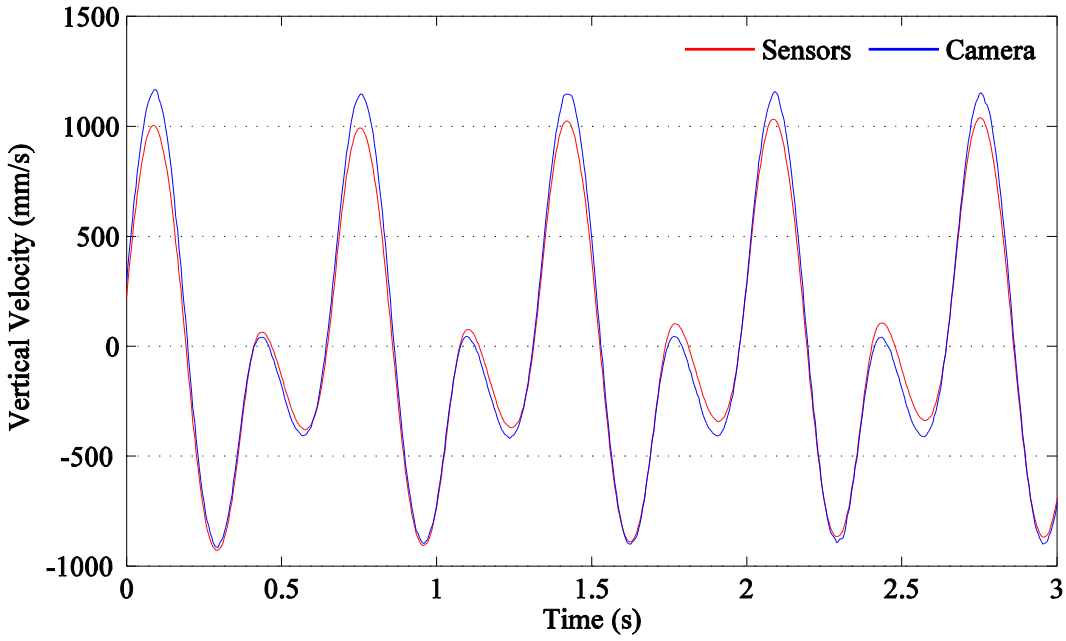

Figure 4.25: Vertical velocity signals from the sensor and the camera under the Type 3 lameness.

A velocity signal that resembles Type 3 lameness is shown in Figure 4.25. In this case, we have

$$\begin{aligned} CMax_1 - SMax_1 &= E_1 \\ CMin_1 - SMin_1 &= E_1 + E_2 \\ CMax_2 - SMax_2 &= E_1 + E_2 - E_3 \\ CMin_2 - CMin_2 &= E_1 + E_2 - E_3 - E_4 \end{aligned} \tag{4.22}$$

Hence,

$$\begin{aligned} CDiffMax &= CMax_2 - CMax_1 = SMax_2 - SMax_1 + (E_2 - E_3) = SDiffMax + (E_2 - E_3) \\ CDiffMin &= CMin_2 - CMin_1 = SMin_2 - SMin_1 + (-E_3 - E_4) = SDiffMin + (-E_3 - E_4) \end{aligned} \tag{4.23}$$

As a result, DiffMin is likely to be overestimated while DiffMax may be quite accurate. For these two different cases, we conclude that two conditioning formulas are needed for two different types of lameness.

4.5. Normal Ranges of Head and Pelvis Rotation Angles

Here we investigate the normal ranges of rotation angles of horses' head and pelvis during trotting. If the rotation angles are large, then we have to use the conditioning algorithms on the sensor output to obtain the true vertical acceleration. On the other hand, if the angles are small, then we do not need to condition the sensor acceleration at all. As explained in Section 4.3.1, first we convert the gyroscope output to angular velocity (degree/s). Then we integrate angular velocity signals once to get the rotation angles. Notice that these rotation angles are assumed to have a zero mean. Numerical results show that the range of rotation angles of real horses is mostly quite small, with an absolute value less than 15 degrees. Figure 4.26, Figure 4.27 and Table C.1 in Appendix C report the head and pelvis rotation angles of 12 different horses during trotting.

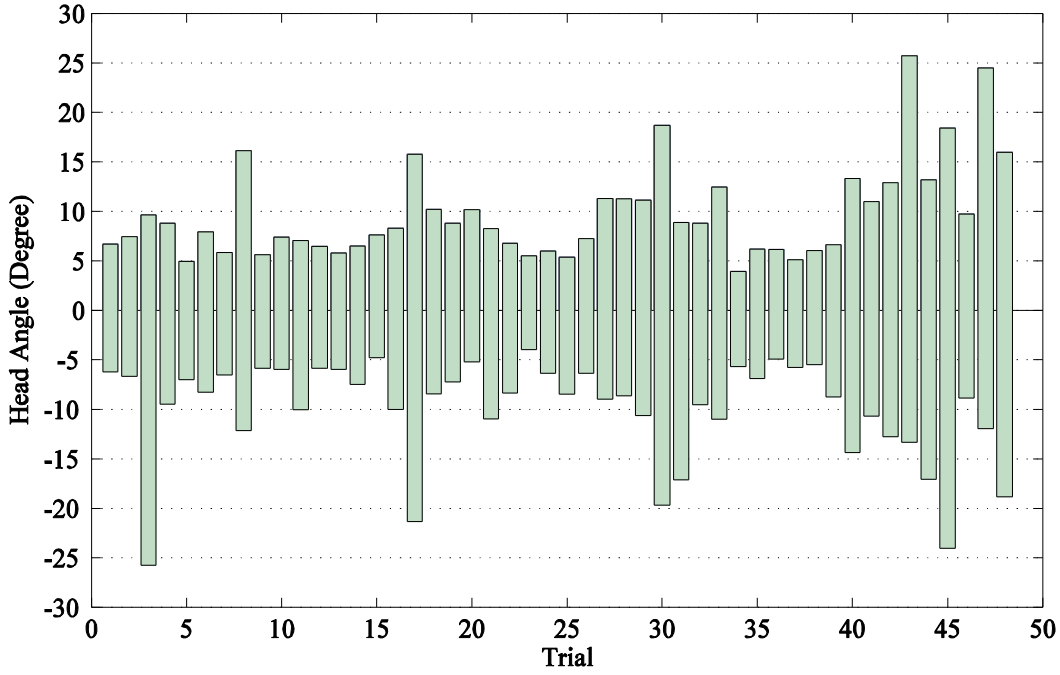

Figure 4.26: Head rotation angle ranges in real trotting horses.

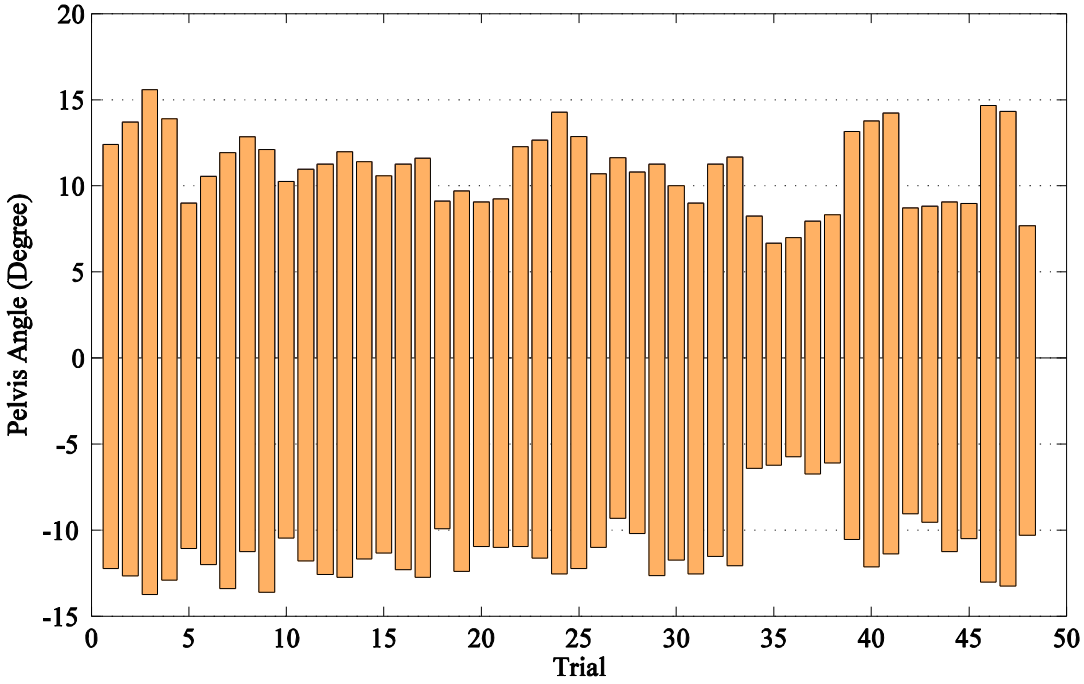

Figure 4.27: Pelvis rotation angle ranges in real trotting horses.

Among these trials, there are a few cases in which rotation angles exceed 15 degrees. For these cases, the conditioning algorithms are needed. Therefore, to make ELL inclusive, we recommend calculating the rotation angles first. If the maximum absolute rotation angle exceeds the threshold value of 15 degrees, then ELL needs to use the conditioning algorithms.

Chapter 5: SUMMARY AND RECOMMENDATIONS

5.1. Summary of Research

This thesis completes two main studies in order to improve the Equine Lameness Locator (ELL). First we evaluate the use of HHT-CPD-end method against the SWT method for decomposing equine head and pelvis position signals. Second, we correct the uniaxial accelerometer's output to account for the rotation movement.

The HHT-CPD-end method is proved to be less accurate than the SWF method for real horse trotting trials. After combining the CPD and HHT methods and integrating it into the ELL program, we evaluate 10 artificial, ideal position signals and 158 real horse trials. Numerical results show that the HHT-CPD-end method is slightly more accurate and precise than the SWF method for the ideal cases, except for cases without lameness. However, the SWF method is more robust, accurate and precise for real horse data. Therefore, we recommend keeping SWF for ELL.

The wireless accelerometer's output does not need to be conditioned for rotation angles between -15 and 15 degrees. However, for rotation angle outside that range, two different conditioning algorithms are needed to correct the acceleration signals for different types of lameness. We perform two tests to verify this. The dual-accelerometer test translates two accelerations up and down at the same time. One accelerometer also rotates during the process while the other does not rotate. After 9 trials, we conclude that for small rotation angles (-15 to 15 degrees), no conditioning is needed. On the other hand, the accelerometer-videogrammetry test uses a single accelerometer and a camera system to

record acceleration of a rotation-translation motion. After comparing the accelerometer data with the camera data from 84 trials, we confirm that two correction algorithms are needed for rotation angle outside the range of -15 to 15 degrees. Eq. (4.18) is recommended for correcting lameness of Type 1 and Type 2 while Eq. (4.19) is recommended for correcting lameness of Type 3 and Type 4.

5.2. Recommendations for Future Work

While the HHT-CPD-end method is less effective than the SWF method, it provides instantaneous frequency and amplitude of a dynamic signal. This information may be useful to evaluate lameness in other gaits rather than trotting, such as cantering or galloping. Therefore, further study is recommended to explore the potential of the HHT-CPD-end method.

The proposed empirical conditioning algorithms are not developed from strict mechanics/physics. The corrected errors are mainly from the numerical integration process. Moreover, the proposed conditioning algorithms have not been tested in real horse data. Hence, applying the conditioning algorithms to process real horse data is suggested. Furthermore, it is necessary to confirm that horses' head and pelvis rotation angle signals usually have zero mean.

Finally, high frequency noise should be removed from the acceleration signals measured by the wireless sensors before they are double integrated for use in the ELL program. For better double integration results, it can be useful to develop an advanced integration method using the curve fitting approach shown in Section 3.2 for differentiation.

REFERENCES:

1. Keegan, K.G., Yonezawa, Y., Pai, P.F., Wilson, D.A., and Kramer, J., "Evaluation of a Sensor-Based System of Motion Analysis for Detection and Quantification of Forelimb and Hind Limb Lameness in Horses," American J. of Veterinary Research 65(5), 665-670, 2004.

2. Equinosis, LLC, Columbia, MO, USA (http://equinosis.com/press-release/lameness-locator-science-making-stride-in-equine-lameness-evaluation).

3. Keegan, K.G., Pai, P.F., Wilson, D.A., and Smith, B.K., "Signal Decomposition Method of Evaluating Head Movement to Measure Induced Forelimb Lameness in Horses Trotting on a Treadmill," Equine Veterinary Journal 33(5), 446-451, 2001.

4. Palmer III, L. R., Orin, D. E., "3D Control of a High-Speed Quadruped Trot," Industrial Robot 33(4), 298-302, 2006.

5. Kelmer, G., Keegan, K.G., Kramer, J., Wilson, D.A., Pai, P.F., and Singh, P., "Computer-Assisted Kinematic Evaluation of Induced Compensatory Movements Resembling Lameness in Horses Trotting on a Treadmill," American J. of Veterinary Research 66(4), 646-655, 2005.

6. Keegan, K.G. and Pai, P.F., "Lameness Evaluation Systems and Methods," US Patent No. 7601126, October 13, 2009.

7. Keegan, K.G., Kramer, J., Yonezawa, Y., Maki, H., Pai, P.F., Dent, E.V., Kellerman, T., Wilson, D.A., and Reed, S., "Assessment of Repeatability of a Wireless, Inertial Sensor-Based Lameness Evaluation System for Horses," American J. of Veterinary Research 72 (9), 1156-1163, 2011.

8. Keegan, K.G., Wilson, D.A., Kramer, J., Reed, S.K., Yonezawa, Y., Maki, H., Pai, P.F., Lopes, M.A.F., "Comparison of a Body-Mounted Inertial Sensor Method to Subjective Evaluation for Detection of Lameness in Horses," American J. of Veterinary Research, accepted.

9. Pai, P.F., "Nonlinear Vibration Characterization by Signal Decomposition," Journal of Sound and Vibration 307, 527-544, 2007.

10. Huang, N.E., Shen, Z., Long, S.R., Wu, M.C., Shih, H.H., Zheng, Q., Yen, N.C., Tung, C.C., and Liu, H.H., "The Empirical Mode Decomposition and the Hilbert Spectrum for Nonlinear and Non-Stationary Time Series Analysis," Proc. R. Soc. Lond. A 454, 903-995, 1998.

11. Huang, N.E., Shen, Z., and Long, S.R., "A New View of Nonlinear Water Waves: The Hilbert Spectrum," Annual Review of Fluid Mechanics 31, 417-457, 1999.

12. Huang, N.E., Wu, M.C., Long, S.R., Shen, S.S.P., Qu, W., Gloersen, P., and Fan, K.L., "A Confidence Limit for the Empirical Mode Decomposition and Hilbert Spectral Analysis," Proc. R. Soc. Lond. A 459, 2317-2345, 2003.

13. Wu, Z. and Huang, N.E., "A Study of the Characteristics of White Noise Using the Empirical Mode Decomposition Method," Proc. R. Soc. Lond. A 460, 1597-1611, 2004.

14. Huang, N.E. and Attoh-Okine, N.O. (editors), The Hilbert-Huang Transform in Engineering, CRC Press, Boca Raton, FL, 2005.

15. Brigham, E.O., The Fast Fourier Transform, Prentice-Hall, Englewood Cliffs, New Jersey, 1974.

16. Daubechies, I., Ten Lectures on Wavelets, CBMS-NSF Lecture Notes 61, SIAM, Philadelphia, 1992.

17. Wu, F. and Qu, L., "An Improved Method for Restraining the End Effect in Empirical Mode Decomposition and Its Applications to the Fault Diagnosis of Large Rotating Machinery," Journal of Sound and Vibration 314, 586-602, 2008.

18. Dätig, M. and Schlurmann, T., "Performance and Limitations of the Hilbert–Huang Transformation (HHT) with an Application to Irregular Water Waves," Ocean Engineering 31, 1783–1834, 2004.

19. Pai, P.F., "Time-Frequency Characterization of Nonlinear Normal Modes and Challenges in Nonlinearity Identification of Dynamical Systems," Mechanical Systems and Signal Processing 25, 2358-2374, 2011.

20. Maragos, P., Kaiser, J.F., and Quatieri, T.F., "Energy Separation in Signal Modulations with Application to Speech Analysis," IEEE Transactions on Signal Processing 41 (10), 3024-3051, 1993.

APPENDIX A: Means and Standard Deviations of DiffMax and DiffMin of Head Movement of Real Trotting Horses

Table A.1: Means and standard deviations of DiffMax and DiffMin of head movement of real trotting horses (108 cases).

SWF Method				HHT with EE Improvement			
Mean DiffMax (mm)	SD DiffMax (mm)	Mean DiffMin (mm)	SD DiffMin (mm)	Mean DiffMax (mm)	SD DiffMax (mm)	Mean DiffMin (mm)	SD DiffMin (mm)
-1.598	4.180	-12.883	6.477	-1.302	5.414	-13.401	6.788
8.689	7.640	-11.817	5.392	9.576	11.136	-11.769	7.168
-9.011	6.073	1.033	8.548	-6.223	21.645	5.130	21.586
9.626	10.262	-8.967	14.034	7.839	28.224	-5.075	26.231
-2.228	10.298	-19.369	8.068	-2.649	11.284	-20.923	8.543
34.232	11.983	64.249	11.333	11.259	39.642	3.727	37.216
-7.294	7.208	4.783	12.399	-7.780	8.442	5.250	14.774
-31.903	10.744	-38.610	13.752	-32.448	11.765	-39.596	14.873
-1.119	7.289	-7.953	7.165	-1.162	11.532	-8.374	11.212
6.280	7.714	-8.867	3.899	6.592	9.790	-8.798	5.490
6.740	15.489	3.640	18.076	6.724	19.045	3.301	20.523
2.205	12.003	8.948	6.682	0.364	23.633	10.308	15.627
-4.741	6.571	-0.485	16.081	-5.123	8.968	-0.385	18.304
-4.491	7.833	-1.994	22.084	-5.598	10.081	-2.442	26.128
18.056	9.847	9.857	5.078	18.671	9.603	9.967	5.484
22.029	27.183	1.126	23.363	10.155	71.807	-0.832	53.060
48.252	11.397	93.935	14.202	5.038	29.201	-18.075	22.329
13.433	13.267	-2.743	20.290	-3.957	20.998	-1.293	18.816
7.271	19.227	3.854	15.322	7.976	23.144	4.224	20.771
-38.455	10.545	-3.693	10.735	-39.220	10.755	-3.856	11.555
-7.464	4.504	1.877	7.261	-7.757	5.661	1.611	8.591
3.975	11.785	-6.618	12.474	2.568	12.640	-5.726	9.970
0.556	12.215	9.462	12.497	2.113	20.335	9.175	43.653
-0.587	4.451	-8.712	6.570	-0.704	6.769	-8.784	8.195

Table A.1: (continued)

SWF Method				HHT With EE Improvement			
Mean DiffMax (mm)	SD DiffMax (mm)	Mean DiffMin (mm)	SD DiffMin (mm)	Mean DiffMax (mm)	SD DiffMax (mm)	Mean DiffMin (mm)	SD DiffMin (mm)
11.401	9.234	8.702	12.099	11.574	10.018	9.348	13.217
-9.448	7.278	4.617	7.773	-9.423	9.063	4.862	10.203
7.830	25.334	-3.134	16.197	10.128	38.284	0.315	32.517
12.332	16.903	-2.330	16.609	13.738	22.497	-1.338	25.179
-6.201	7.930	12.410	23.235	-8.711	31.334	13.094	34.077
44.464	10.971	85.141	11.311	11.533	38.105	-30.123	19.301
-6.294	26.049	-18.967	41.170	-1.610	57.062	-5.260	69.494
-3.546	6.189	3.591	8.004	-3.584	10.396	4.058	11.627
1.141	14.990	26.957	13.288	-4.984	14.525	2.535	29.498
9.243	17.925	-8.293	13.521	10.069	22.331	-7.949	20.113
2.294	7.728	7.200	8.667	1.830	12.104	6.519	14.513
2.945	10.047	10.787	9.605	1.582	21.010	12.083	13.834
-6.650	8.526	-8.003	8.515	-4.766	15.463	-7.055	18.492
-3.444	10.730	-3.173	10.561	-3.872	12.389	-2.959	12.085
-11.727	7.554	8.008	7.267	-13.290	11.744	7.629	12.397
9.308	10.150	0.371	8.855	9.551	12.176	0.514	10.704
10.789	11.383	8.753	5.574	11.134	14.244	9.403	8.593
-7.888	10.862	1.837	16.635	-8.836	14.912	0.573	19.086
2.907	8.798	-12.883	12.955	2.624	15.773	-13.626	32.479
-28.328	13.583	-43.814	18.294	-6.820	53.748	1.134	47.649
-1.936	6.297	-0.502	11.133	-5.693	15.614	-1.104	18.881
17.166	12.842	-4.524	15.313	11.812	24.198	-0.470	20.414
5.983	5.896	6.229	11.948	6.987	11.135	6.896	13.382
0.020	11.139	-18.450	11.880	0.051	12.967	-18.892	14.285
-2.453	5.377	-7.577	5.731	-2.317	10.749	-8.133	13.285

Table A.1: (continued)

SWF Method				HHT With EE Improvement			
Mean DiffMax (mm)	SD DiffMax (mm)	Mean DiffMin (mm)	SD DiffMin (mm)	Mean DiffMax (mm)	SD DiffMax (mm)	Mean DiffMin (mm)	SD DiffMin (mm)
16.028	14.134	-7.448	8.568	15.699	17.270	-8.181	10.630
119.079	11.252	186.503	16.002	18.395	27.386	20.290	26.624
0.513	11.472	3.082	9.127	0.312	14.889	2.907	14.328
17.354	10.271	4.157	11.905	18.165	13.660	4.707	14.232
8.895	8.868	-10.975	6.119	9.422	16.163	-11.642	12.350
6.466	12.702	-14.600	9.346	6.731	18.554	-14.947	13.540
3.828	16.016	2.754	9.014	6.188	22.456	3.731	17.605
1.032	4.075	-19.618	4.156	0.795	4.975	-20.799	4.327
22.728	17.774	1.056	16.631	23.044	18.386	1.077	18.907
-3.571	5.469	-5.091	7.428	-4.344	7.701	-6.079	10.148
-1.011	4.773	-12.803	4.612	-0.259	5.484	-13.943	11.164
-1.979	7.175	-17.985	6.280	-1.436	8.852	-19.249	7.658
17.631	8.003	4.083	8.771	18.129	8.676	4.571	9.456
3.422	12.415	-4.559	11.166	1.181	13.626	-3.474	13.673
-3.196	10.110	4.222	18.097	-3.963	13.416	4.524	21.382
7.418	5.997	16.494	5.925	7.823	8.793	16.887	8.997
20.319	11.407	40.597	18.860	-2.778	23.902	-19.401	27.321
6.560	18.192	-13.166	12.336	6.819	21.303	-16.759	20.897
21.105	13.737	2.401	13.153	21.506	19.607	2.329	19.273
-4.296	4.217	7.996	10.801	-5.106	5.344	8.586	12.168
0.086	17.163	17.062	25.057	5.484	15.784	18.942	30.008
15.290	18.749	23.280	18.792	-8.977	27.998	-8.728	30.274
-6.036	9.530	3.194	13.426	-6.911	16.299	3.955	16.516
4.185	5.721	7.666	3.266	4.235	6.142	8.041	3.589
1.057	7.317	7.759	5.320	1.272	11.120	8.519	9.692

Table A.1: (continued)

SWF Method				HHT With EE Improvement			
Mean DiffMax (mm)	SD DiffMax (mm)	Mean DiffMin (mm)	SD DiffMin (mm)	Mean DiffMax (mm)	SD DiffMax (mm)	Mean DiffMin (mm)	SD DiffMin (mm)
-19.000	8.644	-19.135	10.867	-19.555	13.898	-19.903	14.512
5.454	11.130	-3.233	10.952	10.316	33.523	1.486	43.802
7.197	6.175	-8.937	8.524	7.836	8.374	-9.306	12.090
-36.991	10.228	-22.837	15.556	-25.266	29.819	-13.245	25.875
-4.269	11.219	5.364	9.923	-4.967	13.751	5.334	11.935
-3.767	6.234	1.280	7.321	-3.823	8.153	0.782	9.579
0.555	7.533	-12.299	10.299	0.998	11.384	-12.807	12.274
-4.755	6.094	6.597	7.308	-4.921	5.893	6.890	6.793
-21.392	6.820	-24.934	10.851	-19.935	8.181	-22.018	11.158
-2.498	10.579	1.116	17.010	-2.746	14.201	0.172	21.493
-40.296	11.436	-16.793	11.765	-41.864	11.858	-17.944	13.389
2.934	10.619	0.781	8.534	4.378	11.440	1.022	11.043
-10.083	7.579	-18.853	10.686	-10.257	10.874	-19.793	12.597
-3.211	6.355	-10.431	8.690	-3.435	8.583	-11.010	9.515
4.919	6.600	5.538	6.695	5.101	8.201	5.781	7.855
10.154	6.785	8.239	6.957	10.212	7.853	8.588	7.385
5.889	9.198	3.393	5.706	5.818	10.400	3.422	7.578
9.707	8.865	8.289	7.267	10.172	8.970	9.067	7.819
28.644	12.842	-1.762	10.482	32.860	22.325	-0.309	14.619
-5.928	4.806	-11.437	7.875	-6.232	11.077	-12.611	13.063
13.854	19.681	9.530	7.285	15.130	23.349	11.303	12.293
-3.145	6.314	-18.242	7.285	-3.458	6.497	-19.881	7.190
-5.467	9.816	-14.376	14.518	-5.809	16.160	-15.006	19.382
12.778	14.738	11.884	10.577	13.098	19.418	13.287	12.679
-3.339	9.857	-1.371	11.981	-3.440	13.099	-2.300	15.241

Table A.1: (continued)

SWF Method				HHT With EE Improvement			
Mean DiffMax (mm)	SD DiffMax (mm)	Mean DiffMin (mm)	SD DiffMin (mm)	Mean DiffMax (mm)	SD DiffMax (mm)	Mean DiffMin (mm)	SD DiffMin (mm)
0.447	7.113	-16.291	7.735	1.763	12.919	-15.498	16.234
-3.043	8.220	-15.553	11.367	-3.554	13.498	-17.158	14.760
2.611	5.242	-18.788	5.046	3.025	4.975	-19.854	6.078
11.399	31.563	-1.707	37.602	18.950	96.381	-7.799	95.805
55.419	8.549	27.937	6.290	-4.070	42.011	-7.105	19.578
42.761	8.217	18.690	9.353	40.842	7.886	14.583	13.246
6.376	8.093	17.710	8.382	6.916	16.064	17.963	17.980
4.625	11.886	-0.386	10.041	5.337	15.305	0.064	13.834

Table A.2: Means and standard deviations of DiffMax and DiffMin of pelvis movement of real trotting horses (108 cases).

SWF Method				HHT With EE Improvement			
Mean DiffMax (mm)	SD DiffMax (mm)	Mean DiffMin (mm)	SD DiffMin (mm)	Mean DiffMax (mm)	SD DiffMax (mm)	Mean DiffMin (mm)	SD DiffMin (mm)
-3.374	3.774	3.905	4.649	-3.054	4.658	4.667	5.361
0.800	4.120	-4.764	1.508	1.654	2.304	-5.853	1.949
-5.256	5.755	-1.488	4.590	-2.781	3.642	-0.401	5.616
0.900	5.172	8.557	4.792	-0.827	6.323	-8.861	5.502
-0.774	3.301	0.023	2.564	-0.515	4.115	0.822	3.292
-4.315	3.413	-3.226	4.561	2.903	3.516	4.555	5.139
7.837	4.551	7.930	2.952	8.817	4.455	8.569	2.860
10.933	5.680	-2.556	5.689	-11.331	5.832	2.077	5.948
-3.236	3.602	8.069	3.518	-3.223	3.511	7.573	3.569
-1.374	2.281	2.813	3.327	-2.548	2.371	4.490	5.513
4.451	4.666	7.081	4.892	-2.393	6.672	-4.079	8.786
-1.090	4.402	2.884	6.538	1.314	3.633	2.806	6.667
-4.043	4.026	-0.459	4.406	-3.321	5.163	-0.735	4.810
-3.266	3.445	-16.041	2.656	-2.899	0.731	-18.594	3.001
-8.861	8.249	-8.542	7.836	-6.191	8.883	-8.426	8.610
7.947	8.600	3.276	6.741	7.897	9.725	2.979	7.912
-12.978	6.543	4.132	7.471	-13.950	6.995	6.034	5.308
3.793	5.592	5.938	4.858	3.812	6.059	6.126	5.360
-0.446	6.613	9.037	6.929	0.221	7.892	-9.021	6.304
3.472	4.618	-2.185	4.294	-3.812	6.226	1.275	5.024
-5.118	3.748	2.989	3.470	5.857	4.378	-3.083	4.604
-15.376	4.819	-12.819	6.002	-15.641	4.650	-12.997	6.207
-1.387	3.619	-11.181	3.836	0.912	4.984	15.521	2.233
-14.463	3.004	5.900	2.487	-14.997	3.370	6.772	3.344
0.636	4.273	4.175	2.843	1.691	4.030	3.422	2.733

Table A.2: (continued)

SWF Method				HHT With EE Improvement			
Mean DiffMax (mm)	SD DiffMax (mm)	Mean DiffMin (mm)	SD DiffMin (mm)	Mean DiffMax (mm)	SD DiffMax (mm)	Mean DiffMin (mm)	SD DiffMin (mm)
7.505	3.822	6.897	4.766	8.485	3.476	8.711	3.300
-12.292	9.584	7.955	11.951	12.045	10.086	-7.399	12.150
0.564	5.913	4.654	5.579	-2.229	5.692	-3.491	7.232
1.800	4.934	-8.078	3.627	2.064	3.966	-8.237	3.057
-13.609	5.622	-0.920	5.028	-15.552	3.094	-2.454	5.218
6.279	7.356	-9.305	10.110	-6.118	8.551	9.217	11.210
-3.885	3.725	-1.290	4.421	-3.368	4.748	-0.420	5.283
-1.563	5.111	-4.113	5.109	2.353	4.048	6.299	4.641
15.583	8.902	0.620	10.742	6.881	17.158	3.489	10.809
0.849	7.996	15.472	6.418	1.491	8.563	15.805	7.134
-2.745	4.601	-2.967	4.679	5.437	7.567	5.030	6.754
-0.035	3.972	-1.887	3.287	-0.203	4.425	-1.974	2.726
-1.483	5.288	-1.587	5.910	-0.537	6.800	2.213	4.518
7.209	4.153	9.088	3.482	-7.351	5.118	-10.157	4.073
-3.594	3.834	-0.461	3.287	-3.998	3.813	-0.906	3.713
4.309	8.150	3.950	4.304	6.917	5.687	4.328	5.478
-5.488	5.049	-2.334	3.149	5.771	4.474	2.649	3.334
7.547	2.925	-8.818	5.491	8.225	2.900	-11.328	7.218
12.306	4.549	-9.316	7.471	13.210	3.329	-11.272	8.147
1.266	4.057	-10.615	4.552	5.145	1.281	-6.401	2.788
2.377	6.462	20.513	4.778	-1.089	7.847	-17.048	14.675
2.695	4.259	-0.132	5.349	1.246	3.482	-2.279	6.454
-1.989	3.779	-1.480	4.902	4.177	4.553	0.147	5.758
5.895	4.517	13.260	6.128	13.418	0.579	21.321	0.417
-22.252	6.791	-15.304	5.405	-22.825	6.748	-15.343	5.611

Table A.2: (continued)

SWF Method				HHT With EE Improvement			
Mean DiffMax (mm)	SD DiffMax (mm)	Mean DiffMin (mm)	SD DiffMin (mm)	Mean DiffMax (mm)	SD DiffMax (mm)	Mean DiffMin (mm)	SD DiffMin (mm)
-22.489	4.846	-0.827	4.794	-22.291	4.269	-1.377	5.626
1.373	6.134	-0.851	8.469	6.202	44.943	7.869	53.213
0.260	3.106	3.691	5.137	0.427	4.491	1.257	6.796
4.267	1.860	4.681	3.050	4.639	1.067	4.968	2.761
-3.248	4.935	-11.281	3.193	2.768	6.284	-1.232	12.722
2.437	8.493	1.672	8.788	-2.778	5.052	-3.697	12.532
-1.684	3.060	-1.759	3.116	-2.435	4.446	-2.816	3.501
-12.271	7.109	1.998	4.524	12.354	7.630	-2.297	5.744
-2.807	4.591	5.017	2.858	-1.574	8.183	4.631	6.133
-0.463	2.924	4.812	4.156	-0.507	5.493	5.815	6.574
3.168	2.612	5.919	1.869	3.632	3.042	6.659	2.604
-17.200	4.187	-10.786	3.474	-4.153	18.603	-1.817	11.087
0.335	7.651	3.385	6.537	1.680	8.494	1.368	8.203
1.277	2.500	-7.912	3.201	-1.412	2.959	3.618	8.374
-4.444	4.007	0.819	3.773	-3.618	3.153	0.553	4.403
-2.287	3.743	-2.460	5.649	-2.149	4.693	-3.236	7.285
5.814	7.650	9.310	4.166	4.664	10.469	8.231	5.600
-17.587	7.851	12.409	7.575	-17.307	8.093	13.324	6.999
-5.497	2.666	-0.292	4.470	5.473	2.611	0.709	6.697
0.864	7.235	-5.078	4.868	-4.765	5.177	-10.387	3.572
-5.818	6.655	0.834	6.361	-6.187	8.358	1.434	7.166
4.498	7.337	7.556	8.419	3.823	12.102	-8.663	9.600
-7.456	3.323	-7.452	2.900	-6.530	3.772	-8.095	3.151
-7.692	2.850	-0.991	3.746	-9.372	4.018	-2.760	4.432
-5.226	7.651	-15.441	6.676	-4.553	12.568	-15.617	9.058

Table A.2: (continued)

SWF Method				HHT With EE Improvement			
Mean DiffMax (mm)	SD DiffMax (mm)	Mean DiffMin (mm)	SD DiffMin (mm)	Mean DiffMax (mm)	SD DiffMax (mm)	Mean DiffMin (mm)	SD DiffMin (mm)
5.518	2.842	-10.818	4.388	7.209	3.604	-11.913	4.190
3.703	3.329	3.672	3.232	2.559	2.884	3.475	1.701
5.748	4.806	0.178	5.968	-5.729	5.224	-0.233	6.406
1.997	5.572	0.889	5.331	0.619	7.358	1.638	5.505
0.236	3.856	1.635	3.464	-1.427	3.235	2.448	4.111
2.155	4.061	5.242	2.797	2.219	4.566	5.476	2.598
-5.150	2.639	-3.318	3.526	4.351	3.256	4.910	4.100
-1.481	3.957	4.486	2.625	3.998	3.545	-6.028	2.722
1.745	5.288	-4.206	4.550	0.302	6.997	-0.033	6.049
9.209	6.270	-2.181	7.929	-9.393	6.967	1.808	8.899
7.642	9.629	9.676	6.417	8.564	8.002	13.542	5.576
-6.330	3.727	13.042	4.754	-6.334	4.812	13.609	5.067
-0.554	3.780	6.395	3.665	-1.047	4.204	1.827	6.947
-5.952	3.430	-6.686	3.801	-1.341	6.919	0.748	7.849
-6.813	2.547	-9.296	2.544	-7.573	2.669	-9.106	2.885
-5.173	4.742	-6.666	3.558	-4.545	5.166	-7.742	3.334
15.552	4.523	12.715	5.922	16.883	5.079	15.263	6.217
-2.023	2.815	7.668	5.862	-2.662	5.342	13.254	2.413
-5.606	4.667	4.907	3.450	-5.096	5.545	4.702	6.251
-1.871	4.737	6.706	6.672	7.756	0.000	2.335	0.000
-12.520	4.472	5.696	2.508	-12.671	4.303	5.836	1.842
1.077	5.367	7.559	4.353	-1.456	6.077	-2.729	9.058
6.100	4.427	11.344	3.721	7.174	5.132	13.579	3.466
6.114	5.862	-2.182	4.656	6.368	6.575	-3.517	4.476
-0.940	3.309	-3.487	2.456	-0.741	3.437	-3.686	2.202

Table A.2: (continued)

SWF Method				HHT With EE Improvement			
Mean DiffMax (mm)	SD DiffMax (mm)	Mean DiffMin (mm)	SD DiffMin (mm)	Mean DiffMax (mm)	SD DiffMax (mm)	Mean DiffMin (mm)	SD DiffMin (mm)
2.484	4.149	6.266	4.310	2.208	4.750	7.097	6.812
5.845	4.017	5.801	1.857	5.712	3.224	6.108	1.848
3.357	5.814	2.050	11.608	3.345	8.683	-3.156	12.388
-18.926	3.663	-12.239	3.741	18.537	3.581	13.561	3.894
-22.520	7.538	-3.864	8.733	8.101	22.891	3.029	8.553
-18.839	5.548	1.672	5.712	-18.719	5.208	1.533	6.050
-1.304	4.459	3.152	5.027	1.672	4.342	-2.755	5.255

Table A.3: Means and standard deviations of DiffMax and DiffMin of head movement of real trotting horses (107 cases).

SWF Method				HHT With ISBM Improvement			
Mean DiffMax (mm)	SD DiffMax (mm)	Mean DiffMin (mm)	SD DiffMin (mm)	Mean DiffMax (mm)	SD DiffMax (mm)	Mean DiffMin (mm)	SD DiffMin (mm)
-1.598	4.180	-12.883	6.477	-1.412	5.306	-13.664	6.696
8.689	7.640	-11.817	5.392	8.639	8.770	-12.198	6.226
-9.011	6.073	1.033	8.548	-12.759	10.134	0.800	14.238
-2.228	10.298	-19.369	8.068	-2.487	11.534	-20.877	8.296
34.232	11.983	64.249	11.333	10.060	34.400	5.736	40.548
-7.294	7.208	4.783	12.399	-7.807	8.177	5.167	14.335
-1.119	7.289	-7.953	7.165	-1.256	11.603	-8.286	11.176
6.280	7.714	-8.867	3.899	7.179	10.493	-9.159	5.127
2.205	12.003	8.948	6.682	-0.193	24.909	10.327	15.467
-4.741	6.571	-0.485	16.081	-5.137	9.649	-0.486	18.670
-4.491	7.833	-1.994	22.084	-6.000	9.508	-2.336	25.717
18.056	9.847	9.857	5.078	18.634	9.577	10.323	5.331
48.252	11.397	93.935	14.202	7.220	29.365	-11.537	16.753
13.433	13.267	-2.743	20.290	-3.983	20.969	-1.302	18.785
7.271	19.227	3.854	15.322	7.856	23.243	4.233	20.863
-38.455	10.545	-3.693	10.735	-39.153	10.794	-3.858	11.584
-7.464	4.504	1.877	7.261	-7.939	5.238	1.752	8.630
0.556	12.215	9.462	12.497	2.331	24.110	11.106	44.389
-0.587	4.451	-8.712	6.570	-0.207	7.489	-8.543	7.870
-4.715	10.634	-5.614	11.386	-4.500	21.394	-5.430	22.796
7.349	6.943	-1.773	7.766	8.625	9.930	-1.736	11.568
11.401	9.234	8.702	12.099	11.698	9.950	9.300	13.365
-9.448	7.278	4.617	7.773	-9.636	8.810	4.513	10.594
12.332	16.903	-2.330	16.609	12.613	21.023	-2.525	22.055
-6.201	7.930	12.410	23.235	-8.614	33.597	12.932	35.726

Table A.3: (continued)

SWF Method				HHT With ISBM Improvement			
Mean DiffMax (mm)	SD DiffMax (mm)	Mean DiffMin (mm)	SD DiffMin (mm)	Mean DiffMax (mm)	SD DiffMax (mm)	Mean DiffMin (mm)	SD DiffMin (mm)
44.464	10.971	85.141	11.311	11.818	37.699	-30.212	19.095
-3.546	6.189	3.591	8.004	-3.564	10.383	4.175	11.337
1.141	14.990	26.957	13.288	-6.786	13.569	1.846	28.438
9.243	17.925	-8.293	13.521	9.493	24.034	-8.569	21.627
2.945	10.047	10.787	9.605	2.573	18.819	13.205	15.065
-1.221	8.189	-13.824	4.366	-6.487	19.342	-22.289	27.252
5.302	8.510	5.481	16.704	6.339	10.230	5.295	20.120
-2.403	9.469	1.510	27.941	-2.293	16.377	1.275	32.477
-120.281	19.886	-180.175	7.715	-2.991	18.625	11.308	24.510
-11.727	7.554	8.008	7.267	-12.947	10.901	7.868	11.130
9.308	10.150	0.371	8.855	10.263	13.148	1.542	11.560
10.789	11.383	8.753	5.574	11.193	14.378	9.342	8.649
-7.888	10.862	1.837	16.635	-10.387	33.785	5.614	38.569
2.907	8.798	-12.883	12.955	3.045	15.505	-13.652	33.188
-1.936	6.297	-0.502	11.133	-4.790	14.952	-1.450	18.383
17.166	12.842	-4.524	15.313	12.050	24.240	-0.687	20.786
5.983	5.896	6.229	11.948	7.245	11.033	6.969	12.478
-7.430	7.466	4.956	6.155	-7.861	11.714	5.625	9.580
0.020	11.139	-18.450	11.880	0.133	13.091	-19.072	14.112
11.204	12.270	4.367	18.307	23.613	56.972	13.810	66.002
-2.453	5.377	-7.577	5.731	-2.610	10.524	-8.477	13.254
1.179	9.744	-0.284	10.387	1.118	14.406	-0.488	14.710
-3.092	4.607	1.681	6.266	-4.232	7.692	2.335	16.599
119.079	11.252	186.503	16.002	30.044	43.614	31.506	52.811
17.354	10.271	4.157	11.905	18.086	11.475	4.473	13.374

Table A.3: (continued)

SWF Method				HHT With ISBM Improvement			
Mean DiffMax (mm)	SD DiffMax (mm)	Mean DiffMin (mm)	SD DiffMin (mm)	Mean DiffMax (mm)	SD DiffMax (mm)	Mean DiffMin (mm)	SD DiffMin (mm)
8.895	8.868	-10.975	6.119	9.266	15.607	-11.679	11.290
6.466	12.702	-14.600	9.346	6.661	18.967	-14.934	13.733
3.828	16.016	2.754	9.014	6.341	22.428	4.150	18.031
5.075	14.453	-4.036	14.770	1.731	89.829	-4.262	114.184
-1.809	11.347	-1.491	6.307	-1.634	13.992	-1.826	9.369
-3.571	5.469	-5.091	7.428	-4.268	7.522	-6.082	9.969
-1.011	4.773	-12.803	4.612	-0.145	5.444	-13.915	10.795
-1.979	7.175	-17.985	6.280	-1.647	9.354	-19.584	8.230
17.631	8.003	4.083	8.771	18.053	8.648	4.535	9.470
-5.077	11.548	8.110	11.058	-4.992	14.012	9.140	12.504
0.489	8.801	18.353	11.756	0.478	12.991	19.212	15.435
-5.457	8.338	-0.297	13.885	7.555	7.240	14.864	3.587
-3.196	10.110	4.222	18.097	-3.855	13.746	4.453	21.311
7.418	5.997	16.494	5.925	7.823	8.718	17.016	8.819
20.319	11.407	40.597	18.860	-2.807	23.748	-19.469	27.377
5.142	12.114	4.529	11.163	5.628	22.412	4.819	21.150
6.560	18.192	-13.166	12.336	6.671	21.796	-16.166	22.288
-4.296	4.217	7.996	10.801	-5.462	5.232	8.266	12.758
0.086	17.163	17.062	25.057	6.492	27.306	25.656	35.255
15.290	18.749	23.280	18.792	15.874	25.177	20.190	24.991
-6.036	9.530	3.194	13.426	-5.471	19.500	3.989	16.524
4.185	5.721	7.666	3.266	4.315	6.285	8.063	3.548
1.057	7.317	7.759	5.320	1.484	11.133	8.666	9.985
5.454	11.130	-3.233	10.952	9.904	36.094	5.146	44.277
7.197	6.175	-8.937	8.524	8.258	14.370	-8.913	17.334

Table A.3: (continued)

SWF Method				HHT With ISBM Improvement			
Mean DiffMax (mm)	SD DiffMax (mm)	Mean DiffMin (mm)	SD DiffMin (mm)	Mean DiffMax (mm)	SD DiffMax (mm)	Mean DiffMin (mm)	SD DiffMin (mm)
-36.991	10.228	-22.837	15.556	-25.235	29.862	-13.268	25.861
-4.269	11.219	5.364	9.923	-3.807	15.771	6.147	13.701
-3.767	6.234	1.280	7.321	-3.956	8.143	0.689	9.583
-4.382	18.436	-32.984	31.849	1.043	23.577	-4.853	52.331
0.555	7.533	-12.299	10.299	1.252	10.341	-12.426	12.388
-4.755	6.094	6.597	7.308	-4.980	5.503	6.433	7.510
-21.392	6.820	-24.934	10.851	-19.843	8.370	-22.360	11.496
-2.498	10.579	1.116	17.010	-2.723	14.271	0.234	21.367
-40.296	11.436	-16.793	11.765	-41.938	11.906	-18.001	13.251
2.934	10.619	0.781	8.534	4.051	12.401	0.299	12.781
-5.948	16.341	-55.566	13.828	-13.828	25.696	-7.330	61.070
-10.083	7.579	-18.853	10.686	-10.346	10.525	-19.785	12.577
-3.211	6.355	-10.431	8.690	-3.500	7.849	-11.024	9.428
4.919	6.600	5.538	6.695	4.891	8.442	5.531	8.156
10.154	6.785	8.239	6.957	10.229	7.800	8.576	7.458
1.193	6.286	-18.370	6.242	0.971	7.899	-20.168	6.459
9.707	8.865	8.289	7.267	10.136	9.217	9.010	8.087
28.644	12.842	-1.762	10.482	32.984	22.349	-0.278	14.734
-5.928	4.806	-11.437	7.875	-6.324	11.798	-12.602	13.489
13.854	19.681	9.530	7.285	14.032	21.602	11.822	13.358
-3.145	6.314	-18.242	7.285	-3.454	6.530	-19.816	7.134
-5.467	9.816	-14.376	14.518	-7.082	13.895	-16.402	25.366
12.778	14.738	11.884	10.577	12.799	18.989	13.059	13.123
-3.339	9.857	-1.371	11.981	-3.627	13.911	-2.890	17.118
0.447	7.113	-16.291	7.735	0.634	11.334	-17.035	12.372

Table A.3: (continued)

SWF Method				HHT With ISBM Improvement			
Mean DiffMax (mm)	SD DiffMax (mm)	Mean DiffMin (mm)	SD DiffMin (mm)	Mean DiffMax (mm)	SD DiffMax (mm)	Mean DiffMin (mm)	SD DiffMin (mm)
-3.043	8.220	-15.553	11.367	-3.607	13.636	-17.294	14.564
2.611	5.242	-18.788	5.046	2.986	5.146	-20.269	5.209
55.419	8.549	27.937	6.290	0.365	39.320	-6.217	18.870
42.761	8.217	18.690	9.353	40.853	8.391	14.589	12.811
-8.286	7.473	-18.042	8.045	-8.779	9.279	-19.429	9.647
-15.845	32.765	-33.861	44.571	0.581	79.104	-11.002	68.394
4.625	11.886	-0.386	10.041	5.426	14.986	0.246	13.377

Table A.4: Means and standard deviations of DiffMax and DiffMin of pelvis movement of real trotting horses (107 cases).

SWF Method				HHT With ISBM Improvement			
Mean DiffMax (mm)	SD DiffMax (mm)	Mean DiffMin (mm)	SD DiffMin (mm)	Mean DiffMax (mm)	SD DiffMax (mm)	Mean DiffMin (mm)	SD DiffMin (mm)
-3.374	3.774	3.905	4.649	-3.923	4.241	4.645	4.975
0.800	4.120	-4.764	1.508	0.468	7.181	-4.743	3.255
-5.256	5.755	-1.488	4.590	-5.526	6.556	-1.189	4.870
-0.774	3.301	0.023	2.564	-0.636	3.658	0.532	3.007
-4.315	3.413	-3.226	4.561	-4.640	4.453	-3.506	5.823
7.837	4.551	7.930	2.952	8.242	4.733	7.720	3.438
-3.236	3.602	8.069	3.518	-3.268	3.659	8.482	3.506
-1.374	2.281	2.813	3.327	-1.775	3.428	3.198	5.250
-1.090	4.402	2.884	6.538	-0.932	6.982	1.231	6.736
-4.043	4.026	-0.459	4.406	-4.116	4.874	-0.172	4.551
-3.266	3.445	-16.041	2.656	-4.490	2.997	-17.263	2.884
-8.861	8.249	-8.542	7.836	-7.666	8.683	-9.512	7.089
-12.978	6.543	4.132	7.471	-13.135	6.404	4.093	7.863
3.793	5.592	5.938	4.858	3.827	6.043	6.039	5.338
-0.446	6.613	9.037	6.929	-0.335	7.214	9.182	7.043
3.472	4.618	-2.185	4.294	3.716	4.964	-2.371	4.863
-5.118	3.748	2.989	3.470	-5.317	3.856	3.247	3.984
-1.387	3.619	-11.181	3.836	-1.687	4.026	-12.819	4.207
-14.463	3.004	5.900	2.487	-14.907	3.749	6.297	3.292
6.072	6.718	4.207	7.162	6.692	8.360	4.321	9.809
2.828	5.775	5.978	6.610	3.724	6.253	6.753	6.420
0.636	4.273	4.175	2.843	0.728	4.786	4.468	3.079
7.505	3.822	6.897	4.766	7.896	3.714	7.182	4.849
0.564	5.913	4.654	5.579	0.655	7.198	5.057	6.556
1.800	4.934	-8.078	3.627	1.947	4.947	-8.445	3.642

Table A.4: (continued)

SWF Method				HHT With ISBM Improvement			
Mean DiffMax (mm)	SD DiffMax (mm)	Mean DiffMin (mm)	SD DiffMin (mm)	Mean DiffMax (mm)	SD DiffMax (mm)	Mean DiffMin (mm)	SD DiffMin (mm)
-13.609	5.622	-0.920	5.028	-14.722	4.586	-1.243	5.760
-3.885	3.725	-1.290	4.421	-3.717	4.738	-1.011	5.055
-1.563	5.111	-4.113	5.109	-1.617	4.817	-4.464	5.489
15.583	8.902	0.620	10.742	15.763	9.405	0.824	11.596
-2.745	4.601	-2.967	4.679	-2.557	4.969	-2.253	5.688
-11.939	5.122	-15.111	6.064	-14.393	6.373	-17.226	7.303
3.912	3.746	-9.485	5.770	4.476	4.667	-9.945	6.819
4.395	5.119	-9.308	3.314	5.182	5.360	-9.915	3.780
-1.243	19.972	18.660	15.010	-10.350	14.197	7.116	13.921
7.209	4.153	9.088	3.482	7.389	4.785	9.531	3.501
-3.594	3.834	-0.461	3.287	-3.938	4.154	-0.437	3.841
4.309	8.150	3.950	4.304	4.943	7.727	4.264	4.591
-5.488	5.049	-2.334	3.149	-5.358	5.180	-2.439	4.103
7.547	2.925	-8.818	5.491	8.497	2.387	-9.584	6.220
1.266	4.057	-10.615	4.552	1.493	5.349	-12.006	5.406
2.377	6.462	20.513	4.778	2.462	7.245	21.520	4.866
2.695	4.259	-0.132	5.349	2.901	6.204	-0.159	7.333
8.833	4.970	3.509	4.184	10.054	5.597	3.746	4.787
-1.989	3.779	-1.480	4.902	-1.851	5.181	-1.298	5.816
6.498	3.217	-8.759	4.689	7.406	3.622	-9.468	4.708
5.895	4.517	13.260	6.128	6.867	5.292	14.963	6.803
1.983	7.557	-7.792	8.280	2.039	9.786	-7.703	10.952
-2.976	4.304	0.524	5.283	-3.618	5.950	2.675	6.929
-22.489	4.846	-0.827	4.794	-23.526	4.928	-1.222	5.473
0.260	3.106	3.691	5.137	0.176	4.311	3.973	5.527

Table A.4: (continued)

SWF Method				HHT With ISBM Improvement			
Mean DiffMax (mm)	SD DiffMax (mm)	Mean DiffMin (mm)	SD DiffMin (mm)	Mean DiffMax (mm)	SD DiffMax (mm)	Mean DiffMin (mm)	SD DiffMin (mm)
4.267	1.860	4.681	3.050	4.450	1.689	4.990	3.593
-3.248	4.935	-11.281	3.193	-3.378	5.416	-11.831	3.121
2.437	8.493	1.672	8.788	2.352	9.939	1.280	9.949
2.553	3.558	-3.825	3.151	2.356	3.799	-3.625	3.555
-9.713	9.490	-19.091	12.366	-11.646	12.509	-22.409	11.696
-2.807	4.591	5.017	2.858	-2.886	5.617	5.670	4.106
-0.463	2.924	4.812	4.156	-0.295	4.319	4.993	5.704
3.168	2.612	5.919	1.869	3.326	2.868	6.441	1.943
-17.200	4.187	-10.786	3.474	-17.968	4.526	-11.078	3.701
10.273	4.969	6.315	4.464	11.227	5.532	6.591	4.799
10.367	6.184	1.844	6.343	10.287	6.927	1.942	6.926
-17.372	3.318	2.053	5.159	-19.308	3.806	3.351	6.613
1.277	2.500	-7.912	3.201	1.555	3.067	-8.546	3.411
-4.444	4.007	0.819	3.773	-3.555	5.301	1.653	5.463
-2.287	3.743	-2.460	5.649	-2.361	4.769	-2.290	6.340
19.332	10.861	-4.950	7.471	21.443	10.736	-4.974	7.994
5.814	7.650	9.310	4.166	5.943	8.136	10.082	4.109
-5.497	2.666	-0.292	4.470	-5.332	3.406	0.252	5.170
0.864	7.235	-5.078	4.868	1.251	7.444	-5.180	4.819
-5.818	6.655	0.834	6.361	-6.214	7.787	0.693	7.612
4.498	7.337	7.556	8.419	6.039	8.460	8.547	13.135
-7.456	3.323	-7.452	2.900	-7.859	3.793	-7.698	2.997
-7.692	2.850	-0.991	3.746	-9.017	3.843	-1.305	6.328
5.518	2.842	-10.818	4.388	5.430	4.702	-12.943	4.460
3.703	3.329	3.672	3.232	3.500	3.553	3.874	4.048

Table A.4: (continued)

SWF Method				HHT With ISBM Improvement			
Mean DiffMax (mm)	SD DiffMax (mm)	Mean DiffMin (mm)	SD DiffMin (mm)	Mean DiffMax (mm)	SD DiffMax (mm)	Mean DiffMin (mm)	SD DiffMin (mm)
5.748	4.806	0.178	5.968	6.022	5.242	0.423	6.493
1.997	5.572	0.889	5.331	2.623	6.521	1.126	6.036
0.236	3.856	1.635	3.464	-0.054	3.988	1.879	4.326
8.255	5.207	-8.705	4.661	9.357	6.016	-9.556	5.651
2.155	4.061	5.242	2.797	2.556	4.587	5.496	2.866
-5.150	2.639	-3.318	3.526	-5.003	3.134	-3.593	4.018
-1.481	3.957	4.486	2.625	-1.500	4.440	4.865	2.603
1.745	5.288	-4.206	4.550	2.031	6.516	-4.130	5.346
9.209	6.270	-2.181	7.929	9.917	7.148	-2.572	9.050
7.642	9.629	9.676	6.417	8.325	9.979	10.633	7.103
9.369	8.736	-2.519	5.174	10.995	8.598	-2.575	7.429
-6.330	3.727	13.042	4.754	-6.667	4.295	14.623	4.735
-0.554	3.780	6.395	3.665	-0.457	4.530	7.103	3.844
-5.952	3.430	-6.686	3.801	-6.057	3.651	-6.781	4.182
-6.813	2.547	-9.296	2.544	-6.882	2.788	-9.762	2.878
-0.848	3.346	6.351	2.971	-0.947	4.096	7.050	3.498
15.552	4.523	12.715	5.922	16.386	5.001	13.486	6.000
-2.023	2.815	7.668	5.862	-2.794	5.506	7.950	7.286
-5.606	4.667	4.907	3.450	-5.667	6.087	5.237	5.538
-1.871	4.737	6.706	6.672	-1.064	7.427	6.543	7.447
-12.520	4.472	5.696	2.508	-13.010	5.027	6.111	2.642
1.077	5.367	7.559	4.353	1.384	5.846	8.272	4.943
6.100	4.427	11.344	3.721	7.182	4.357	12.231	3.981
6.114	5.862	-2.182	4.656	6.758	6.448	-3.006	5.652
-0.940	3.309	-3.487	2.456	-0.812	3.466	-3.321	2.498

Table A.4: (continued)

SWF Method				HHT With ISBM Improvement			
Mean DiffMax (mm)	SD DiffMax (mm)	Mean DiffMin (mm)	SD DiffMin (mm)	Mean DiffMax (mm)	SD DiffMax (mm)	Mean DiffMin (mm)	SD DiffMin (mm)
2.484	4.149	6.266	4.310	2.556	4.861	6.976	5.770
5.845	4.017	5.801	1.857	5.655	4.245	6.219	1.814
-18.926	3.663	-12.239	3.741	-19.533	3.972	-13.016	4.106
-22.520	7.538	-3.864	8.733	-7.982	21.708	-0.111	10.430
-7.510	5.263	-16.815	6.018	-7.672	5.069	-17.847	5.959
9.919	5.473	-7.041	5.057	10.884	6.159	-7.684	5.332
-1.304	4.459	3.152	5.027	-1.363	4.768	3.461	5.106

APPENDIX B: Results from Single Accelerometer Tests and Accelerometer-Videogrammetry Tests

Table B.1: Accelerometer-videogrammetry test results: means and standard deviations of DiffMax and DiffMin from the camera and the sensor.

			Camera (position)				1.48*Accelerometer			
A_{Lame}/A_{Normal}	Normal Displacement (mm)	Type	Mean DiffMax (mm)	SD DiffMax (mm)	Mean DiffMin (mm)	SD DiffMin (mm)	Mean DiffMax (mm)	SD DiffMax (mm)	Mean DiffMin (mm)	SD DiffMin (mm)
0	50.8	0	0.018	0.238	-0.032	0.158	-0.145	0.352	-0.009	0.127
0	101.6	0	-0.040	0.192	-0.007	0.075	0.076	0.371	0.067	0.215
0	50.8	0	-0.007	0.061	0.013	0.141	0.015	0.098	0.106	0.509
0	101.6	0	-0.035	0.300	0.032	0.204	-0.016	0.458	0.044	0.210
0	50.8	0	-0.009	0.090	-0.051	0.133	0.103	0.191	-0.016	0.202
0	101.6	0	-0.085	0.273	0.029	0.224	-0.084	0.386	0.076	0.295
0.2	50.8	2	2.085	0.047	6.039	0.041	2.102	0.231	5.104	0.139
0.2	101.6	2	-2.959	0.187	-13.916	0.302	-3.234	0.401	-10.969	0.432
0.2	50.8	1	-2.896	0.051	5.639	0.056	-2.247	0.054	4.918	0.070
0.2	101.6	1	7.380	0.285	-14.024	0.113	5.861	0.324	-12.415	0.230
0.2	50.8	1	6.019	0.113	-2.544	0.101	5.240	0.218	-2.629	0.197
0.2	101.6	1	-15.310	0.356	7.296	0.224	-12.946	0.330	7.452	0.130
0.4	50.8	2	-4.044	0.080	-12.267	0.093	-4.113	0.126	-10.052	0.207
0.4	101.6	2	-6.386	0.197	-26.274	0.144	-7.145	0.316	-20.895	0.319
0.4	50.8	1	5.888	0.165	-11.972	0.075	4.400	0.178	-10.291	0.030
0.4	101.6	1	13.255	0.368	-26.792	0.024	10.284	0.184	-23.213	0.121
0.4	50.8	1	12.878	0.086	-5.321	0.087	10.977	0.343	-5.256	0.208
0.4	101.6	1	-28.873	0.303	13.478	0.694	-24.874	0.152	13.737	0.631
0.6	50.8	2	-5.847	0.072	-18.776	0.063	-6.279	0.122	-15.411	0.188
0.6	101.6	2	-9.742	0.057	-36.785	0.430	-10.887	0.056	-29.346	0.422
0.6	50.8	1	-8.755	0.104	18.103	0.366	-6.362	0.265	15.877	0.309
0.6	101.6	1	19.837	1.428	-41.782	0.328	15.368	1.295	-36.310	0.355
0.6	50.8	1	18.638	0.079	-7.578	0.090	15.795	0.237	-7.486	0.167

Table B.1: (continued)

			Camera (position)				1.48*Accelerometer			
A_{Lame}/ A_{Normal}	Normal Displacement (mm)	Type	Mean DiffMax (mm)	SD DiffMax (mm)	Mean DiffMin (mm)	SD DiffMin (mm)	Mean DiffMax (mm)	SD DiffMax (mm)	Mean DiffMin (mm)	SD DiffMin (mm)
0.6	101.6	1	45.517	0.261	-20.514	0.089	39.287	0.357	-20.738	0.273
0.8	50.8	2	-6.955	0.222	-24.377	0.239	-7.539	0.218	-20.026	0.492
0.8	101.6	2	-13.711	0.274	-51.471	0.690	-15.308	0.487	-40.994	0.680
0.8	50.8	1	12.240	0.186	-26.102	0.098	9.490	0.183	-22.675	0.164
0.8	101.6	1	23.283	3.052	-50.890	0.928	18.186	2.756	-43.911	1.011
0.8	50.8	1	25.220	0.166	-10.171	0.133	21.461	0.344	-10.054	0.150
0.8	101.6	1	55.749	0.342	-24.476	0.135	48.163	0.485	-24.972	0.125
1	50.8	2	-8.594	0.139	-33.230	0.069	-9.347	0.182	-27.086	0.129
1	101.6	2	-15.518	0.559	-60.434	1.219	-16.914	0.646	-48.542	1.212
1	50.8	1	14.786	0.186	-32.459	0.064	11.147	0.120	-28.309	0.115
1	101.6	1	26.210	3.359	-60.242	1.069	20.375	3.253	-52.091	1.354
1	50.8	1	-33.754	0.243	13.446	0.263	-28.463	0.251	13.507	0.269
1	101.6	1	73.589	0.505	-31.175	0.052	63.781	0.470	-31.722	0.376
1.1	50.8	2	-8.729	0.070	-34.945	0.070	-9.569	0.155	-28.697	0.138
1.1	101.6	2	-17.413	0.644	-70.187	1.178	-19.724	0.618	-56.333	1.219
1.1	50.8	1	16.370	0.295	-36.141	0.107	12.346	0.360	-31.396	0.299
1.1	101.6	1	31.430	2.124	-70.947	0.598	24.382	2.470	-61.389	1.110
1.1	50.8	1	-37.889	0.193	15.108	0.204	-31.987	0.222	15.171	0.298
1.1	101.6	1	81.220	0.384	-33.514	0.060	70.450	0.367	-34.245	0.209
1.3	50.8	2	10.403	0.041	45.292	0.032	11.862	0.167	37.217	0.180
1.3	101.6	2	-18.347	0.514	-80.931	0.930	-21.305	0.544	-64.654	1.184
1.3	50.8	1	17.766	0.150	-40.240	0.134	13.617	0.067	-35.316	0.185
1.3	101.6	1	34.851	1.660	-80.540	0.390	27.225	1.989	-69.765	0.723
1.3	50.8	1	-44.264	0.140	17.156	0.183	-37.335	0.243	17.475	0.137

Table B.1: (continued)

			Camera (position)				1.48*Accelerometer			
A_{Lame}/ A_{Normal}	Normal Displacement (mm)	Type	Mean DiffMax (mm)	SD DiffMax (mm)	Mean DiffMin (mm)	SD DiffMin (mm)	Mean DiffMax (mm)	SD DiffMax (mm)	Mean DiffMin (mm)	SD DiffMin (mm)
1.3	101.6	1	101.134	0.731	-47.379	0.474	88.087	0.599	-47.389	0.598
1.5	50.8	2	-10.075	0.367	-47.555	0.370	-11.279	0.473	-39.232	0.575
1.5	101.6	2	-19.196	1.149	-86.966	1.839	-22.409	1.222	-69.755	2.333
1.5	50.8	1	21.138	0.232	-48.842	0.070	16.412	0.283	-42.832	0.223
1.5	101.6	1	37.399	1.227	-89.935	0.211	29.754	1.348	-78.017	0.565
1.5	50.8	1	-53.182	0.185	24.628	0.337	-44.788	0.307	23.622	0.285
1.5	101.6	1	109.706	0.303	-51.095	0.648	95.782	0.840	-51.026	0.740
1.6	50.8	2	-11.101	0.287	-56.042	0.257	-12.845	0.342	-46.142	0.379
1.6	101.6	2	-20.393	1.229	-97.304	1.836	-24.531	1.424	-77.847	2.100
1.8	50.8	2	-11.188	0.357	-62.369	0.276	-13.345	0.431	-51.370	0.468
1.8	101.6	2	-19.938	1.649	-106.245	2.262	-25.008	1.801	-84.649	2.457
2	50.8	2	-11.092	0.294	-69.272	0.210	-13.518	0.474	-57.016	0.290
2	101.6	2	-19.898	2.031	-117.912	2.600	-25.803	2.360	-94.405	2.876
1.3	101.6	2	-88.473	0.421	-33.905	0.132	-83.677	0.542	-21.813	0.178
1.5	50.8	2	-40.966	0.109	-19.110	0.052	-37.677	0.207	-14.069	0.120
1.5	101.6	2	-87.879	0.243	-34.228	0.276	-83.725	0.411	-22.868	0.399
1.6	50.8	2	-45.296	0.151	-21.391	0.150	-41.713	0.135	-15.922	0.307
1.8	50.8	2	-57.445	0.235	-31.010	0.265	-52.380	0.238	-23.654	0.281
1.8	101.6	2	-115.946	0.568	-53.953	0.649	-108.683	0.489	-38.474	0.741
2	50.8	2	-55.811	0.210	-32.252	0.380	-51.164	0.346	-24.300	0.307
2	101.6	2	-21.421	0.477	-120.776	0.772	-26.939	0.704	-97.335	0.958
0	50.8	0	0.006	0.091	0.039	0.068	-0.161	0.214	0.034	0.308
0	101.6	0	-0.056	0.270	0.007	0.242	0.090	0.409	0.033	0.211
0.4	101.6	2	-23.843	0.159	-10.246	0.141	-22.533	0.332	-6.324	0.165

Table B.1: (continued)

			Camera (position)				1.48*Accelerometer			
A_{Lame}/A_{Normal}	Normal Displacement (mm)	Type	Mean DiffMax (mm)	SD DiffMax (mm)	Mean DiffMin (mm)	SD DiffMin (mm)	Mean DiffMax (mm)	SD DiffMax (mm)	Mean DiffMin (mm)	SD DiffMin (mm)
0.6	50.8	2	16.291	0.048	6.692	0.083	14.747	0.220	4.721	0.060
0.6	101.6	2	-35.883	0.208	-15.430	0.251	-33.573	0.401	-9.827	0.215
0.8	50.8	2	-23.552	0.090	-9.800	0.134	-21.408	0.113	-6.964	0.186
0.8	101.6	2	-48.670	0.112	-20.347	0.090	-45.674	0.282	-12.387	0.548
1	50.8	2	-29.248	0.082	-12.378	0.164	-26.501	0.258	-8.857	0.312
1	101.6	2	-63.115	0.214	-24.870	0.140	-59.641	0.208	-15.636	0.349
1.1	50.8	2	-32.745	0.168	-13.966	0.157	-29.726	0.231	-9.911	0.189
1.1	101.6	2	-70.147	0.138	-27.520	0.144	-66.160	0.318	-17.246	0.477
1.3	50.8	2	-37.451	0.140	-16.566	0.091	-34.200	0.112	-11.949	0.251

Table B.2: Accelerometer-Videogrammetry test results: means and standard deviations of DiffMax and DiffMin from Camera and Sensor with theoretical correction.

			Camera (position)				Theoretical Correction			
A_{Lame}/A_{Normal}	Normal Displacement (mm)	Type	Mean DiffMax (mm)	SD DiffMax (mm)	Mean DiffMin (mm)	SD DiffMin (mm)	Mean DiffMax (mm)	SD DiffMax (mm)	Mean DiffMin (mm)	SD DiffMin (mm)
0	50.8	0	0.018	0.238	-0.032	0.158	-0.141	0.380	-0.025	0.120
0	101.6	0	-0.040	0.192	-0.007	0.075	0.079	0.377	0.065	0.205
0	50.8	0	-0.007	0.061	0.013	0.141	0.004	0.106	0.091	0.488
0	101.6	0	-0.035	0.300	0.032	0.204	-0.006	0.473	0.051	0.213
0	50.8	0	-0.009	0.090	-0.051	0.133	0.109	0.196	-0.016	0.197
0	101.6	0	-0.085	0.273	0.029	0.224	-0.078	0.428	0.076	0.278
0.2	50.8	2	2.085	0.047	6.039	0.041	2.613	0.230	5.922	0.129
0.2	101.6	2	-2.959	0.187	-13.916	0.302	-3.971	0.408	-12.198	0.416
0.2	50.8	1	-2.896	0.051	5.639	0.056	-2.664	0.079	5.764	0.074
0.2	101.6	1	7.380	0.285	-14.024	0.113	6.764	0.354	-13.732	0.228
0.2	50.8	1	6.019	0.113	-2.544	0.101	6.326	0.239	-3.095	0.184
0.2	101.6	1	-15.310	0.356	7.296	0.224	-15.369	0.375	8.267	0.139
0.4	50.8	2	-4.044	0.080	-12.267	0.093	-5.097	0.122	-11.719	0.201
0.4	101.6	2	-6.386	0.197	-26.274	0.144	-8.626	0.344	-23.042	0.289
0.4	50.8	1	5.888	0.165	-11.972	0.075	5.207	0.189	-12.102	0.032
0.4	101.6	1	13.255	0.368	-26.792	0.024	11.945	0.216	-25.708	0.085
0.4	50.8	1	12.878	0.086	-5.321	0.087	13.279	0.351	-6.215	0.198
0.4	101.6	1	-28.873	0.303	13.478	0.694	-29.303	0.166	15.216	0.641
0.6	50.8	2	-5.847	0.072	-18.776	0.063	-7.700	0.113	-17.923	0.192
0.6	101.6	2	-9.742	0.057	-36.785	0.430	-13.000	0.048	-32.095	0.440
0.6	50.8	1	-8.755	0.104	18.103	0.366	-7.571	0.251	18.575	0.329
0.6	101.6	1	19.837	1.428	-41.782	0.328	17.752	1.430	-39.985	0.288
0.6	50.8	1	18.638	0.079	-7.578	0.090	13.605	0.216	-5.888	0.162
0.6	101.6	1	45.517	0.261	-20.514	0.089	35.556	0.338	-16.209	0.288

Table B.2: (continued)

			Camera (position)				Theoretical Correction			
A_{Lame}/ A_{Normal}	Normal Displacement (mm)	Type	Mean DiffMax (mm)	SD DiffMax (mm)	Mean DiffMin (mm)	SD DiffMin (mm)	Mean DiffMax (mm)	SD DiffMax (mm)	Mean DiffMin (mm)	SD DiffMin (mm)
0.8	50.8	2	-6.955	0.222	-24.377	0.239	-6.497	0.195	-16.040	0.452
0.8	101.6	2	-13.711	0.274	-51.471	0.690	-13.977	0.466	-32.145	0.640
0.8	50.8	1	12.240	0.186	-26.102	0.098	8.364	0.171	-17.939	0.152
0.8	101.6	1	23.283	3.052	-50.890	0.928	16.790	2.561	-33.953	0.847
0.8	50.8	1	25.220	0.166	-10.171	0.133	18.517	0.314	-7.916	0.136
0.8	101.6	1	55.749	0.342	-24.476	0.135	43.761	0.493	-19.466	0.180
1	50.8	2	-8.594	0.139	-33.230	0.069	-8.078	0.199	-21.742	0.135
1	101.6	2	-15.518	0.559	-60.434	1.219	-15.612	0.596	-38.111	1.132
1	50.8	1	14.786	0.186	-32.459	0.064	9.932	0.113	-22.639	0.121
1	101.6	1	26.210	3.359	-60.242	1.069	18.760	3.013	-40.038	1.169
1	50.8	1	-33.754	0.243	13.446	0.263	-24.761	0.240	10.753	0.237
1	101.6	1	73.589	0.505	-31.175	0.052	58.108	0.464	-24.898	0.337
1.1	50.8	2	-8.729	0.070	-34.945	0.070	-8.304	0.150	-22.982	0.128
1.1	101.6	2	-17.413	0.644	-70.187	1.178	-18.068	0.603	-44.154	1.108
1.1	50.8	1	16.370	0.295	-36.141	0.107	10.993	0.343	-24.996	0.269
1.1	101.6	1	31.430	2.124	-70.947	0.598	22.669	2.315	-47.933	0.999
1.1	50.8	1	-37.889	0.193	15.108	0.204	-27.770	0.223	12.030	0.297
1.1	101.6	1	81.220	0.384	-33.514	0.060	64.717	0.369	-27.013	0.272
1.3	50.8	2	10.403	0.041	45.292	0.032	10.367	0.166	29.717	0.185
1.3	101.6	2	-18.347	0.514	-80.931	0.930	-19.701	0.512	-50.444	1.077
1.3	50.8	1	17.766	0.150	-40.240	0.134	12.295	0.076	-28.199	0.169
1.3	101.6	1	34.851	1.660	-80.540	0.390	25.504	1.876	-54.552	0.586
1.3	50.8	1	-44.264	0.140	17.156	0.183	-32.668	0.264	14.010	0.145
1.3	101.6	1	101.134	0.731	-47.379	0.474	-77.225	0.317	30.656	0.461

Table B.2: (continued)

			Camera (position)				Theoretical Correction			
A_{Lame}/A_{Normal}	Normal Displacement (mm)	Type	Mean DiffMax (mm)	SD DiffMax (mm)	Mean DiffMin (mm)	SD DiffMin (mm)	Mean DiffMax (mm)	SD DiffMax (mm)	Mean DiffMin (mm)	SD DiffMin (mm)
1.5	50.8	2	-10.075	0.367	-47.555	0.370	-9.954	0.439	-31.644	0.470
1.5	101.6	2	-19.196	1.149	-86.966	1.839	-20.846	1.188	-54.849	2.144
1.5	50.8	1	21.138	0.232	-48.842	0.070	14.853	0.254	-34.154	0.196
1.5	101.6	1	37.399	1.227	-89.935	0.211	27.944	1.257	-60.920	0.501
1.5	50.8	1	-53.182	0.185	24.628	0.337	-37.928	0.223	15.758	0.128
1.5	101.6	1	109.706	0.303	-51.095	0.648	87.514	0.622	-40.080	0.582
1.6	50.8	2	-11.101	0.287	-56.042	0.257	-11.374	0.311	-36.843	0.355
1.6	101.6	2	-20.393	1.229	-97.304	1.836	-23.024	1.294	-61.159	1.925
1.8	50.8	2	-11.188	0.357	-62.369	0.276	-12.021	0.390	-41.194	0.445
1.8	101.6	2	-19.938	1.649	-106.245	2.262	-23.648	1.655	-67.164	2.240
2	50.8	2	-11.092	0.294	-69.272	0.210	-12.280	0.421	-45.840	0.230
2	101.6	2	-19.898	2.031	-117.912	2.600	-24.565	2.190	-75.112	2.662
1.3	101.6	2	-88.473	0.421	-33.905	0.132	-76.968	0.403	-17.456	0.173
1.5	50.8	2	-40.966	0.109	-19.110	0.052	-33.227	0.135	-11.683	0.141
1.5	101.6	2	-87.879	0.243	-34.228	0.276	-77.973	0.430	-18.835	0.393
1.6	50.8	2	-45.296	0.151	-21.391	0.150	-36.810	0.118	-13.330	0.303
1.8	50.8	2	-57.445	0.235	-31.010	0.265	-43.989	0.197	-16.471	0.170
1.8	101.6	2	-115.946	0.568	-53.953	0.649	-99.614	0.446	-31.544	0.621
2	50.8	2	-55.811	0.210	-32.252	0.380	-44.953	0.080	-20.174	0.097
2	101.6	2	-21.421	0.477	-120.776	0.772	-25.702	0.619	-76.750	0.936
0	50.8	0	0.006	0.091	0.039	0.068	-0.150	0.203	0.036	0.293
0	101.6	0	-0.056	0.270	0.007	0.242	0.085	0.391	0.025	0.194
0.4	101.6	2	-23.843	0.159	-10.246	0.141	-20.948	0.324	-4.954	0.159
0.6	50.8	2	16.291	0.048	6.692	0.083	13.100	0.213	3.965	0.056

Table B.2: (continued)

			Camera (position)				Theoretical Correction			
A_{Lame}/A_{Normal}	Normal Displacement (mm)	Type	Mean DiffMax (mm)	SD DiffMax (mm)	Mean DiffMin (mm)	SD DiffMin (mm)	Mean DiffMax (mm)	SD DiffMax (mm)	Mean DiffMin (mm)	SD DiffMin (mm)
0.6	101.6	2	-35.883	0.208	-15.430	0.251	-31.207	0.390	-7.804	0.193
0.8	50.8	2	-23.552	0.090	-9.800	0.134	-18.926	0.104	-5.817	0.181
0.8	101.6	2	-48.670	0.112	-20.347	0.090	-42.388	0.253	-9.789	0.518
1	50.8	2	-29.248	0.082	-12.378	0.164	-23.411	0.240	-7.401	0.284
1	101.6	2	-63.115	0.214	-24.870	0.140	-55.041	0.251	-12.352	0.294
1.1	50.8	2	-32.745	0.168	-13.966	0.157	-26.219	0.224	-8.257	0.169
1.1	101.6	2	-70.147	0.138	-27.520	0.144	-61.159	0.296	-13.771	0.474
1.3	50.8	2	-37.451	0.140	-16.566	0.091	-30.162	0.106	-9.952	0.240

Table B.3: Accelerometer-Videogrammetry test results: means and standard deviations of DiffMax and DiffMin from the camera and sensor with empirical correction.

			Camera (Position)				Empirical Correction			
A_{Lame}/A_{Normal}	Normal Displacement (mm)	Type	Mean DiffMax (mm)	SD DiffMax (mm)	Mean DiffMin (mm)	SD DiffMin (mm)	Mean DiffMax (mm)	SD DiffMax (mm)	Mean DiffMin (mm)	SD DiffMin (mm)
11	50.8	1	-37.889	0.193	15.108	0.204	-38.228	0.212	17.422	0.276
10	50.8	1	-33.754	0.243	13.446	0.263	-34.018	0.268	15.604	0.290
4	101.6	1	-28.873	0.303	13.478	0.694	-29.300	0.166	15.233	0.642
2	101.6	1	-15.310	0.356	7.296	0.224	-15.370	0.375	8.277	0.139
6	50.8	1	-8.755	0.104	18.103	0.366	-7.580	0.251	18.606	0.330
2	50.8	1	-2.896	0.051	5.639	0.056	-2.667	0.080	5.774	0.074
4	50.8	1	5.888	0.165	-11.972	0.075	5.213	0.189	-12.122	0.032
2	50.8	1	6.019	0.113	-2.544	0.101	6.335	0.239	-3.101	0.184
2	101.6	1	7.380	0.285	-14.024	0.113	6.763	0.354	-13.748	0.228
8	50.8	1	12.240	0.186	-26.102	0.098	11.099	0.180	-26.545	0.161
4	50.8	1	12.878	0.086	-5.321	0.087	13.298	0.352	-6.226	0.198
4	101.6	1	13.255	0.368	-26.792	0.024	11.942	0.216	-25.737	0.085
10	50.8	1	14.786	0.186	-32.459	0.064	12.935	0.135	-32.945	0.109
11	50.8	1	16.370	0.295	-36.141	0.107	14.282	0.376	-36.533	0.279
13	50.8	1	17.766	0.150	-40.240	0.134	15.599	0.078	-40.789	0.192
6	50.8	1	18.638	0.079	-7.578	0.090	19.128	0.235	-8.850	0.149
6	101.6	1	19.837	1.428	-41.782	0.328	17.743	1.430	-40.027	0.288
15	50.8	1	21.138	0.232	-48.842	0.070	18.548	0.296	-49.319	0.220
8	101.6	1	23.283	3.052	-50.890	0.928	20.649	2.987	-47.967	0.869
8	50.8	1	25.220	0.166	-10.171	0.133	25.900	0.356	-11.781	0.128
10	101.6	1	26.210	3.359	-60.242	1.069	23.109	3.475	-56.659	1.103
11	101.6	1	31.430	2.124	-70.947	0.598	27.254	2.647	-66.409	0.889
13	101.6	1	34.851	1.660	-80.540	0.390	30.199	2.112	-75.064	0.563
15	101.6	1	37.399	1.227	-89.935	0.211	32.687	1.420	-83.306	0.440

Table B.3: (continued)

			Camera (Position)				Empirical Correction			
A_{Lame}/A_{Normal}	Normal Displacement (mm)	Type	Mean DiffMax (mm)	SD DiffMax (mm)	Mean DiffMin (mm)	SD DiffMin (mm)	Mean DiffMax (mm)	SD DiffMax (mm)	Mean DiffMin (mm)	SD DiffMin (mm)
13	50.8	2	-37.451	0.140	-16.566	0.091	-37.618	0.132	-14.611	0.291
6	101.6	2	-35.883	0.208	-15.430	0.251	-35.176	0.438	-13.235	0.272
11	50.8	2	-32.745	0.168	-13.966	0.157	-32.702	0.241	-12.132	0.214
10	50.8	2	-29.248	0.082	-12.378	0.164	-29.091	0.271	-10.814	0.339
4	101.6	2	-23.843	0.159	-10.246	0.141	-23.600	0.337	-8.652	0.208
8	50.8	2	-23.552	0.090	-9.800	0.134	-23.458	0.119	-8.500	0.203
20	101.6	2	-21.421	0.477	-120.776	0.772	-26.861	0.798	-135.736	1.317
16	101.6	2	-20.393	1.229	-97.304	1.836	-25.086	1.593	-107.772	2.410
18	101.6	2	-19.938	1.649	-106.245	2.262	-25.198	2.051	-117.602	2.859
20	101.6	2	-19.898	2.031	-117.912	2.600	-34.195	5.063	-131.801	4.173
15	101.6	2	-19.196	1.149	-86.966	1.839	-23.212	1.379	-96.449	2.576
13	101.6	2	-18.347	0.514	-80.931	0.930	-22.199	0.612	-89.318	1.357
11	101.6	2	-17.413	0.644	-70.187	1.178	-20.666	0.661	-77.119	1.382
10	101.6	2	-15.518	0.559	-60.434	1.219	-17.808	0.710	-66.335	1.375
8	101.6	2	-13.711	0.274	-51.471	0.690	-16.240	0.489	-56.144	0.779
18	50.8	2	-11.188	0.357	-62.369	0.276	-14.054	0.466	-65.389	0.561
16	50.8	2	-11.101	0.287	-56.042	0.257	-13.807	0.367	-58.784	0.478
20	50.8	2	-11.092	0.294	-69.272	0.210	-21.010	0.798	-73.831	0.422
15	50.8	2	-10.075	0.367	-47.555	0.370	-12.276	0.508	-50.086	0.686
6	101.6	2	-9.742	0.057	-36.785	0.430	-11.636	0.057	-40.400	0.430
11	50.8	2	-8.729	0.070	-34.945	0.070	-10.604	0.159	-36.417	0.183
10	50.8	2	-8.594	0.139	-33.230	0.069	-10.392	0.199	-34.399	0.112
8	50.8	2	-6.955	0.222	-24.377	0.239	-8.417	0.231	-25.305	0.527
4	101.6	2	-6.386	0.197	-26.274	0.144	-7.680	0.341	-28.501	0.323

Table B.3: (continued)

			Camera (Position)				Empirical Correction			
A_{Lame}/A_{Normal}	Normal Displacement (mm)	Type	Mean DiffMax (mm)	SD DiffMax (mm)	Mean DiffMin (mm)	SD DiffMin (mm)	Mean DiffMax (mm)	SD DiffMax (mm)	Mean DiffMin (mm)	SD DiffMin (mm)
6	50.8	2	-5.847	0.072	-18.776	0.063	-7.021	0.132	-19.384	0.217
4	50.8	2	-4.044	0.080	-12.267	0.093	-4.632	0.128	-12.646	0.225
2	101.6	2	-2.959	0.187	-13.916	0.302	-3.511	0.420	-14.967	0.476
2	50.8	2	2.085	0.047	6.039	0.041	2.369	0.242	6.383	0.150
13	50.8	2	10.403	0.041	45.292	0.032	12.985	0.164	47.424	0.230
6	50.8	2	16.291	0.048	6.692	0.083	16.105	0.229	5.747	0.070

Appendix C: Rotation Angles of Head and Pelvis of Trotting Horses

Table C.1: Maximum and minimum sensor rotation angles of real horses.

Name	Segment	Max Head Angle (Degree)	Min Head Angle (Degree)	Max Pelvis Angle (Degree)	Min Pelvis Angle (Degree)
4-10-2012 - diamond - baseline	1	6.700	-6.239	12.399	-12.221
4-10-2012 - diamond - baseline	2	7.436	-6.695	13.702	-12.660
4-10-2012 - diamond - baseline	3	9.636	-25.757	15.582	-13.738
4-10-2012 - diamond - baseline	4	8.792	-9.465	13.906	-12.902
4-11-2012 - cat daddy - baseline 2	1	4.934	-6.996	9.004	-11.078
4-11-2012 - cat daddy - baseline 2	2	7.942	-8.271	10.542	-11.987
4-11-2012 - cat daddy - baseline 2	3	5.827	-6.511	11.933	-13.399
4-11-2012 - cat daddy - baseline 2	4	16.108	-12.186	12.837	-11.232
4-11-2012 - cat daddy - baseline 2	5	5.603	-5.845	12.109	-13.601
4-11-2012 - cat daddy - baseline	1	7.358	-5.976	10.253	-10.462
4-11-2012 - cat daddy - baseline	2	7.037	-10.028	10.952	-11.781
4-11-2012 - cat daddy - baseline	3	6.458	-5.849	11.238	-12.577
4-11-2012 - cat daddy - baseline	4	5.764	-5.963	11.967	-12.719
4-11-2012 - gunner - baseline	1	6.487	-7.481	11.388	-11.675
4-11-2012 - gunner - baseline	2	7.613	-4.817	10.577	-11.326
4-11-2012 - gunner - baseline	3	8.296	-10.006	11.243	-12.292
4-11-2012 - gunner - baseline	4	15.751	-21.350	11.579	-12.744
4-11-2012 - true pride - baseline true	1	10.213	-8.422	9.106	-9.908
4-11-2012 - true pride - baseline true	2	8.810	-7.245	9.693	-12.395
4-11-2012 - true pride - baseline true	3	10.154	-5.221	9.045	-10.969
4-11-2012 - true pride - baseline true	4	8.252	-10.951	9.235	-10.991
4-12-2012 - heidi - baseline	1	6.746	-8.356	12.271	-10.940
4-12-2012 - heidi - baseline	2	5.481	-3.998	12.652	-11.623
4-12-2012 - heidi - baseline	3	5.960	-6.375	14.274	-12.535
4-12-2012 - heidi - baseline	4	5.344	-8.465	12.857	-12.216

Table C.1: (continued)

Name	Segment	Max Head Angle (Degree)	Min Head Angle (Degree)	Max Pelvis Angle (Degree)	Min Pelvis Angle (Degree)
4-12-2012 - lucy - baseline	1	7.231	-6.364	10.701	-10.999
4-12-2012 - lucy - baseline	2	11.318	-8.976	11.626	-9.310
4-12-2012 - lucy - baseline	3	11.246	-8.603	10.801	-10.190
4-12-2012 - lucy - baseline	4	11.159	-10.631	11.231	-12.652
4-12-2012 - sam - baseline	1	18.690	-19.702	10.001	-11.739
4-12-2012 - sam - baseline	2	8.866	-17.144	8.985	-12.542
4-12-2012 - sam - baseline	3	8.789	-9.540	11.235	-11.506
4-12-2012 - sam - baseline	4	12.410	-10.980	11.660	-12.069
4-17-2012 - kings gem - baseline	1	3.954	-5.666	8.237	-6.408
4-17-2012 - kings gem - baseline	2	6.193	-6.898	6.677	-6.225
4-17-2012 - kings gem - baseline	3	6.134	-4.918	6.985	-5.729
4-17-2012 - kings gem - baseline	4	5.089	-5.767	7.932	-6.729
4-17-2012 - kings gem - baseline	5	6.046	-5.478	8.317	-6.078
Britney - trot	1	6.640	-8.746	13.164	-10.529
Britney - trot	2	13.317	-14.356	13.750	-12.128
Britney - trot	3	10.986	-10.694	14.208	-11.368
Saddlebred - WW - Calvin - 8-13-2012 - trot 2	1	12.878	-12.791	8.708	-9.040
Saddlebred - WW - Calvin - 8-13-2012 - trot 2	2	25.695	-13.320	8.810	-9.531
Saddlebred - WW - Calvin - 8-13-2012 - trot	1	13.168	-17.071	9.043	-11.245
Saddlebred - WW - Calvin - 8-13-2012 - trot	2	18.409	-24.025	8.972	-10.503
Saddlebred - WW - Champagne - 8-13-2012 - trot 2	1	9.693	-8.852	14.648	-13.030
Saddlebred - WW - Champagne - 8-13-2012 - trot 2	2	24.474	-11.949	14.311	-13.247
Saddlebred - WW - Wendell - 8-13-2012 - trot	1	15.980	-18.846	7.667	-10.282